Reconstructing the Arrival Direction of Cosmic Neutrinos with the Radio Neutrino Observatory Greenland (RNO-G)

der Naturwissenschaftlichen Fakultät
der Friedrich-Alexander-Universität Erlangen-Nürnberg
zur Erlangung des Doktorgrades Dr. rer. nat.
vorgelegt von
Ilse Plaisier

Als Dissertation genehmigt von der
Naturwissenschaftlichen Fakultät der Friedrich Alexander-Universität
Erlangen-Nürnberg

Abstract

The production of *cosmogenic* neutrinos are expected in the ultra-high energy regime, due to charged particles, *cosmic rays*, that interact with photons of the cosmic microwave background. Due to the steeply falling flux for higher energies the currently largest neutrino detector (IceCube), covering a volume of $\approx$1 km^3, is only sensitive up to $\approx$ PeV energies. IceCube uses the detection of optical light, i.e. Cherenkov radiation, emitted by the particle shower that is generated due to a neutrino interacting in the South Pole ice. Since photons are scattered and absorbed in the ice, it relies on dense instrumentation of the detection modules.

The particle shower created by the neutrino interaction also emits radio pulses (Askaryan emission) with coherent emission on a cone with opening angle of the Cherenkov angle. These radio waves can propagate for hundreds of meters in glacial ice and are detectable for neutrinos with energies above $\approx$10 PeV. Therefore, detecting radio pulses is an excellent technique to build sparsely instrumented arrays for identifying these energetic low flux neutrinos. The Radio Neutrino Observatory Greenland (RNO-G), which uses the Greenlandic ice sheet as a detection medium, is the first running detector making use of this technique which has the prospects of detecting a neutrino. With that, RNO-G is the first experiment probing the energy scale beyond thus far measured. RNO-G builds on the experience of prototype in-ice neutrino detectors in Antartica, as well as the well established radio detection experiments for cosmic-ray air showers.

Besides the cosmogenic neutrinos, cosmic rays interacting with ambient matter and photon fields in the surrounding of their production sources result in the production of photons, as well as ultra-high energy *astrophysical* neutrinos. IceCube has found compelling evidence for such an astrophysical neutrino flux. Neutrinos do not get deflected or significantly absorbed while they are traversing the universe, like cosmic rays and photons. Therefore, when the direction of the neutrino can be accurately established, individual sources can be identified as cosmic-ray accelerators.

With the prospect of the first neutrino to be detected using the radio technique, it becomes more relevant to develop methods to extract the properties of these particles from the measured waveforms. In this thesis, a methodology is developed for reconstructing the incoming direction of a neutrino detected with an in-ice radio detector.

We make use of a *forward-folding* approach, which fits a model of the electric field to the measured waveforms detected with the antennas in order to obtain the direction. To obtain the neutrino direction, the angle under which the radio signal is recorded with respect to the shower axis (the *viewing angle*), as well as the arrival direction of the signal and direction of polarization of the electric field is needed. The frequency spectrum of the measured waveforms contains information on the viewing angle, and an amplitude measurement of waveforms detected in antennas sensitive to perpendicular polarizations will enable to obtain the direction of the electric field. The signal-model based approach directly fits forward folded electric-field priors to the voltage waveforms. It therefore combines the measure-

ment of the viewing angle and polarization, obtaining the neutrino direction. This results in the first reconstruction method for a deep in the ice located radio neutrino detector that uses the information of the complete station.

Using the developed reconstruction method, the angular resolution for RNO-G can be quantified. We find that the resolution is dependent on the incoming zenith direction of the neutrino as well as the energy of the particle shower. We find a median angular resolution of 3.2° with an analysis efficiency of 50%. For high quality events, which contain significant amplitude in antennas sensitive to the horizontal as well as vertical component of the electric field, an resolution of 1.3° is obtained.

The main uncertainty of the resolution comes from the polarization, and therefore uncertainty regions for neutrino events result in long and narrow bands on the sky. Consequently, RNO-G is capable of a good localization of $\approx$10 deg^2 for 90% containment for high-quality events, making RNO-G suited for the *multi-messenger* follow-up program.

Zusammenfassung

Durch die Wechselwirkung von geladen Teilchen, *kosmischer Strahlung*, mit Photonen des kosmischen Mikrowellenhintergrunds wird die Produktion von *kosmogenen* Neutrinos im ultrahochenergetischen Bereich erwartet. Aufgrund des steil abfallenden Flusses bei höheren Energien ist der derzeit größte Neutrinodetektor (IceCube), der ein Volumen von $\approx$1 km^3 abdeckt, nur bis zu $\approx$ PeV-Energien empfindlich. IceCube nutzt den Nachweis von optischem Licht, d.h. von Cherenkov-Strahlung, die von einem Teilchenschauer emittiert wird, der durch die Wechselwirkung eines Neutrinos im Eis des Südpols entsteht. Da Photonen im Eis gestreut und absorbiert werden, ist für IceCube eine dichte Instrumentierung der Detektionsmodule notwendig.

Der durch die Neutrino-Wechselwirkung erzeugte Teilchenschauer emittiert auch Radio pulse (Askaryan-Emission). Auf einem Kegel, mit dem Öffnungswinkel gleich dem Cherenkov-Winkel, ist die Emission kohärent. Diese Radiowellen können sich über Hunderte von Metern im Gletschereis ausbreiten und sind für Neutrinos mit Energien über $\approx$ 10 PeV nachweisbar. Daher ist die Nachweis von Radiopulsen eine hervorragende Technik, um spärlich instrumentierte Arrays zur Identifizierung dieser energiereichen Neutrinos mit niedrigem Fluss zu bauen. Das Radio-Neutrino-Observatory Greenland (RNO-G), das die grönländische Eisdecke als Detektionsmedium nutzt, ist der erste laufende Detektor, der diese Technik nutzt und Aussicht auf den Nachweis eines Neutrinos hat. Damit ist RNO-G das erste Experiment, das die Energieskala jenseits der bisher gemessenen Werte untersucht. RNO-G baut auf den Erfahrungen auf, welche mit Prototypen von Neutrinodetektoren in antarktischen Eis gemacht wurden, sowie auf den gut etablierten Radio-Detektionsexperimenten für kosmische Strahlung.

Zusätzlich zu den kosmogenen Neutrinos führt die Wechselwirkung der kosmischen Strahlung mit der umgebenden Materie und den Photonenfeldern in der Umgebung ihrer Produktionsquellen zur Erzeugung von Photonen und ultrahochenergetischen *astrophysikalischen* Neutrinos. IceCube hat überzeugende Beweise für einen solchen astrophysikalischen Neutrinofluss gefunden. Eine kombinierte Messung des Spektrums dieser kosmischen Strahlung, der Photonen und der Neutrinos wird Informationen über die Umgebung der Quellen sowie über die Quellenklassen liefern, welche die kosmische Strahlung auf diese hohen Energien beschleunigen. In Gegensatz zu kosmischer Strahlung und Photonen werden Neutrinos auf ihrer Reise durch das Universum weder abgelenkt noch absorbiert. Daher ist es möglich, dass wenn die Richtung des Neutrinos genau bestimmt werden kann, sich einzelne Quellen als Beschleuniger kosmischer Strahlung identifizieren lassen.

Mit der Aussicht, dass das erste Neutrino mit der Radiotechnik nachgewiesen werden

kann, wird es immer wichtiger Methoden zu entwickeln, um die Eigenschaften dieser Teilchen aus den gemessenen Wellenformen zu extrahieren. In dieser Arbeit wird eine Methode entwickelt, um die Einfallsrichtung eines Neutrinos zu rekonstruieren, welches mit einem In-Eis-Radiodetektor gemessen wurde.

Wir verwenden einen Ansatz der Vorwärtsfaltung, bei dem ein Modell des elektrischen Feldes an die mit den Antennan gemessenen Wellenformen angepasst wird, um die Richtung zu ermitteln. Um die Richtung des Neutrinos zu ermitteln, werden der Winkel unter dem das Radiosignal in Bezug auf die Schauerachse aufgezeichnet wird (der *Blickwinkel*), sowie die Ankunftsrichtung des Signals und die Richtung des Polarisation des elektrischen Feldes benötigt. Das Frequenzspektrum der gemessenen Wellenformen enthält Informationen über den Blickwinkel und eine Messung der Amplitude von Wellenformen, welche mit fur senkrechte Polarisation sensitiven Antennen gemessen wurden, ermöglicht es, die Richtung des elektrischen Feldes zu ermitteln. Der auf einem Signalmodell basierende Ansatz passt die vorwärts gefalteten a-priori-Verteilung für das elektrische Feld direkt an die gemessenen Wellenformen an. Der Ansatz kombiniert daher die Messung des Sichtwinkels und der Polarisation, um die Richtung des Neutrinos zu erhalten. Das Ergebnis ist die erste Rekonstruktionsmethode für einen tief im Eis befindlichen Radio-Neutrino-Detektor, welche die Informationen der gesamten Station nutzt.

Mit der entwickelten Rekonstruktionsmethode kann die Winkelauflösung für RNO-G quantifiziert werden. Wir stellen fest, dass die Auflösung sowohl von der einfallenden Zenitrichtung des Neutrinos als auch von der Energie des Teilchenschauers abhängt. Wir finden eine mittlere Winkelauflösung von 3,2° bei einer Analyseeffizienz von 50%. Für qualitativ hochwertige Ereignisse, die eine signifikante Amplitude in Antennen enthalten, die sowohl für die horizontale als auch für die vertikale Komponente des elektrischen Feldes empfindlich sind, ergibt sich eine Auflösung von 1,3°.

Die Hauptunsicherheit der Auflösung kommt von der Polarisation und daher ergeben sich Unsicherheitsbereiche fur Neutrino-Ereignisse als lange und schmale Bänder am Himmel. Infolgedessen ist RNO-G in der Lage, 90% der Ereignisse von hoher Qualität mit einer guten Lokalisierung von ca. 10 deg^2 zu rekonstruieren. Dadurch eignet sich RNO-G für das *multi-messenger* Nachfolgeprogramm.

Table of Contents

Chapter 1

Introduction

Nuanneq naapilluti.

— *Greelandic for* Pleased to meet you

This thesis portrays the prospects of the encounter of a particle that has never been met before. The timing of this occurence is unknown. As is when it will happen again. And how often. A meeting destined to be veiled, since only the imprints these particles leave behind can be observed. That is, only if they decide to even leave a trace. Particles that are memorable and rare, since they are faster than their flock. A meeting to look forward to. And to be prepared for in order to gain most value out of the occasion. Since, despite the little we know about these encounters, for sure they will at most happen rarely.

This thesis is about ultra-high energy *neutrinos*. Those above 10 PeV. *Astrophysical* ones, or *cosmogenic*. It focusses on a relatively new technique to detect cosmic particles: detection of the *radio* waves generated as a consequence of the interaction of the particle with matter. This is the first technique that has the potential to detect neutrinos of these incredible energies.

This thesis is centred around the *Radio Neutrino Observatory - Greenland* (RNO-G), which detects the emission within the Greenlandic ice sheet created by interacting neutrinos. RNO-G will be the first experiment that has the capability to potentially confirm the existense of these energeticals.

The fascinating thing about the occurence with these neutrinos, is that they leave an impress about where they originate from: the progenitors that drive these particles to be so energetic. The direction and the journey that they underwent will reveal their origins. This thesis focusses on this key ingredient of extracting information from the left behind footprint: identifying the incoming direction of the neutrinos.

How the origin of the neutrinos is related to their journey, and therefore the motivation for a good esimate of the direction of the neutrino, is outlined in chapter 2. Then, the argument for the usage of the radio technique to detect these particles is described in chapter 3. Chapter 4 describes the experiment of focus for this thesis: RNO-G. Next, in chapter 5, the

toolbox to capture reality in a software framework is discussed. It describes the interaction of the neutrinos in the ice, the description of the RNO-G experiment as well as its reconstruction tools. Within this framework, the methodology for reconstructing the direction of the neutrinos is developed, which is discussed in chapter 6. The obtained angular resolution and implications for RNO-G and other in-ice radio neutrino experiments are discussed in chapter 7.

The three years during this thesis, RNO-G has evolved from an unfunded proposal to its first year of datataking. Besides the direction reconstruction methodology and results, various aspects of the RNO-G development are implanted in this thesis, among which station design, first data taking as well as simulation development. Chapter 4 gives insight in the optimization of the RNO-G antennas and the station design. Furthermore, analyzed data from the first RNO-G season is part of chapter 3. Also, development of more precise simulations for ice modeling are discussed in chapter 5, as well as first results in 6. The radio neutrino detection benefits from the predecessor of cosmic-ray radio detection. Cosmic-ray data from an in-ice neutrino radio detector is analyzed as part of chapter 6.

Chapter 2

Ultra-High Energy Neutrinos

Angalalluarina.
— *Greenlandic for* Have a good journey

The Radio Neutrino Observatory in Greenland (RNO-G) will be sensitive to ultra-high energy (UHE) neutrinos, which are out of reach for any currently data-taking neutrino observatory. This chapter starts with introducing the neutrino in section 2.1. For these ultra-high energies, neutrinos are predicted to stem from the interaction of cosmic-rays with the ambient matter and photon fields in the vicinity of their production sites, *astrophysical neutrinos*, as well as the interaction with the CMB, resulting in *cosmogenic neutrinos*, as will be discussed in section 2.3. Besides neutrinos also photons are created when cosmic rays interact with their surroundings, and therefore combining knowledge of each of these particles gives information on the cosmic-ray accelerators, which makes neutrinos part of the *multi-messenger* particles. Section 2.2 discusses the relevant properties of these messengers and the processes that create them, hence how they can be combined to learn more about the universe. Then, section 2.4 gives a short overview on the current detection methods for the multi-messenger particles.

2.1 Little Neutron

The first theoretical prediction of the neutrino goes back to 1930, when Pauli suggested a new neutral particle. He was unable to attend a conference on radioactivity, and therefore he wrote a simple letter with his theory. He called his newly designed particle a *neutron*, because of its uncharged nature. He came up with the idea in order to solve two outstanding problems. First, besides the well recognized particles the electron and proton, an extra neutral particle was needed with similar mass as the proton in order to explain the masses of heavier elements. The current belief was that this particle consisted of a proton and electron bounded tight together. Secondly, beta decay had shown to result in electrons with a whole spectrum of energies, which would contradict energy balance as proposed by Einstein if the electron was the only resulting particle in beta decay. Both problems could be fixed with this new neutral imaginary particle. However, Chadwick discovered in 1932 the neutron, but found out that it was very heavy. This particle could not be the answer to the continuous spectrum of electrons as a result for beta decay, since it required an at most very low mass particle. Therefore, the two puzzles turned out to not be solvable by the same particle-answer. The neutron got recognized as a new particle, and with that also the idea of inventing new particles to solve physics problems. With that, Pauli was more supported by the public in his quest to find a new almost massless neutral particle for the beta decay anomaly. Because of the masses of the newly discovered and soon to be discovered particle, the latter was proposed to be called *little neutron*, also *neutrino*.

The theory became more likely when the end of the energy spectrum of beta decay electrons was measured more precisely. The end turned out to have a hard cut-off which means that an extra particle was involved. The first detection of the neutrino, however, only happened more than a quarter of a century later than its first proposal, in 1956 [1]. Meanwhile, the theoretical framework of beta decay was completely set up by Fermi and the experimental set-up was thought through by Pontecorvo [2]. All that Cowan and Reines had to do was the actual experiment. They put water tanks 12 meter underground, to shield it from cosmic rays and put it 11 meters away from a reactor. They observed three gamma rays, the first two due to annihilation of a positron with an electron. The last one due to a neutron capture. Coincidence of the positron-electron annihilation and the neutron capture as detected, gave the unique signature of an anti-neutrino reacting with a proton which is known as *inverse beta decay*.

The universe is drowned in neutrinos as it is the dominant particle besides photons. Despite the Earth daily being bumped, accessed and left-behind, with trillions of these neutrinos, life easily goes on as they are harmless. And regardless their superabundant presence, less is known about this particle than any other particle that has ever been seen. Neutrinos are everywhere and seem to be created everywhere, as even radioactivity from the calcium in your own bones is producing neutrinos.

Neutrinos have an extremely low probability to interact and therefore they live very long. Consequently, the Earth is not only covered with neutrinos that are terrestial, but also neutrinos that are solar and come from anywhere in the universe. Since most parts of the universe are inaccessible for human means of traveling, our next best chance to explore its wideness is tracing the messengers it sends to Earth. However, neutrinos are electrically neutral, meaning that they are only visible in a detector when they interact. Neutrinos have a very

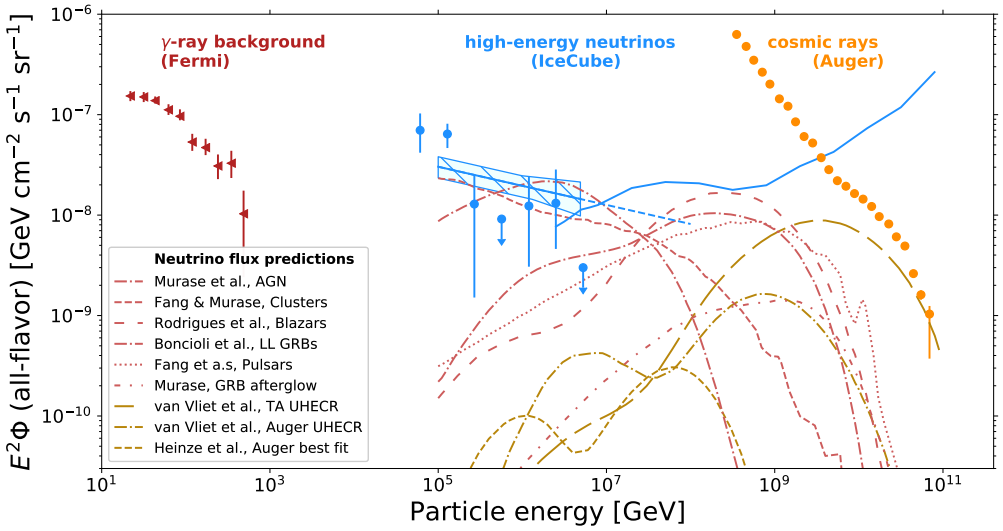

Figure 2.1: Isotropic energy spectrum of the three multi-messenger particles: gamma rays, neutrinos and cosmic rays with data given by Fermi [14], IceCube [15] and Pierre Auger [16] respectively. In the dashed lines predicted fluxes are given for several sources (red) and for cosmogenic neutrinos (dark yellow) for the energy range of the sensitivity of radio detectors. Figure taken from [17].

low mass, are only weakly interacting and have an extremely small cross-section [3], which makes interactions very rare, detecting them extremely difficult and challenging and therefore it makes the learning process slow.

One of the things known about these particles is that they are like no other particle observed so far, since they tend to change flavour during their lifetime, in a process called *neutrino oscillations*. The Homestake Experiment concluded in 1964 that the electron neutrino flux expected due to the nuclear fusion in the sun was only a third of what was expected [4]. Only four decades later it was discovered that the deficit of electron neutrinos matched the excess of generated muon neutrinos [5]. The change of flavour state of the neutrino is only possible when the neutrinos have non-zero mass, which led to the first discovery of physics beyond the standard model. These days, lots of experiments are aiming to measure the mass differences between the three neutrino flavours e, μ and τ for which reactor [6], solar [7], atmospheric [7; 8; 9] or accelerator [10] neutrinos are used, depending on the neutrino state.

A bit more than 20 years later, in 1987, after the first detections of the solar neutrinos, neutrinos were measured from beyond our own solar system. Several neutrino experiments measured simultaneously an excess in neutrinos which coincided with the core-collapse of a shortly before discovered supernova in the Large Magellanic Cloud [11]. Besides the first detected neutrinos that could be identified as probes of studying the universe outside our own solar system, this was also the first observation of an extra-solar source using multiple messengers. IceCube, worlds largest neutrino detector, as first discovered in 2013 a flux of high-energy astrophysical neutrinos and thereby the role of neutrinos as messengers of far away sources had been established [12; 13].

2.2 Neutrinos as Multi-Messenger Particles

Humanity has been studying the universe by perceiving photons arriving at Earth since the very beginning. Only recently, other particles made their way in the methods for studying the universe and with that the gap between *particle physics* and *astronomy* got filled with *astroparticle physics*; particle physics with astrophysical accelerators. Also, astronomy got broadened to *multi-messenger astronomy*, incorporating information from messengers other than photons. These other particles are the *cosmic-rays* and the neutrinos.

2.2.1 Multi-Messenger Astronomy

Cosmic rays were first discovered by Victor Hess in 1912, when he found that the ionizing radiation was surprisingly increasing with altitude, because the Earth itself was expected to be the source of radiation [18]. This indicated that these cosmic rays originated from an extraterrestrial source. The thought to be *rays*, however, turned out to be charged particles, which makes their origin hard to be pin-pointed because they are deflected by the magnetic fields they traverse while propagating to the Earth.

Nowadays, large scale experiments are installed for detecting each of the multi-messenger particles: *gamma rays*, neutrinos and cosmic rays. The current isotropic fluxes measured for these messengers are visualized in figure 2.1. The energy densities are tantalizingly identical for the three messengers, which suggests a common origin, although each occurring in their own energy regime. The cosmic-ray spectrum, being very well established over the last decades, extends all the way up to 10^{20} eV which is far beyond the energies of current earth-based accelerators; LHC (CERN) is capable of accelerating particles up to 10^{12} eV.

To shed light on the sources that are capable of accelerating these charged particles up to these significant energies, the cosmic rays themselves are not very helpful due to their charged nature. Gamma rays, being uncharged and therefore pointing directly back to the source of creation, don't require cosmic rays to be produced and for very high energies they suffer from extinctive absorption. This makes neutrinos very promising candidates for further revealing the source of cosmic rays, since they are not only uncharged, but they also make their way towards Earth. Combining information of multiple messengers led to the identification of the first likely source of high-energy neutrinos, TXS 0506+056, which was in the direction of a high energy neutrino and was also flaring in gamma rays [19].

The neutrino is the particle of target of this thesis and specifically neutrinos with energies beyond the ones thus far measured with IceCube, i.e. $>$ 10 PeV.

2.2.2 Cosmic Rays

Since Hess' balloon experiment, a variety of large scale detectors have been developed and the cosmic-ray energy spectrum has been identified. Cosmic rays with energies of 10^{20} eV have been measured, suggesting sources hidden in the universe that are very successful accelerators. The main concept that is generally thought to be the producer of these accelerated particles is *Fermi acceleration* [20]. Fermi originally proposed the idea of particles being accelerated due to being repeatedly reflected by magnetic mirrors. The dominant process

is thought to be *diffusive shock acceleration*, in which acceleration occurs through repeated crossing of a shock front. After each crossing, particles have a probability to escape the acceleration zone. More cycles are required for a particle to gain higher energies and therefore the energy spectrum created due to pure Fermi acceleration leads to a power law with $E^{-\gamma}$ spectrum, with a spectral index of $\gamma \approx 2$. Besides that the source must be capable of accelerating cosmic rays due to Fermi acceleration, a requirement for acceleration to high energies, is that the particle can be contained during the acceleration process. This condition of the Larmor radius of a particle to fit within the physical size of the acceleration zone is called the *Hillas criterion* and it sets constraints on the magnetic field strength and the source extension. The conditions on the physical size and the magnetic fields of a source also determine the maximum possible energy reachable for a particle being accelerated by the source. This could lead to an abrupt cut-off in the cosmic-ray energy spectrum. Such a cut-off indeed seems to be the case in the well-measured energy spectrum by the Pierre Auger Observatory (PAO) [21].

Up to 1 PeV, the cosmic-ray spectrum is well described by a power law, after which there is a spectral softening, the so-called *knee*. Around 10^{18} eV the spectrum undergoes a hardening which is known as the *ankle*. The energy spectrum ends with a high-energy cut-off. The knee is likely caused by the transition from galactic to extra galactic cosmic rays, whereas the origin of the ankle has not yet been resolved. Besides the Hillas criterion, an explanation for the cut-off could be the *Greisen-Zatsepin-Kuzmin limit* (GZK), or a combination of the two [22; 23]. Very low statistics is available in the highest energy regime above 10^{18} eV due to the low flux at these energies and the enormous detectors needed to cover such a flux, which constitutes difficulties in resolving the reason for the cut-off. Furthermore, the resolution of mass composition is poor due to the statistical fluctuations of the indicator parameter the shower maximum, X_{max}, and the uncertainties in hadronic interaction models [24].

The GZK limit is the maximum energy limit for cosmic rays before they interact with photons from the cosmic-microwave background (CMB). When this happens, pions are produced via the delta resonance:

$$p + \gamma_{\text{CMB}} \rightarrow \Delta^{+} \rightarrow n + \pi^{+} \tag{2.1}$$

$$p + \gamma_{\text{CMB}} \rightarrow \Delta^{+} \rightarrow p + \pi^{0} \tag{2.2}$$

For nearby cosmic-ray sources, attenuation due to the GZK effect is less likely, and therefore the detection of cosmic rays beyond the energy cut-off would constrain the distance for the production of UHE cosmic rays.

2.2.3 Neutrinos

Due to the abundance of photon fields in almost any source, cosmic-ray production has the by-product of neutrino production. The charged pions created in the interaction of cosmic rays with surrounding photons, the general case of equation 2.1, where $\gamma_{\text{CMB}} = \gamma$, will decay to muons, which will then further decay to electrons, generating two neutrinos:

$$\pi^{+} \rightarrow \nu_{\mu} + \overline{\nu_{\mu}} + \nu_{e} + e^{+}, \pi^{-} \rightarrow \overline{\nu_{\mu}} + \nu_{\mu} + \overline{\nu_{e}} + e^{-} \tag{2.3}$$

Furthermore, cosmic rays can interact with ambient matter which also leads to charged pion production:

$$p + p \rightarrow p, \pi^{\pm}, \pi^{0} \tag{2.4}$$

When this neutrino generation happens inside the sources, they are generally called *astrophysical* neutrinos. On the other hand, the charged pions created in the GZK effect will lead to the so-called *cosmogenic* neutrinos. Because the composition of cosmic rays determines the exact GZK cut-off, the cosmogenic neutrino flux is also dependent on the cosmic-ray composition.

Because neutrinos are electrically neutral, they are not deflected by magnetic fields and they will, similar to photons, travel in straight lines. Furthermore, they are not expected to get attenuated by interactions with the surroundings. For those reasons, neutrinos are good messengers to discover the UHE cosmic-ray sources, although the tendency of neutrinos to rarely interact, makes them hard to detect.

2.2.4 Photons

Studying the universe with photons is the oldest and most established branch in astrophysics. It is common to distinguish between sources in thermal equilibrium producing thermal radiation, while the tracers of cosmic rays are usually photons from non-thermal emission processes like e.g. synchrotron radiation, Compton scattering or neutral pion decays. We observe non-thermal emission across the entire electromagnetic spectrum from radio up to gamma rays. The photons associated with neutrino production are the *hadronic gamma rays*. The same reactions (the general case of equation 2.1 and 2.4) that create the charged pions for the neutrinos, are always accompanied by neutral pions, which will decay to a photon pair:

$$\pi^{0} \rightarrow \gamma + \gamma \tag{2.5}$$

Therefore, neutrino production is always accompanied by gamma ray production. Gamma rays arising from protons interacting with the CMB background are the so-called *cosmogenic photons*.

However, the generated gamma rays are probable to be absorbed, and even if they escape their production site, they are likely to interact with the Extragalactic Background Light (EBL), leading to pair production:

$$\gamma + \gamma_{\mathrm{EBL}} \rightarrow e^{+} + e^{-} \tag{2.6}$$

Therefore, neutrinos can be detected coming from sources which are dark in gamma rays. This EBL absorption causes a strong attenuation for gamma rays for distant objects, meaning that the vast majority of detected gamma ray emitters are located within the local universe. The absence of detecting PeV photons is therefore an argument that the highest energy cosmic rays are of extragalactic origin.

Other ubiquitous production mechanisms result in *leptonic gamma rays*. In main astrophysical sources of radiation electrons are observed to produce synchrotron radiation in turbulent magnetic fields or scatter up photons to higher energies via inverse Compton scattering.

Therefore, if gamma rays are detected, these do necessarily need to be accompanied by neutrino production and can therefore complicate the multi-messenger study.

2.3 Science Case UHE Neutrinos

The neutrinos of interest for the Radio Neutrino Observatory Greenland (RNO-G) are neutrinos with an energy above 10^{16} eV. The neutrino flux depends strongly on the cosmic-ray flux properties, in particular the cosmic-ray composition, their energy spectrum and their source distribution. A measurement of the neutrino flux can be used to place constraints on these parameters, as well as on the parameters of source environments and hadronic interaction models [25]. For the energy regime of RNO-G, multiple theories have predicted astrophysical sources to produce neutrinos as well as models resulting in cosmogenic neutrinos which exclusively predict feasible fluxes in the ultra-high energy regime, with energies higher than current neutrino detectors are sensitive to. Models for both scenarios are indicated in figure 2.1. In this section, astrophysical as well a cosmogenic neutrinos are discussed.

2.3.1 Astrophysical Neutrino Sources

A number of astrophysical sources are addressed as potential candidates for neutrinos in the RNO-G sensitivity regime, of which *pulsars*, *gamma ray bursts* (GRB) and *Active Galactic Nuclei* (AGN).

Pulsars

A pulsar is a highly-magnetized rapidly rotating neutron star that emits beamed radiation and relativistic particles. Due to the rotation of the neutron star, the beam is experienced from Earth as a light-house like pattern once it is directed towards Earth. When a star reduces in size due to the core-collapse, the new born neutron star starts rotating very rapidly to conserve angular momentum and the magnetic field strength starts to rise. This causes the acceleration of charged particles from near the magnetic poles of the neutron star and results in beamed radiation. The neutrino flux $\Phi * E^2$ spectrum associated with the particle generation in pulsars is postulated to have its maximum around 10^{17} eV [26].

Gamma Ray Bursts

During some supernova or during the merger of binary neutron stars, extremely luminous gamma ray transients are generated which is a source candidate for neutrinos, which can be identified provided that the jet is pointed towards Earth. In some cases, the jet does not fully escape the star, which is the low-luminosity GRB subclass. While they are lower in intensity, they are expected to be brighter neutrino sources than regular GRBs where the jet fully propagates [27]. Because the jet is stuck within the envelop of the star, neutrinos can efficiently be produced by cosmic rays interacting with ambient matter, as in equation 2.4. Besides, the low-luminosity GRBs, also the GRB afterglow, which is a longer lasting emission of longer wavelengths caused by the collisions between the burst and the interstellar gas, is predicted to produce high energy neutrinos [28].

Active Galactic Nuclei

A galaxy with a supermassive black hole at its centre which accretes sufficient material to produce significant electromagnetic radiation is categorised as an *Active Galactic Nuclei* (AGN). The neutrino production from AGNs is predicted to even outshine the production of cosmogenic neutrinos and PA has shown that the arrival directions correlate significantly with AGNs [29; 30]. A sub-category of AGNs are the *blazars*, which is an AGN with the jet directly pointed towards Earth. The blazar was one of the first sources to be suggested as high-energy neutrino producer. Shown is that blazars dominate the contribution to detected gamma rays by Fermi and they are predicted to produce neutrinos in the ultra-high energy regime [31; 32].

The blazar TXS 0506+056 has been identified as the first 3-σ source of neutrino production due to a high energy neutrino that coincided spatially as well as temporally [19]. Other promising candidates are Markarian 421 and Markarian 501 which are the brightest sources in the TeV range [33; 34]. Above this energy range gamma rays get attenuated and therefore it is probable that more distant blazars are also bright in gamma rays at TeV energies but not observable.

2.3.2 Cosmogenic Neutrinos

The current largest detectors aiming for the highest energy cosmic-ray range are PA and Telescope Array (TA), which probe cosmic rays at the highest energies. Since the fluxes at these energies are so low, the reason for the cut-coff is still under debate, as described in section 2.2.2. Also, the measured compositions of PA and TA vary significantly, albeit compatible within the systematic uncertainties, and claims a disfavoring of a pure proton composition [35; 36]. To solve this problem, besides building larger detectors in order to increase the statistics, a measurement of the cosmogenic neutrino flux will be helpful, since it is an indicator for the cosmic-ray composition. The cosmic-ray composition influences the threshold for the GZK cut-off in which a heavier cosmic-ray composition results in a lower neutrino flux prediction. Only protons undergo photopion production, yielding a higher energy threshold (linear increasing with the mass) for the cosmic ray to undergo the GZK effect [37]. The main loss process for heavier nuclei is photodisintegration, in which no leptons are produced. Besides the mass composition, the cosmogenic neutrino flux can constrain the source evolution since sources are required to have redshifts beyond the GZK horizon, resuling in a larger expected neutrino flux for high redshift sources (like AGNs and GRBs) than nearby sources (Tidal Disruption Event (TDE)). Furthermore, the cosmogenic neutrino flux will constrain the parameter space in the spectral index of the injection at the source and the maximum source energy [38; 39]. Based on the measured cosmic-ray spectrum from TA and PA and mass composition measurements of PA, cosmogenic neutrino fluxes can be expected as indicated in figure 2.1 in the dark-yellow lines [40; 39]. If the highest energies cosmic rays contain a fraction of protons (which is allowed by the PA cosmic-ray data), stemming cosmogenic neutrinos can be used for cosmic-ray astronomy, since the deflections of the highest energy protons in the magnetic fields, although highly dependend on magnetic field models, is little [41].

2.4 Multi-Messenger Detection Techniques

Satellites, like the Fermi Space Telescope, have been probing the gamma ray flux at the lower-energies until 300 GeV from space [42], as indicated in figure 2.1. For higher energies however, the flux is dropping significantly and satellites are too small to be sensitive to this regime. Therefore, gamma rays beyond the range of the Fermi telescope need to be detected with earth-based instruments. When a gamma ray undergoes pair production in the Earth's atmosphere, a cascade of particles is created, which is called an *air shower*. This cascade of particles travels slightly faster in the air than light, which causes the emission of Cherenkov light. This Cherenkov light, being faint, ultraviolet and of short duration, is not detectable with the human eye, and therefore large mirrors and high-speed cameras are instrumented for this detection (an Imaging Atmospheric Cherenkov Telescope (IACT)). This approach is used by current earth-based gamma ray detectors like VERITAS [43], H.E.S.S [44] and MAGIC [45] and is continued by the Cherenkov Telescope Array (CTA) [46]. For even higher energies (up to PeV energies) water Cherenkov detectors are used, which detects with photomultiplier tubes (PMT) the Cherenkov light dat is results from high-energy particles striking the water as done by HAWC [47] and LHAASO [48].

Similar for cosmic rays, the number reduces quickly for higher energetic particles and earth-based detectors need to be used for their detection. Interactions with the Earth's atmosphere lead to the emission of Cherenkov light and a cascade of particles. The main technique used to identify cosmic rays is by observing the particles that reach ground level, either by short burst of UV light while plastic scintillators are reached or by water Cherenkov detectors. Furthermore, either the fluorescence light can be detected with PMTs or the radio emission with antennas, which are both stemming directly from the air shower. The lead in cosmic-ray observatories is the 3.000 km^2 PA with a measured spectrum indicated in figure 2.1.

Both the gamma-ray and the cosmic-ray spectrum at the higher energy end are inferred by using air as a detection medium and then using dedicated equipment to detect the created air showers. The atmosphere, however, is transparent for neutrinos due to their very low cross-section and consequently more dense matter is needed for neutrino detectors. Various detector media are currently used surrounded by PMTs to observe the Cherenkov light emitted by the secondary particles due to the neutrino interaction, like high-purity water used by Kamiokande [7]. Also, radiochemical approaches in which a neutron is converted to a proton due to inverse beta decay (SAGE) are used to identify neutrino signatures [49]. For the latter, however, only the presence of a neutrino can be noted, but information about the flavour, direction or energy gets lost.

For the high energy neutrinos, natural volumes are needed for the detection as the flux is so low that it would otherwise make the experiments infeasible. For this energy range the detection of the emitted Cherenkov light is used in natural media like water (ANTARES, Km3NET) and ice (IceCube) [8; 50; 12]. PMT sensors are located in the detection media itself. IceCube is currently the largest neutrino detector with a covered volume of 1 km^3, which resulted in neutrino data up to the PeV range as indicated in figure 2.1. For probing the neutrinos above this energy, larger volumes need to be covered as the sensitivy for the current IceCube flux for the higher energies, as indicated with the solid blue line in figure 2.1, is above the expected flux. IceCube-Gen2 would be the extension of IceCube with sensitivities until EeV energies [51].

Also for neutrinos, the radio emission instead of the optical light emitted can be used for detecting the particle shower. There is a spatial disbalance in the shower between the positive and negative charged particles, leading to radio emission, as will be explained in section 3.1.1. A possible medium for radio detection of neutrinos is ice. While optical light gets easily scattered and absorbed in ice, radio waves can propagate hundreds of meters, which makes the radio detection technique suitable for covering larger volumes. The radio technique is established for the detection of cosmic rays, and pilot arrays for neutrino detections are running for technique verification as will be described in chapter 2. RNO-G is planned to be the first deployed radio detector with sensitivities reaching the energy scale beyond the IceCube detected spectrum. As a next step, the radio technique is planned to be a part of IceCube-Gen2 [51].

Chapter 3

Radio Detection of Neutrinos

siku.

— *Greenlandic for* Ice in general

Radio waves travel hundreds of meters in ice due to the long attenuatio lenght and therefore, detectors using the radio waves occuring from neutrino induced in-ice particle showers can be build very sparse. Therefore, they are a good potential to for the frist time probe the flux at the highest energies. Besides neutrinos, any particle shower in a dieelectric medium will be emit electromagnetic radiation, as it is extensively used for the detection of cosmic-rays by their air-showers. Section 3.1 explains the creating of radio emision of particle showers. The radio technique is well established and has shown to work reliable for cosmic-rays, as described in section 3.2 what makes it promising for the usage of neutrinos. Then, section 3.3 will focus on detecting neutrinos due to the created radio emission. It introduces the requirements for a good neutrino radio detector, and it describes several media suitable for radio neutrino detection. Next, the experiments using ice as a detection media are outlined. Section 3.4 illustrates the expected radio signature in in-ice radio neutrino detectors. Besides neutrino signals, radio detectors will detect lots of data due to the various backgrounds. Section 3.5 describes the radio backgrounds for in-ice radio neutrino experiments, including some first analysis of RNO-G data and identification of background events by the RNO-G hardware. Then, in section 3.6, more focus is being laid on the ice properties, since knowledge of the detection medium is of great importance for proper station calibration. It discusses the important properties of ice for in-ice radio neutrino detectors and the specifics for Greenland ice sheet, where RNO-G is located. Finally, neutrino properties reconstruction in introduced, and in specific the requirements to obtain the neutrino arrival direction.

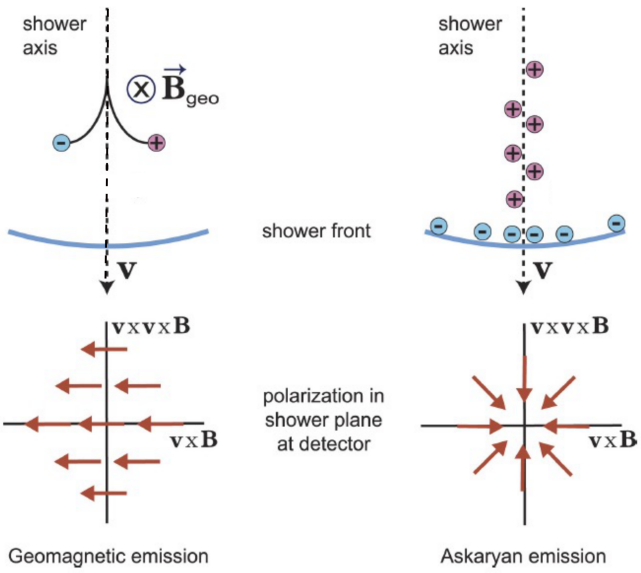

Figure 3.1: Charge seperation in the shower and the resulting direction of the polarization for the geomagnetic effect (left) and the Askaryan effect (right). Figure adapted from [52].

3.1 Radio Emission from Particle Showers

The radio emission that is detected by in-ice neutrino detectors is emitted by the particle shower created due to the neutrino interaction with a nucleon in the ice. As Askaryan already proposed in 1962: Any electromagnetic cascade in a dense dielectric medium should produce observable, coherent radiation [53; 54]. He originally proposed this for cascades produced by cosmic-ray interactions. While for cosmic rays mainly the Earth's atmosphere is used as the interaction medium, more dense media, like ice, are currently being explored for neutrino detection, since the atmosphere has a low density and neutrinos have very low cross sections. The development of the radio-emitting particle shower in-air is very similar to a neutrino-induced in-ice shower.

The first interaction of a cosmic-ray air shower, is the interaction with a nucleon in the Earth's atmosphere. The interaction produces mostly pions and other hadrons, such as kaons, protons and neutrons. In various processes that follow, lots of particles are created which can be divided into two components: the *electromagnetic component* and the *hadronic component*. The *electromagnetic component* of the shower consists of electrons, positrons and photons. Whereas the neutral pions decay into photons ($\pi^0 \rightarrow \gamma + \gamma$), electron and positron pairs are created by a photon ($\gamma \rightarrow e^- + e^+$) and photons are created by Bremsstrahlung ($e^\pm \rightarrow e^\pm + \gamma$).

The charged pions and the remaining protons and neutrons fuel the hadronic component of the shower. As long as their decay length is larger than their interaction length, the high-energy charged pions will continue to interact with nuclei in the atmosphere, creating more pions and expanding the shower. Other produced particles are muons and muon neutrinos which are created when charged pions decay. During the shower development, the secondary particles lose energy, until the interaction length becomes longer than the decay length, creating muons and neutrinos.

3.1.1 Askaryan Effect and Geomagnetic Effect

The positive and negative particles in the moving shower will be separated causing a current. The current, caused due to this charge seperation, is changing over time due to the number of particles in the shower that is increasing and decreasing during the development. This results in the emission of nano-second long radio pulses.

One of the mechanisms causing this charge seperation is called the *Askaryan effect*, as it was proposed by Askaryan himself [53]. A negative charge excess builds up at the shower front, mainly from Compton scattering of cascade photons on atomic electrons. The radio signal emitted due to the Askaryan effect, is because of the build up of electrons in the shower front, with respect to the positive ions of the medium along the shower axis. Furthermore, positrons from the shower get annihilated with electrons from the medium, adding to the negative charge excess. When the shower reaches its maximum number of particles, the number of electrons can outshine the number of positrons by 20%. [55; 53]. The Askaryan effect results in a polarization of the electric field towards the shower axis. This is illustrated in figure 3.1 left. Already proposed in 1962, the first verification of the Askaryan effect in the lab was in 2001 by a series of beam test at SLAC in silica, and later on in 2006 it was reproduced for ice. In air, which is a non-dense media, charge-excess only plays a minor role [53; 56; 55].

For in-air shower development, the Earth magnetic field causes the charge separation in the shower, the *geomagnetic effect*. Because of the Earth's magnetic field, a Lorentz force is created, separating the positive and negatively charged particles perpendicular with respect to the shower axis, due to

$$\vec{F_L} = q \cdot \vec{v} \times \vec{B}, \tag{3.1}$$

where q is the particle charge, $\vec{v}$ the direction of the cosmic ray and the propagation direction of the shower and $\vec{B}$ is the Earth magnetic field. This results in an orientation of the emitted electric-field perpendicular to the shower axis. Accept for muons, who have a too large rigidity, all charged particles in the showers contribute to the geomagnetic effect.

For air showers, the contribution of the Askaryan effect to the radio emission is highly dependent on the Earth magnetic-field strength, and the direction of the shower compared to the magnetic-field direction. The fraction of the contribution of the Askaryan effect to the radio emission is estimated between 3 and 20 percent at the LOFAR site (Drenthe, the Netherlands) [57]. For in-ice shower development, the mean free path of the electrons and positrons is too small to cause a transverse charge separation and therefore the geomagnetic effect can be neglected. Since only the Askaryan effect is important for in-ice showers, only the electromagnetic part of the shower plays a role in the emission.

3.1.2 Coherent Emission

The particles in the shower travel near the speed of light, which is larger than the speed of the emitted radio emission, which travels with $v = \frac{c}{n}$, with c the speed of light in a vacuum and n the index of refraction of the medium. Therefore, the radio emission is more restricted in the traveled distance than the propagating particles, resulting in an emission angle with

respect to the propagation direction of the particles of

$$\cos(\Theta_C) = \frac{1}{n} \tag{3.2}$$

which is the Cherenkov angle. Whereas the refractive index depends on the specific interaction point in the medium, this results in an $\approx 1^\circ$ cone for cosmic rays ($n_{\text{air}} = 1$) and $\approx 55.8^\circ$ in ice ($n_{\text{ice}} = 1.78$). For wavelengths longer than the size of the shower perpendicular of the shower axis, the emission adds up coherently. Therefore, this radio emission is detectable and strongest near the Cherenkov angle. While cosmic-ray air showers can have lengths at the kilometer scale, the size significantly drops for dense media, due to the linear dependence of the interaction length λ with the number density n, $\lambda = \frac{1}{n \cdot \sigma}$ with σ the cross section. The longitudinal dimension of a particle shower in ice is ≈ 10 meters and the width is ≈ 10 cm.

3.2 Radio Detection of Cosmic-Ray Air Showers

In the 1960s, first experimental activities were performed to relate radio pulses with extensive air showers. Even first relations between radio emission and air-shower parameters were established [58]. However, due to lack of sufficient data taking techniques (because man-made interference could not be filtered out, the absence of digital data recording and the usage of very small bandwidths were used ($\mathcal{O}(4MHz)$), the activities were ceased. 40 years later, LOPES was the first to detect cosmic rays with radio antennas, using a bandwidth of 30 MHz. However, back then the radio emission was still assigned to geosynchroton emission [59]. Besides LOPES, CODALEMA rediscovered the field of cosmic-ray detection with radio [60; 61] . Both have currently stopped taking data. Since then, various experiments did cosmic-ray radio detection, like LOFAR, AERA and Tunka-Rex [62; 63; 64].

Radio detection of cosmic rays has shown to work reliably and give similar results as particle detectors [65]. LOFAR has been able to map out a complete air-shower footprint, due to the large density of antennas, and has identified the expected interference between the geomagnetic and charge excess component, which results in a *bean-shaped* pattern for the spatial distribution of the radiation energy [66]. Excellent agreement of data with advanced simulation codes like CoREAS and ZHAires shows that the radiation mechanisms are very well understood [67; 68; 69]. Since radio detection of air showers has proven itself to be well understood and has grown in the last 20 years to a standard-technique, application for detectors optimized for neutrino detections is promising.

3.3 Radio Detection of Neutrino induced Showers

Because neutrinos have very low cross sections, very dense media are needed, and because of the low flux of high energety neutrinos, only big volumes are feasible as neutrino detectors.

3.3.1 Detection Medium Requirements

As a measure for the performance of a neutrino detector the *effective volume* is used, which is given by

$$V_{\text{eff}} = V \cdot f(E) \cdot \frac{\rho_{\text{medium}}}{\rho_{\text{water}}} \tag{3.3}$$

where V is the total volume of the detection medium, $f(E)$ is the fraction of neutrinos interacting in that volume that are detected and ρ_{medium} and ρ_{water} are the densities of the medium and water, respectively. Typically, the water equivalent of the effective volume is given, for inter-experiment comparisons and therefore the effective volume of the detector is multiplied by the ratio of $\frac{\rho_{\text{medium}}}{\rho_{\text{water}}}$.

The effective area is then given by correcting the effective volume for the interaction length $L_{\text{int}}(E_\nu, \rho)$ of the neutrinos:

$$A_{\text{eff}} = \frac{V_{\text{eff}}}{L_{\text{int}}(E_\nu, \rho)}, \qquad L_{\text{int}} = \frac{M_N}{\sigma(E_\nu)\rho} \tag{3.4}$$

with M_n the mass of the nucleon, E_ν the neutrino energy and ρ the average density along the path of the neutrino.

Given a diffuse neutrino flux $F(E_\nu)$, the number of detected neutrino events for an experiment is then given by:

$$N = \int dE_\nu F(E_\nu)\epsilon(E_\nu)4\pi \tag{3.5}$$

with $\epsilon(E_\nu)$ is the time integrated effective area.

An important key in maximizing the number of events N is choosing a detection medium for a maximum effective volume. Besides that large natural volumes need to be available, an important factor of the medium to observe radio emission (and therefore to maximum the V_{eff}) is the dielectrivity; the medium needs to be somewhat transparant to radio. The field attenuation factor L_{attn} is defined to be the distance over which the distance-corrected electric field E drops by a factor of $1 - \frac{1}{e}$. At a distance r:

$$rE(r) = E(0)e^{\frac{-r}{L_{\text{attn}}}}. \tag{3.6}$$

Furthermore, the density ρ of the medium is important, since a larger density reduces the interaction length of the neutrino which increases the effective area.

3.3.2 Quest for Neutrino Detection Medium

Several media have been suggested for detecting neutrinos with the radio technique, like salt, ice and even extraterrestrial volumes like the Moon.

Salt is very dense, and therefore neutrinos are more likely to interact compared to neutrinos propagating in-ice. Neutrino detectors were suggested in natural occurring salt caves, consisting of 100 million year old sea salt, like Cote Blanche [70]. In general these salt mines are shielded with bedrock which blocks backgrounds such as Galactic noise and cosmic rays.

Furthermore, the Cherenkov angle in salt is larger than in ice, and the Cherenkov emission has a broader spectrum to the smaller shower, adding to the effective volume [71]. Whereas the attenuation length depends a lot on the moisture content and the composition of the salt, it was measured to be 63 meter for 300 MHz (250 meter for 200 MHz) at Cote Blanche for, significantly smaller than for ice (see section 3.6).

Various experiments have been studying neutrino interactions in the regolith of the Moon, Jupiter or Saturn as a detector media with earthly based radio-detectors [72; 73]. These experiments are sensitive to very high energy neutrinos due to the large volumes they can cover, setting the current limits for the highest energy regime. The NuMoon experiment is sensitive above 10^{20} eV, which is above the GZK cut-off (section 2.3.2) and therefore limits are mainly set on exotic models [72]. The analyses of these experiments, however, involve large uncertainties due to the many unknowns of these extraterrestrial environments, e.g. the assumption between experiments of the depth of the lunar regolith varies from 10-500 meters.

Searches for radio signals stemming from neutrino interactions in large ice volumes have been performed using satellites, balloons and embedded experiments. The further away a detector is from the interaction position, the higher in energy the lower end of the sensitivity spectrum is. The signal amplitude drops down due to the propagation, and therefore the energy needs to be very large in order to still be detectable several kilometers away (or thousands, for space inhabitant detection volumes). This holds for balloon and satellite experiments. The FORTE satellite looked for 30-300 MHz radio waves as it passed over Greenland in 2003 and ANITA, a balloon experiment, which had its final and fourth flight in 2016 [74; 75]. Balloon exhibitions can search large ice volumes, but due to their far-away distance, they are only sensitive starting from 10^{18} eV. Furthermore, the livetime of balloons is very limited, which impacts the effective volume of the experiment. Furthermore, since balloons are constrained in size, the angular resolution for embedded experiments is better.

3.3.3 In-Ice Neutrino Detectors

The embedded experiment that set the first limits on in-ice neutrino interactions with radio was RICE in 1999, which deployed antennas in the holes drilled by the AMANDA experiment (precursor of IceCube) at the South Pole [76]. Since then, in 2006, 3 deep in-ice radio frequency clusters were deployed at depths of $\approx$ 1300 meter and $\approx$ 300 meter on top of the IceCube strings, known as AURA [77]. Currently, two pilot-arrays for the in-ice radio detection technique are running smoothly in Antartica: ARA and ARIANNA.

Whereas an ARA station contains four 200 meter deep strings (*deep component*), an ARIANNA station consists of four log periodic dipole antennas (LPDA) buried near the surface (*surface component*). Both experiments have been running for more than 10 years, and although the current detectors are too small to be sensitive for neutrino detections [78; 79], lots of work has been put in understanding the in-ice detection technique. ARA uses the coherent sum of eight close-by located antennas as trigger, a *phased array*, to be able to trigger on a very low signal amplitudes [80; 78], still obtaining an analysis efficiency of $\approx$70% [81]. ARA is located at the South Pole and has a large effective volume due to the deep, low-threshold trigger. ARIANNA is located at the Ross Ice Shelf, which is on top of the

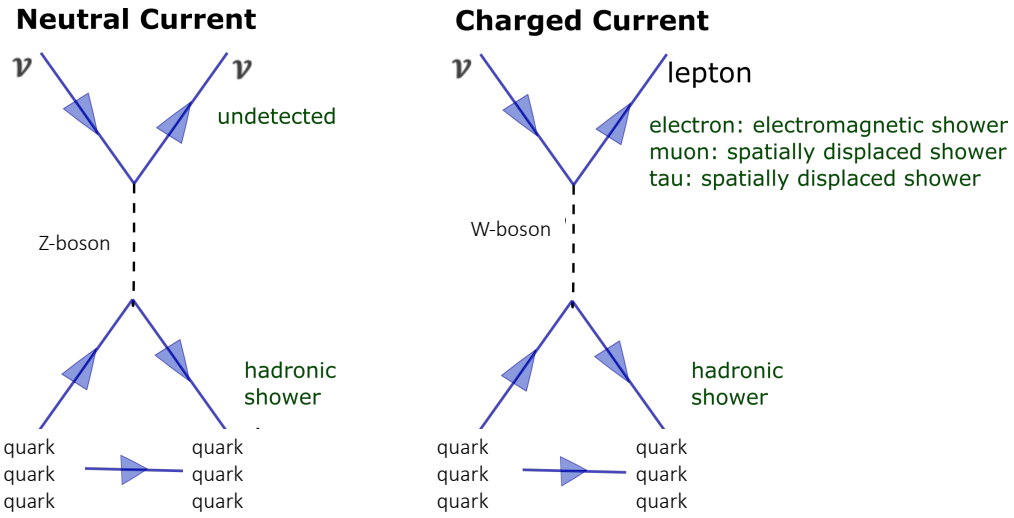

Figure 3.2: Feynman diagrams of a charged current and neutral current neutrino interaction.

Ross Sea. The shallow detector gains in effective volume due to the reflected signals of the ice-air and ice-water boundary, although it is still small compared to a deep detector, like ARA. Because the ARIANNA antennas are close to the surface, upward pointing installed antennas are used for cosmic-ray detection, which can be used as proof-of-principle for neutrino detection [82; 83]. ARA is powered by South Pole station and the ARIANNA stations are autonomous using solar- and wind power [84].

As will be discussed in section 4.2, an RNO-G station will use the expertise of ARA as well as ARIANNA by using a *hybrid* station: three deep strings, including a phased array trigger, and a component close to the surface as will be discussed in section 4.2. In the next three years, RNO-G will be completed with 35 stations. With that, RNO-G will be sensitive to optimistic cosmogenic- and astrophysical neutrino fluxes and therefore RNO-G will be the first radio detector to make either a neutrino detection in radio or exclude realistic models.

Furthermore, a similar hybrid station is planned to be part of the next generation of IceCube, IceCube-Gen2 Radio, covering 500 km^2 [51]. Other future neutrino detectors using the radio technique are PUEO [85] , GRAND [86] and RET [87]. While PUEO is a balloon experiment, the follow-up to ANITA, GRAND is a ground based experiment that will focus on near-horizontal tau neutrinos interacting in the Earth and RET will focus on identifying in-ice particle showers by the reflection of radar.

3.4 Radio Signature of In-Ice Neutrino Interactions

The specific signature of the radio emission depends on the flavor of the neutrino and the type of interaction the neutrino undergoes.

3.4.1 Neutrino Interactions

The deep inelastic reactions of neutrinos with a proton or neutron in the ice can undergo a neutral current (NC), or a charged current (CC) interaction, where the reaction is due to

exchange of the Z-boson and W-boson respectively. The ratio of these interactions is estimated to be roughly 0.7:0.3 for CC:NC slightly varying with energy, for energies between 10^{16} and 10^{21} eV [88]. In case of the CC interaction, a charged lepton of the corresponding neutrino flavour is created. In NC as well as CC-cases, a hadronic shower is induced like visualized in figure 3.2. The electromagnetic part of this shower (created due to the decay of neutral pions into two photons $\pi^0 \rightarrow \gamma + \gamma$) emits the detectable radio emission, however a fraction is transferred to the hadrons, which are undetectable.

3.4.2 Secondaries

For NC interactions, all flavours give similar signatures, i.e. a hadronic shower is created and the outgoing neutrino remains undetected. For CC interactions, besides the hadronic shower, additional showers may occur depending on the flavour of the neutrino. The showers created by the outgoing lepton can be detected as a superposition with the shower of the first interaction, or isolated without the counterpart. These additional interactions add to the effective volume of a neutrino detector. For tau neutrinos the correction is strongest at the PeV scale with an additional 60%, while at high energies the correction is roughly 25% [89].

Outgoing muons due to muon neutrino interactions can undergo catastrophic energy losses, mainly due to Bremsstrahlung, pair production and photonuclear interactions during their track in the ice.

Created taus will decay, resulting in a hadronic shower for hadronic decay channels, and an electromagnetic shower for electrons. For a tau with energy in the PeV range, the decay length will correspond to roughly 50 meter and therefore this could be seen as a *double bang* signature. The tau track length increases linearly with energy, and therefore for low energies the showers will overlap and for high energies the double bang might be out of reach of the detector, and will not be seen, or only isolated without counterpart. Furthermore, also taus undergo catastrophic energy losses, due to photonuclear interactions, Bremsstrahlung and pair production [90]. High energy showers could trigger an in-ice radio detector, and additionaly the coherent adding of low energy showers could be seen by the detector. Whereas overall it is hard to distinguish a tau-track from a muon track, for a tau decaying into a muon, the catastrophic tau-track will morph into the catastrophic muon-track, which with a dense enough detector array might still be distinguishable because the average energy losses for taus are smaller than for muons [90].

For electron neutrinos CC interactions, the outgoing electron induces an extra electromagnetic shower. The electromagnetic part of the shower is influenced by the LPM effect, which leads to an elongation of the shower [91], which has a pronounced effect for higher energies. However, at these energies, processes like photonuclear and electronuclear interactions become important, which limits the grow of the shower length. At low energies the electromagnetic and the hadronic shower are created at the same place and the radio emission interferes mostly constructively. At high energies, the shower maximum of the electromagnetic shower can be far away from the hadronic shower, causing interference of the individual pulses.

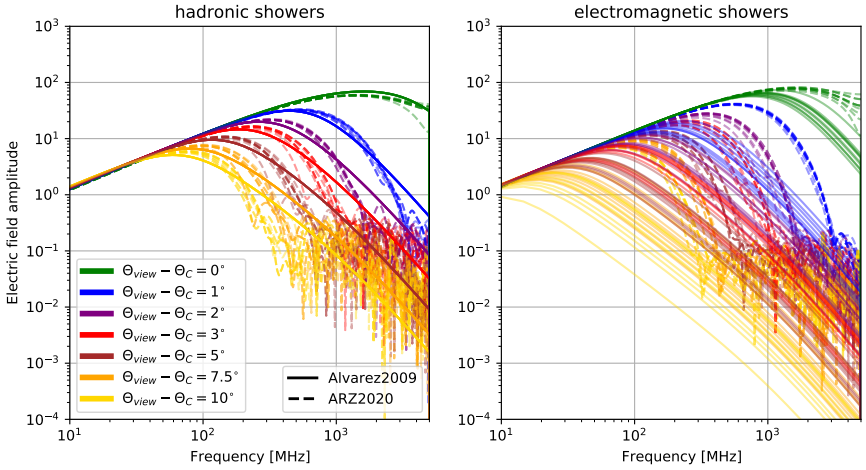

Figure 3.3: Electric fields for different viewing angles for the *ARZ2020* and the *Alvarez2009* model. Further away from the Cherenkov angle the higher frequencies lose coherence. Left: hadronic showers. Right: electromagnetic showers. For electromagnetic showers, the cone width is reduced due to the LPM effect.

3.4.3 Radio Signature

The radio emission is coherent for wavelengths longer than the transverse size of the shower (Moliere radius, roughly 10 cm), which corresponds to frequencies of roughly 1 GHz, where the signal is strongest. The signal distribution around this angle can be approximated with a narrow Gaussian distribution. For lower frequencies, the signal gets weaker but the angular distribution gets much broader, i.e. coherence disappears first for higher frequencies for more off-cone angles. Depending on the distance of the interaction vertex, signal can be detected roughly 7° away from the Cherenkov angle. The electric-field for a variety of off-cone angles, also *viewing angles*, which is defined as the opening angle between the shower axis and the signal, is shown in figure 3.3 for two different electric-field models (which will be explained in chapter 4). Figure 3.3 left shows the spectrum for hadronic showers and figure 3.3 right for electromagnetic showers. For electromagnetic showers, the cone width is reduced with respect to the hadronic showers due to the LPM effect. For viewing angles on opposite side of the cone, but same $\Delta\Theta$, the electric-field is very similar; the frequency spectrum is almost symmetric with respect to Θ_C.

3.5 Noise and Background for In-Ice Neutrino Detectors

Since no radio emission stemming from an in-ice neutrino interaction has ever been detected, a good understanding of the radio backgrounds is needed in order to verify that an observed signature is indeed a neutrino. A good grasp of how the noise behaves as well as any impulsive events coming from the surroundings is required. The noise that radio detectors have to deal with are among others thermal noise, galactic noise, man-made impulsive events and the muons from cosmic-ray air showers. A short overview of these backgrounds are given including some practicalities for RNO-G.

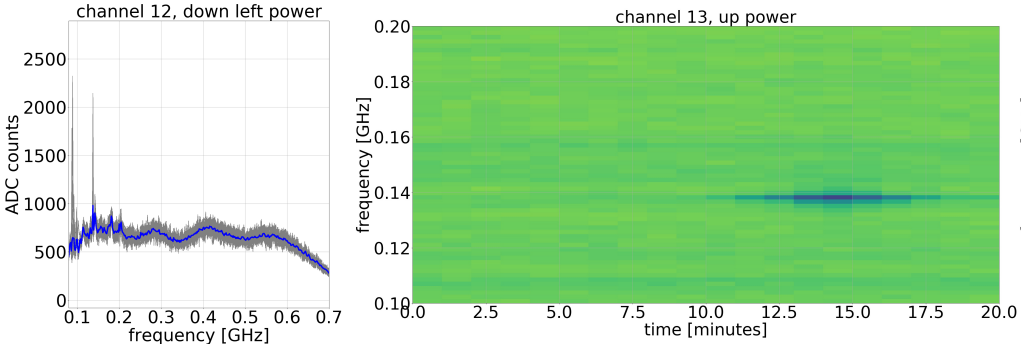

Figure 3.4: Left: Averaged forced trigger spectra used to identify time-variations. The clear peak at 158 MHz is a radio. Right: Spectrogram relative to the averaged spectrum to identify time-variations. The 137 MHz frequency is most likely a satelite [96].

3.5.1 Thermal Noise

Neutrino radio detectors are roughly sensitive from 10^{16} eV (although this highly depends on the geometry of the event), because the emitted pulse needs to be distinguished from the thermal noise of the antennas. Low threshold triggers have been designed in order to detect very low-threshold events, like the phased array trigger used by ARA and RNO-G. The thermal noise is completely determined by the temperature of the system, and caused by the thermal agitation of the electrons in the antenna. It can be calculated with

$$P = k_B T \Delta f \tag{3.7}$$

where k_B is Boltzmanns constant, Δf the bandwidth, T is the system temperature [92]. In general, thermal noise is modeled as Gaussian distributed amplitudes, since it the superposition of thermal fluctuations of many individual electrons, which is a Rayleigh distribution in frequency domain. While the thermal noise is antenna response independent, the noise spectra can differ for each antenna due to the specifics of the system.

3.5.2 Galactic Noise

For the surface detector, the Galaxy, and moreover the galactic plane, is contributing to the received radio signal causing a irreducible noise floor. The galactic noise follows an exponential spectrum throughout the entire MHz band [93]. RNO-G is not sensitive to the galactic centre, and since most emission is coming from the galactic plane, the noise contribution is expected to be constant over time [94]. Furthermore, the galactic noise is expected to only be seen in the surface channels of RNO-G and not in the deep channels, due to the deep position in the ice, as well as that all the antennas in the ice are not sensitive in the vertical direction. For the upward-pointing surface antennas, the galactic noise was shown to be comparable with the thermal noise up to 110 MHz and only a small fraction of the noise-contribution for higher frequencies [94]. ARIANNA has demonstrated its ability to resolve the galactic plane with similar surface antennas as RNO-G [95].

3.5.3 Man-made background

Most radio neutrino experiments are in remote areas, which means that overall they are nicely shielded against man-made radio signals. However, radio detectors are often located near facilities in order to allow for installation and deployment, which are a source for

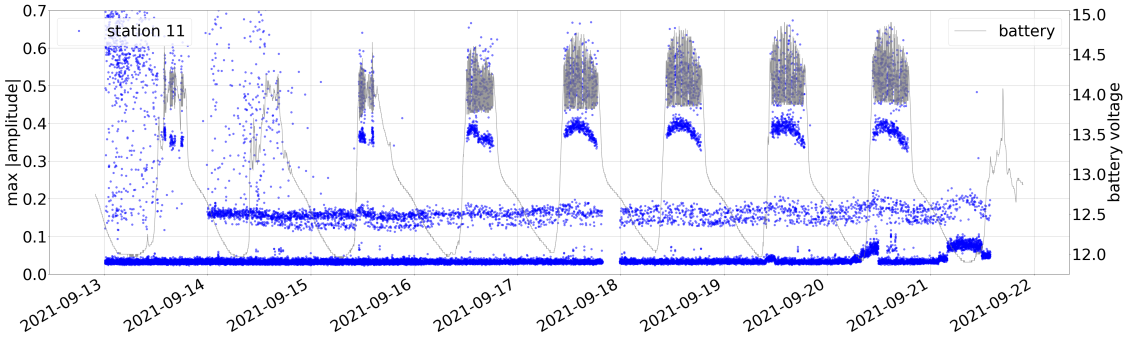

Figure 3.5: Nine days of data for an RNO-G station (blue) and the voltage of the batteries (grey). Clearly seen is the correlation between the batteries and the high amplitude RFI events.

background pulses. Each remaining source of radio frequencies (RFI) needs to be identified. Whereas ARA has a lot of identified RFI sources [97], the site for ARIANNA is more quiet since it is located at the Ross-Ice shelf near a mountain, which shields it from the noise from the station [98]. For RNO-G, for which the thus far deployed stations are relatively close by Summit Camp, radios (very narrow bandwidth from 151 - 156.8 MHz, most used channel is 151.6 MHz) are identified. Other identified narrow-band lines correspond to air traffic communication (123 MHz). Snowmobiles used for transport at Summit Camp are expected to be seen in the lower frequencies up to 100 MHz. Furthermore, planes arriving/leaving Summit Camp are detectable in the detector as well as satellites. Figure 3.4 shows radios, snowmobiles and a satellite as observed at the RNO-G site.

Also, the initial RNO-G hardware contributes to the noise. Figure 3.5 shows for a two week period for an upward facing antenna near the surface (LPDA, as will be described in section 4.2.3) the maximum amplitude of the envelope of the trace for forced- as well as threshold triggers. As can be seen, three different kind of events can be identified by comparing the maximum amplitude. From bottom to top we refer to them as *noise floor*, *first-row* events and *second-row* events. This amplitude distribution is noticeable in all three stations, with comparable amplitudes. The *first-row* pulses are very large in a small frequency-band of 80-100 MHz. They are a 0.2 ns double pulse each minute, which corresponds to the LoRaWAN communication network which transfers data each minute to Summit Camp. The *second-row* events happen in 8 hour very abrupt episodes. The data of the *second-row* events match very well with the discrete behaviour of the voltage of the batteries, as well as the current of the solar panels. Figure 3.5 shows the voltage of the battery matched with the data of station 21 during 9 days of data taking. Spectrograms for both events are shown in appendix A. For future seasons, the RNO-G hardware will be fixed to overcome the deadtimes due to these RFI events. Most likely radio pulses are emitted by the solar panels when the batteries are getting topped off during day time. Furthermore, figure 3.5 shows an abundance of triggered events for the first few days, which can be correlated to the high winds happening during these hours. These *wind events* have also been observed in other radio neutrino experiments [99].

3.5.4 Cosmic Ray and Muon Background

As described in paragraph 3.1, muons will be created in air showers when charged pions decay. Muons will often reach the ground, since their energy is high and the decay time is

long. Therefore, while reaching the ice, the muons will interact with a nucleon in the ice and generate a particle shower which emits radio signals. The radio signature looks very similar/identical to that of a neutrino induced shower, and therefore muons form a background for neutrino detection [89]. The muon flux above 1 PeV has not been measured and predictions highly depend on a large variety of the high energy cosmic-ray flux [100]. Predictions for the number of muons per year for the full RNO-G experiment (35 stations) are between 0.03 and 0.6 per year [89]. Because the muons stem from the remnants of cosmic-ray interactions, detecting the cosmic-ray will give a veto for the muon. RNO-G will use upward facing near surface antennas for this, as will be explain in section 4.2.1.

Additionally, for very vertical cosmic-ray air showers, the shower might not be fully developed before reaching the Earth's surface. In these cases, the particle shower developing in the ice, will emit radio emission. These signals, coming from above, might be reflected on layers in the ice, reaching the detector from within the ice and therefore form a background for neutrino signals [101; 102].

3.6 Ice Properties

A good understanding of the target ice is needed in order to understand the full signature of the radio signal recorded in the detector. Several measurements have been done by glaciologist at the site of RNO-G, Summit Camp Greenland, and by the RNO-G deployment crew during the first deployment season.

The path of the radio signal in the ice is determined by the refractive index profile. In general, the refractive index in ice increases rapidly near the surface, reaching a constant value for deep glacial ice (n = 1.78 for Summit). Due to the changing refractive index, the path the radio signal traverses is refracted and in order to trace back the traversed path of the signal (needed for reconstruction, see section 3.7), a good model for the refractive index profile is required. Furthermore, the rapid change in refractive index at the surface (from n = 1.3 shallow ice to n = 1 in air) causes the signal to reflect from the surface-air boundary, allowing for additional *reflected* pulses to be seen in the detector.

The optimum location for a neutrino detector is in the deep glacial ice, such that the effective volume is optimized due to less refraction. For Greenland this transition is around 70 m.

For radio propagation in glacial ice, the refractive index is related to the density ρ of the ice by [103]

$$n = 1 + 0.845 \cdot \rho \tag{3.8}$$

with ρ in $\frac{\mathrm{g}}{\mathrm{cm}^3}$. Therefore, the refractive index profile can be established by measuring the density of the ice. The depth dependent density of the ice-sheet at Summit has been measured till a depth until 110 meter with two independent measurements. For the first 30 meters a neutron-probe technique has been used which uses a radioactive source of fast neutrons around a cylindrical detector, which scatter with the surroundings [104]. The number of slow neutrons arriving at the detector is a measure for the density of the ice. Further measurements were taken from the surface till a depth of 110 meter by measuring several

ice cores [105]. Densities were computed from measurements of the length, diameter and mass of the various core samples.

Besides that the distance-corrected loss of the radio signal due to traversing the ice highly determines the effective volume of the detector, a correct measurement of the attenuation length is needed for reconstruction of the shower energy (see section 3.7). A measurement of the attenuation length at Summit Camp gives 947 $\pm$ 92 meter for a frequency of 75 MHz averaged over all depths [106]. The set-up consists of a transmitting and a receiving LPDA antenna where signal is reflected off the bedrock and propagates back up in the ice towards the receiving LPDA. The attenuation length is extracted from the gain-loss of the signal. A similar approach has been done during the summer 2021 during the RNO-G deployment for a broad range of frequencies [107]. This resulted in an attenuation length linear decreasing with frequencies, being 900 meters for the lowest frequency of 145 MHz.

The radio array of IceCube-Gen2, will be located at the IceCube site at South Pole. The 2.8 km deep South Pole ice has a longer attenuation length (1450 meters for 380 MHz) than Greenland [108]. Especially for the upper 1500 meters, where most neutrinos are expected to come from, the South Pole ice is much colder than the Greenland ice, resulting in a longer field attenuation length. Near the surface, the South Pole ice is $\approx$ -50°C compared to $\approx$ -30°C for Greenland [109]. A larger field attenuation length causes, besides an increased effective volume, more close-by events to have a larger amplitude. However, it takes longer for the South Pole ice to reach a constant refractive index, i.e. the firn is considered to be 150 meters deep, with respect to 70 meters in Greenland [110] . Therefore, a detector needs to be deployed deeper in the ice in order to optimize the effective volume.

Besides the density profile and the attenuation length of the ice, several other physics plays a role in the huge ice masses, which influences the propagation of the radio emission. Due to the raybending, radio emission from an emitter will not be able to reach all places in the ice, which is called the *shadow zone*. At South Pole, signals were observed from the shadow zone region, which are probably to be explained by the propagation of the radio signal in the firn between ice layers, discontinuities in the density profile: *horizontal propagation* [110]. Such shadow zone propagation has also been observed in the Greenland ice, although being very small [111]. Moreover, several ice layers have been revealed over the full range of the ice sheet at South Pole as well as Greenland which function as *reflective layers*. Also, the South Pole ice has shown to behave anisotropic as ice is a *birefringent* material [112]. Although in lesser degree, the anisotropic behaviour is also observed in Northern Greenland [113]. Good measurements for the RNO-G site still need to be done.

3.7 Neutrino Reconstruction

Since no neutrino has been observed with radio-detectors so far, any identification of a neutrino signal within the haystack of thermal noise would already be a huge achievement. However, to identify the neutrino spectrum or for identification of the cosmic-ray sources, the detector needs to be able to extract more information from the data than simple neutrino-counting. A good detector enables the reconstruction of the neutrino direction as well as energy.

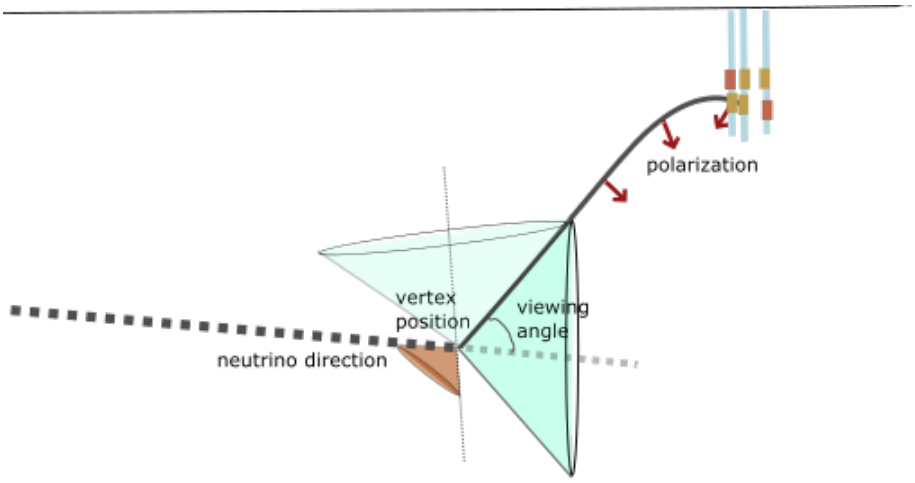

Figure 3.6: Schematic of the geometry of the radio signal detected with an in-ice neutrino radio detector. The neutrino direction depends on the signal direction, the viewing angle and the polarization. The emitted radio emission is indicated by the light blue cone (pointing right). In black, a radio ray is shown propagating to the detector. A measure of only the signal direction and the viewing angle results in possible neutrino directions on a cone, shown in orange. The electric field is polarized towards the shower axis, as indicated with the red arrows and therefore a measure for the polarization direction breaks down the generacy of the neutrino direction.

Figure 3.6 shows the geometry of the radio signal due to a neutrino interaction reaching an in-ice radio detector. Since the radio is emitted on a cone with an opening angle of the Cherenkov angle, a measure of the viewing angle and the signal arrival direction limits the neutrino arrival direction to cone, as illustrated in orange in the figure. Since the polarization is pointed towards the shower axis, the direction of the electric-field contains the information of the position on this cone.

Therefore, a measure of the polarization $\vec{p}$, viewing angle θ_{view} and signal direction l will give enough information to obtain the neutrino direction $\vec{v_\nu}$:

$$\vec{v_\nu} = \vec{p} \cdot \sin\theta_{\text{view}} - \vec{l} \cdot \cos\theta_{\text{view}} \tag{3.9}$$

A good in-ice neutrino detector is capable of giving all three components with good resolution. For the signal arrival direction the time-delays of different antennas are used, which requires a minimum of three antennas for a zenith and azimuth direction. Furthermore, since the arrival direction of the signal at the detectors differs from signal direction at the neutrino interaction point (*vertex*) due to the changing refractive index within the ice, a good ice model is needed. To make a measurement of the polarization, the detector should have antennas that measure orthogonal components of the electric-field. Since the frequency content drops down quickly dependent on the viewing angle, as described in 3.4.3, a measure of the frequency spectrum of the signal gives a measure of the viewing angle, provided that a good model of the electric-field spectrum is available.

The energy of the neutrino can be extracted from the energy fluence in the radio signal. Besides the viewing angle, this depends highly distance to the neutrino interaction vertex. The signal gets attenuated due to the propagation, as well as due to the ice attenuation. A measure of the vertex position can be obtained using the timing-differences between pulses in antennas, and more specifically due to the time-delays of various ray paths. Due to the

ice-air interface, the radio signal can be reflected back from the surface, resulting in a *direct* and *reflected* signal to be detected in the antenna. The reconstruction of the neutrino energy is limited to the energy that is deposited in the particle shower, the *shower energy*. For electron neutrino CC interactions, the full energy of the neutrino is deposited in the hadronic- and electromagnetic shower.

Reconstructing the direction of the incoming neutrino, using the deep station of RNO-G, is the main focus of this thesis as will be outlined in chapter 6 and 7.

Chapter 4

Radio Neutrino Observatory Greenland

nanuq.
— *Greenlandic for* polar bear

This chapter focusses on the description of RNO-G. To indicate the science case of RNO-G, its sensitivities and field of view are described in section 4.1. A practical description follows in section 4.2, describing the lay-out of an RNO-G station aand specifying the hardware that is used in the first deployment round. Then, more information will be given on the location of RNO-G (Summit Camp Greenland) and the deployment, focussing on the first season of summer 2021, including information on the station installation and the mechanical drill that is used to locate antennas deep in the ice sheet (section 4.3). Section 4.4 will focus in more detail on calibration purposes for the RNO-G stations as well as the ice, i.e. calibration pulsers and calibration holes available at the site. Finally, section 4.5 shows selected studies on the optimization of the RNO-G station (string spacing) as well as antenna design as used for the first round of RNO-G stations.

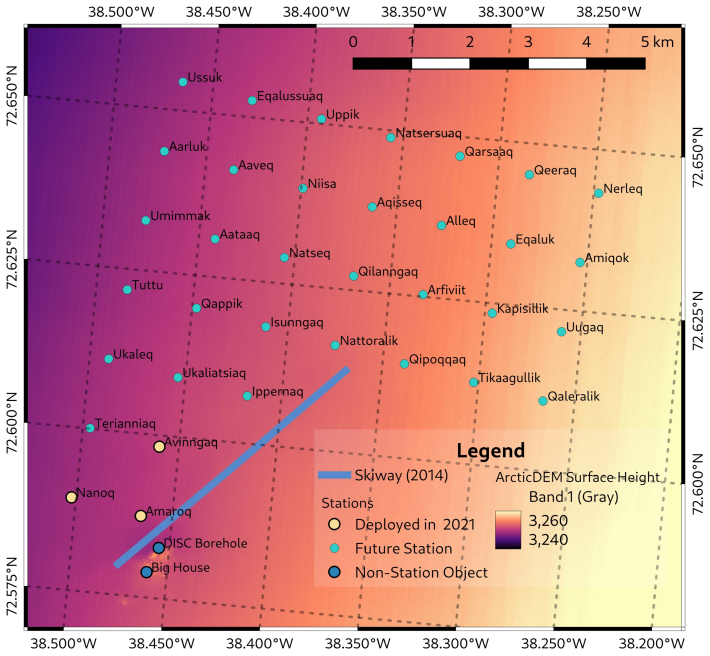

Figure 4.1: The lay-out of the planned RNO-G array. The completed array will feature 35 stations with a spacing of 1.25 km between the stations. The stations are named after animals seen in Greenland. A second naming scheme for stations are two digit numbers following a grid such that the first digit is increasing W-E and the second is increasing in S-N. The currently deployed stations are indicated in yellow. The RNO-G stations are located north from Summit Camp, for which the main communal building Big House is indicated. Furthermore, the DISC hole is marked. Figure from [111].

4.1 RNO-G

The first three stations of RNO-G have been deployed during the summer of 2021 and over the coming 3 years the full array of 35 stations will be completed. Hence, RNO-G will be the first neutrino detector sensitive to detect ultra-high energy neutrinos above 30 PeV or to exclude models for the astrophysical- or cosmogenic neutrino flux in this energy range. A map of all the planned stations is shown in figure 4.1. All stations are named after the Greenlandic name of animals in Greenland. In the first deployment season (summer 2021) the stations Amaroq (=polar wolf, 11), Nanoq (=polar bear, 21) and Avinngaq (=lemming, 22) have been deployed.

The sensitivity of the full RNO-G array for a five year life-time is shown in figure 4.2. The lower edge of the energy regime RNO-G is sensitive to, is due to the irreducible thermal noise of the system, which causes low energy neutrinos of $< 10^{16}$ eV to not be detectable. The station spacing of 1.25 km is optimized to maximize the effective volume such that RNO-G will cover enough volume to be sensitive to neutrinos from the very high energy regime, until 10^{20} eV. Hence, RNO-G will be sensitive to a completely different energy regime than IceCube. Because UHE neutrinos are absorbed when passing through the Earth, RNO-G is mostly sensitive to down-going neutrinos. Therefore, being located in Greenland, the sensitivity is limited to the Northern Hemisphere, which complements the field-of-view of IceCube. The field-of-view for RNO-G is shown in figure 4.3.

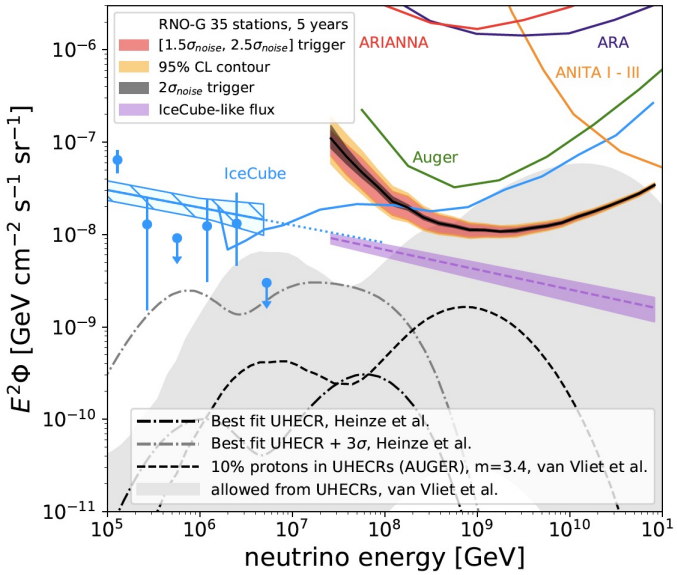

Figure 4.2: The five-year sensitivity (90% CL upper limits) for the complete 35 stations RNO-G array, assuming a 66% up-time. The limits of existing experiments and several predicted fluxes are shown. A dipole trigger is used for a phased array proxy, with a trigger threshold ranging from 1.5 σ_{noise} to 2.5 σ_{noise} . The purple band is the extrapolation for an IceCube-like flux, over the [1.5 σ_{noise}; 2.5 σ_{noise}] trigger range. The figure is taken from [17].

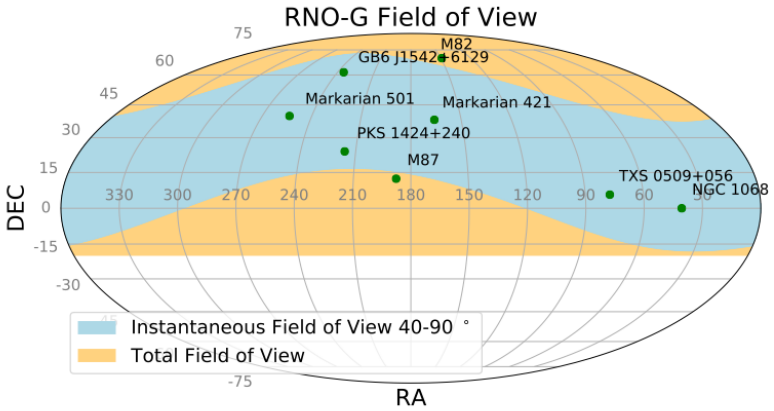

Figure 4.3: The field-of-view for RNO-G in equatorial coordinates, including some interesting candidates. The sky coverage lies predominantly in the Northern Hemisphere. Some significant sources in point-source searches as found by IceCube are located on the map. The blue regime shows the sky coverage for a specific moment in time for the zenith band that contributes the most to the RNO-G sensitivity: 40-90°. Outside this regime the contribution to the effective volume drops significantly. The orange band shows the overall sensitivity.

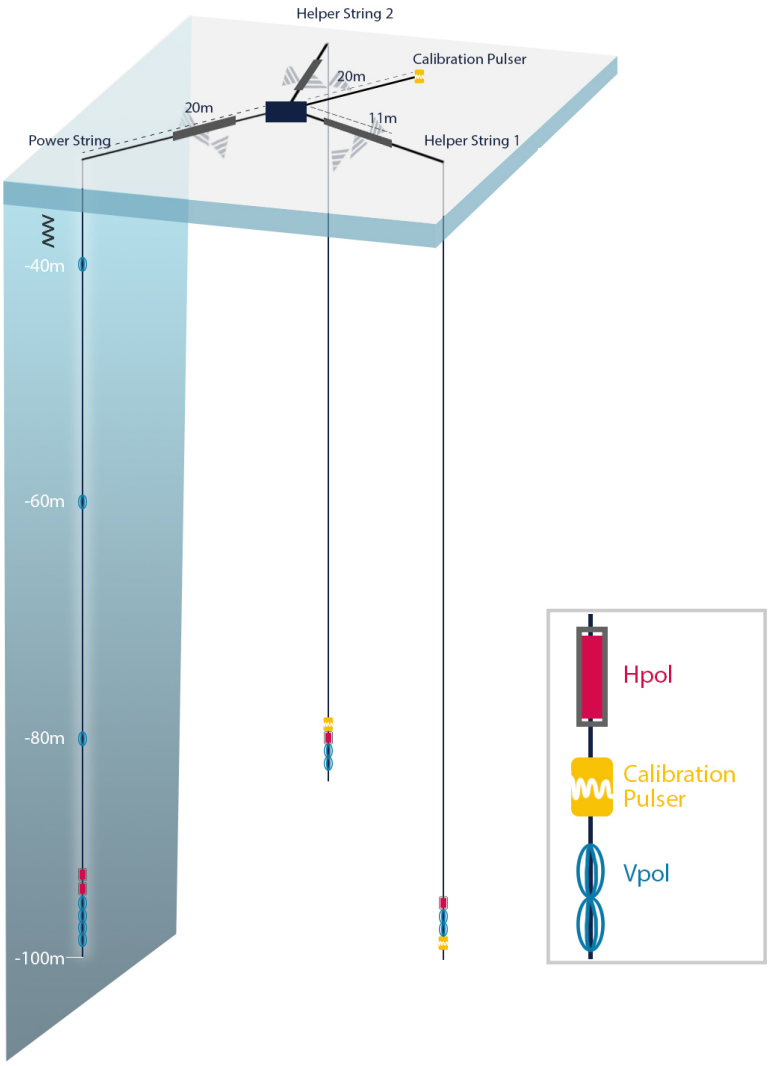

Figure 4.4: A schematic of a single RNO-G station with the *deep* and the *surface* component. The surface component consists of three trenches with three log-periodic dipole antennas (LPDAs) each. There are upward pointing and downward pointing LPDAs, for cosmic-ray as well as neutrino detection respectively.
The deep component consists of three 100 m long strings. The *power string* contains the four vertically polarized (Vpol) antennas that function as the trigger, two additional horizontally polarized (Hpol) antennas for electric-field reconstruction, and more Vpols along the string for vertex distance reconstruction. The other two *helper strings* contain three antennas each and function mainly for azimuthal reconstruction. Furthermore, the helper strings have a pulser Vpol for calibration. An additional calibration pulser is located at the surface. The figure is made by Jack Pairin (IceCube graphics design).

4.2 An RNO-G Station

Each individual station of the full RNO-G array consists of a *deep-* and a *surface component* and therefore makes use of the expertise of ARA and ARIANNA (described in section 3.3.3), respectively. The full layout of a single station is shown in figure 4.4. The surface component is mainly sensitive to cosmic-ray air showers and to neutrinos around the horizon. The deep component contains the low-threshold trigger, and therefore determines mostly the effective volume of the detector. Each surface component contains 9 log-periodic dipole antennas (LPDA) and the deep component is equipped with horizontally polarized (Hpol) and vertically polarized (Vpol) antennas. A measurement of both components of the electric field is needed in order to pin-point the neutrino to its origin, as discussed in chapter 3.

4.2.1 Surface component

The surface component consists of 9 LPDAs located in 3 trenches. Each trench has an LPDA pointing upwards, and two LPDAs pointing 60° down, as shown in figure 4.4. Therefore, the LPDAs cover three different polarization angles. The deepest part of the antennas is buried about 1.5 meter below the ice surface. Due to the ray-bending in the ice, most signals from neutrino induced showers will not reach the surface and will therefore not be seen by the surface antennas. The surface component will mainly function as cosmic-ray detector and with that also as muon-veto, as explained in chapter 3.

4.2.2 Deep Component

The deep component of an RNO-G station consists of three strings reaching from the surface to ≈100 meter depth. One of them functions as the *power string* and contains the phased array trigger at the lower end of the string. Two additional Hpols are added right above the phased array. Because the Hpols are close to the phased array Vpols, they all see roughly the same electric-field and therefore the cluster can be used for electric-field reconstruction by deconvolving the antenna response, as is explained in chapter 3. Three more Vpols are placed at this string, at roughly 80, 60 and 40 m depth. The travel time differences between these channel pairs will help with the vertex distance reconstruction. The other two strings are referred to as *helper strings*, and they are mainly for azimuth reconstruction of the radio signal. They contain two Vpols, an Hpol and an additional Vpol that functions as calibration pulser. The horizontal string separation for an RNO-G station is 20 m from the center of the station.

4.2.3 LPDA, Vpol and Hpol

RNO-G makes use of antennas predominantly sensitive to the vertical (Vpol) as well has horizontally (Hpol) polarized signals for the deep component and log periodic dipole antennas (LPDA) for the surface component. The Vpol and Hpol have been specifically designed for RNO-G.

LPDA

The LPDA antennas have the largest gain of the antennas used in an RNO-G station. They are very sensitive, directional and broadband antennas. They are large in measures (roughly

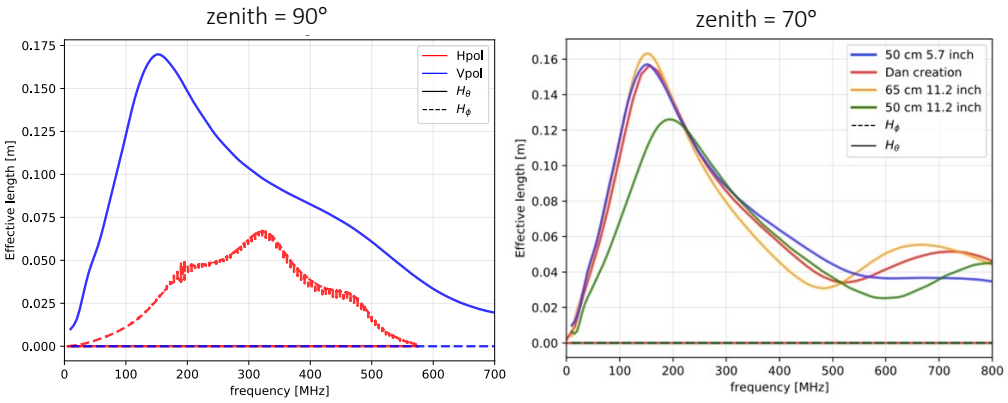

Figure 4.5: Left: Vector effective length for the RNO-G Vpol and Hpol. The bicone Vpol is broadband and has a maximum sensitivity around 150 MHz. The Vpol is hardly sensitive in the ϕ direction (horizontal). The slot-antenna Hpol is sensitive in the 200-450 MHz band and peaks around 280 MHz. The Hpol is hardly sensitive in the θ direction (vertical). Right: Vector effective length for various iterations of the RNO-G Vpol for a zenith of 70°.

1.5 x 1.5 m) and therefore ideal for a surface component, where digging trenches of these sizes is doable. They are sensitive in the full frequency range of the amplifiers and have a clear peak frequency just below 100 MHz. The LPDAs are commercially produced by CREATE, located in Japan [114]. The same LPDA antennas are used as for ARIANNA.

Hpol

The narrow holes limit the possible geometries of the antennas for the deep component that can be used. The horizontal size of the antenna is limited to the 11.2 inch width of the borehole, favoring the usage of vertically oriented antennas. Therefore a slot-antenna design is chosen for the Hpol. Slot-antennas couple to the magnetic field, instead of to the electric field and therefore the horizontal component can be detected while the antenna is vertically oriented. This approach was also used for ARA [78]. Hpol simulations were performed in air and the antenna response was rescaled for the in-ice refractive index. More work is ongoing for in-ice simulations of the antenna response. The frequency depenedent conversion factor between the electric field and the antenna voltage is given by the *vector effective length* H_{eff} as will be further explained in section 5.2. The vector effective length for a zenith of 90° is shown in figure 4.5. The H_θ component of the Hpol is nearly zero. The band represents an asymmetry in azimuth. The Hpol is mainly sensitive from 200-400 MHz.

Vpol

The RNO-G Vpol is a bicone antenna, iterating on the GNO and RICE design, which makes it sensitive to vertically polarized electric fields [115]. Vpol simulations were performed based on xFDTD [116]. Simulations were performed in ice with a constant index of refraction of 1.78. The vector effective length for a zenith of 90° is shown in figure 4.5. The H_ϕ component of Vpol is nearly zero. The antenna has a peak frequency at $\pm$ 150 MHz and is sensitive between 100 and 600 MHz. To chose the Vpol with the most optimal geometry, simulations were performed to study the effect on both effective volume and reconstruction performance, as will be discussed in section 4.5.2. The Vpols are also used as the calibration pulsers as part of the deep station.

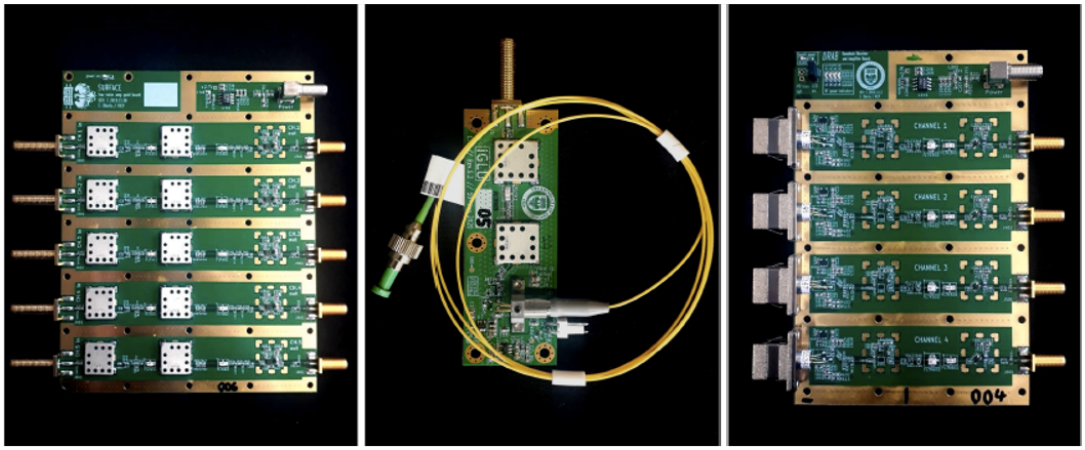

Figure 4.6: Amplifiers as designed for RNO-G. Left: SURFACE amplifiers for the signals coming from the LPDAs via coaxial cable. Middle: an IGLU board (In-ice Gain with Low-power Unit) used to convert signals from antennas deep in the ice to analog RF signals and then feed them into the indicated fiber. Right: DRAB board (Down-hole Receiver and Amplifier Board) located within the station housing. Figure from [17].

4.2.4 Trigger, Power and Amplifiers

To obtain the high effective volume needed to be sensitive in the ultra-high energy regime, is equipped with a low-threshold trigger and the amplifiers are designed to have low system noise temperature. Each RNO-G station is powered by two installed solar panels, which has the nice benefit that the stations are easily scalable.

Phased Array Trigger

The main trigger for RNO-G is a phased array trigger which uses the coherent-sum and beam-forming from a compact array of four Vpols positioned at the lower end of the power string. The phased array trigger is already successfully used in ARA, although design changes had to be made in order to accommodate for lower available power due to the autonomous station design of RNO-G [78]. Eight beams will be formed, which is a lower number than for ARA, but the beams will be wider, such that they cover the full range of expected signal arrival directions. The phased array will be placed at roughly 100 m depth, which is below the firn (70 m) such that it provides significant increase in field-of-view due to fewer limitations by ray bending. The phased array is expected to behave similar as a 2-σ dipole trigger [17, Fig. 18].

Power and Communication

The stations are designed to function autonomously with wireless communication. A commercially sourced LTE base station is deployed with an antenna on the roof of the MSF (Mobile Science Facility) building at Summit Camp with a band of 880-915 MHz uplink and 925-960 MHz downlink. An additional LoRaWAN network is deployed which provides a backup low-power, but low-bandwidth connection for control and monitoring.

Each station is powered by two solar panels, with a maximum power output of 300 W, and a lead-acid battery bank of 5kWh. The solar panels are located at the center of each station.

Figure 4.7: Left: Helper string hole of station Amaroq made with the BigRAID drill, the first completed station-hole of RNO-G. Right: BigRAID drill with erected tower and lowered drill. The drill is attached to TUCKER (owned by Summit Camp) to move the drill to the next station after hole completion.

The battery bank is sufficient for a three day full system operation when no power of the solar panels is available due to e.g. cloudy days. The panels are pointed south, in order to catch most sun in the shoulder seasons (when the sun only rises above the horizon for short periods per day). The RNO-G stations can be operated in several different modes, depending on the available solar power capacity. When the station is fully running (*full-station* mode), the power usage is 24 W. In *high-threshold* mode, the low-threshold phased array trigger is turned off, the LTE-data transfer is minimal, which results in a power usage of 17 W. When even less power is available, the entire deep station is turned off and only the 9 surface LPDAs are running (*surface-only*) which uses 6 W. During the polar night, the stations will be set in *winter-over* mode, which means that everything is turned off except for the LoRaWAN network and the station controller.

In total, RNO-G has a science livetime of roughly 70% averaged over the year. For the remaining 30%, the station is in *winter-over* mode. In the deployment season of 2022, 3 wind-turbines will be installed to forsee the station of power when the solar panels cannot provide for it, which is expected to increase the science life time to more then 90%.

Amplifiers and DAQ

For the deep station, the feed of each deployed antenna is connected via a coax cable and a low-noise amplifier (IGLU). The signal is transmitted by Radio Frequency over Fiber (RFoF) to prevent significant gain losses due to long copper coax cables. The RFoF as well as the IGLU are powered by a DC connection from the surface, which is the only through-going coax cable in the boreholes. The IGLU and RFoF are designed for minimal noise temperature and low power. The signals are converted back to analog signals in the DAQ box (DRAB), where they are amplified. The LPDA signals are transmitted by coax cables and amplified in the DAQ box with the SURFACE amplifier. The amplifiers are shown in figure 4.6.

Figure 4.8: Left: In-field deployment of the first RNO-G station (Amaroq). Two solar panels are installed at the center of the station, pointing towards the south. All the hole positions and LPDA positions are marked by red flags. Right: Deployment shack being transported using a snowmobile.

4.3 Summit Camp and Deployment

RNO-G is located near the United States National Science Foundation (NSF) facility Summit Camp (also Summit Station) in Greenland [117]. Summer 2021 was the first deployment season of RNO-G in which three stations were deployed and calibration measurements were performed.

4.3.1 Summit Camp Greenland

The ice sheet on which Summit Camp is located is more than 3 km thick, which provides the homogeneous and cold ice needed for radio neutrino detectors. Due to the NSF facility, Summit Camp contains the required infrastructure to allow for the installation and maintenance of the detector. Summit Station is part of the Northeast Greenland National Park, which is 3.200 m above sea level. Summit is 460 km away from the closest village and is only accessible by plane via Kangerlussuaq. There is a 4.5 km long and 60 m wide ski-way which is regularly maintained and makes plane traffic possible during days with good visibility. The ski way is shown in the schematic figure 4.1, together with the fully planned RNO-G experiment. Also shown in the figure is the Big House, which is the main communal building of the camp and functions as galley. South of the Big House is the clean air/snow sector; here is the location of the weather observatory (Temporary Atmospheric Watch Observatory) and where snow samples are taken for geological ice studies. Therefore, the locations of the RNO-G station sites are north of Summit Camp.

During the winter season, $\approx$ 5 people are stationed at Summit Camp to keep the station going. During the summer, Summit can host up to $\approx$ 40 people, of which only a small fraction ($\approx$ 8 people) as part of science teams. The first deployment of the RNO-G experiment started in summer 2021, which was one year later than originally planned due to the COVID pandemic. The first installation was performed by a science team of 7 people and two shifts of 3 people operating the drill. Furthermore, three weeks were used for ice and calibration measurements after the deployment period. Summit Camp provides snow mobiles which are used for transport to the station sites during the deployment and sleds to transport the cargo and the deployment shack. Deploying a full single station, including the communication set-up and solar panels, takes roughly 3-4 days, provided that there is good visibility and that there are no days with the wind coming from the north. Since the weather station

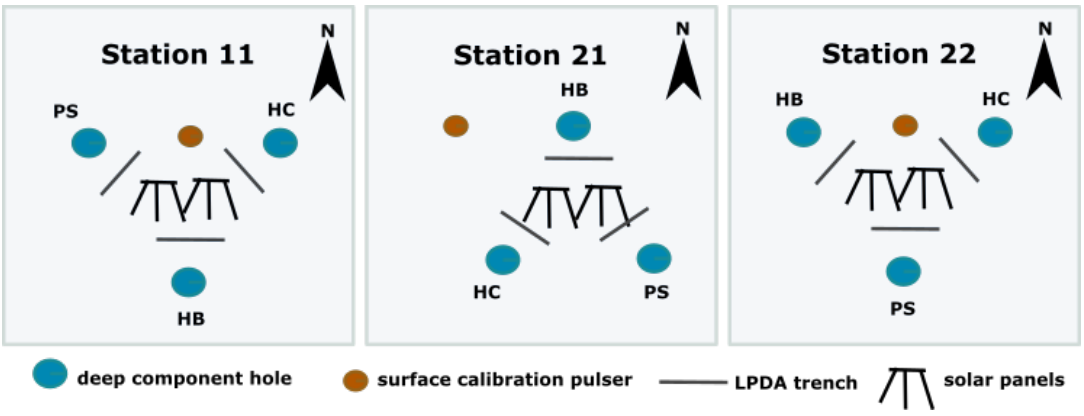

Figure 4.9: The station configurations of the three deployed stations Nanoq (11), Amaroq (21) and Avinngaq (22). Indicated are the power string (PS) and helper string holes (HB and HC) for the deep component, the LPDA trenches, the solar panels and the position of the calibration surface pulser.

is south of the RNO-G station sites, no fuel can be burned when the wind is coming from the north, which means that snow mobiles and the drill cannot be used.

4.3.2 BigRAID

For the 100 m deep holes for the deep component of an RNO-G station, the BigRAID drill (Big Rapid Ice Drill) from the British Antarctic Survey was used. The obtained holes have a large diameter of 11.2 inch (32 cm), which allows for some flexibility in the antenna designs. The drill is mechanical, instead of the hot-water drill used for IceCube. A mechanical drill is much more light-weight, uses less power and is less complex, which makes it preferable for large scale projects. The usage of BigRAID in the first deployment season of RNO-G has been the first in-field operation of the drill. A total of 10 holes were made to depths between 95 and 100 meters, of which 9 are the holes of the three deployed RNO-G stations, and one functions as an outfall hole for Summit Camp. Some trouble shooting during this first in-field usage of the drill was because of parts of the drill that broke and had to be repaired, unexpected performance in the changing weather at Summit and not be able to operate the drill due to low visibility or northern winds. The drilling team has shown to be able to drill a 100 meter hole in a single (long) shift. Another reason the BigRAID drill was chosen is because of the fast performance, such that drilling the holes would not be the limiting factor during deployment. The drill with erected tower and lowered drill is shown in figure 4.7, together with the first finished hole (helper string) at Amaroq.

4.3.3 Station Deployment

The LPDAs from the surface component are placed in 1.5 meter deep trenches. Each trench is about 6 meters long and 2 shovel blades (60 cm) wide and is positioned orthogonal between a deep string bore hole and the centre, 7 meters away from the centre. A level is used to make sure that the antennas are standing correctly positioned. After placing the antennas, the trenches are refilled with snow. An extra small trench from the middle of the LPDA trench towards to center of the station is made, which guides all the coax cables from the LPDAs to leave the trench. Some of the cables are extended with 0.89 m long jumper cables when the coax was not long enough to reach the DAQ box, which will be fixed for further

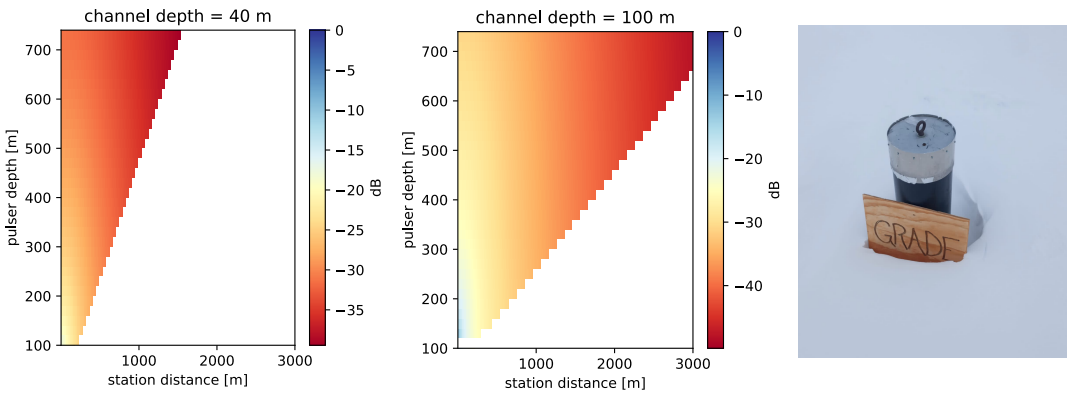

Figure 4.10: Left: Decrease in amplitude due to the attenuation of a pulser in the DISC hole for various antennas within an RNO-G station and located at various positions. Right: The top of the DISC hole. Seen is the black casing and the metal lid on top.

seasons.

For the string-deployment of RNO-G a deployment shack is used, learning from the experience of ARA. A photo is shown in figure 4.8 right. The shack is insulating and ideal for the precise work of attaching modules and connecting cables for the deployment team to perform the lowering of the strings. A hole is located in the floor of the shack, which allows the string to be dropped down the hole, provided that the shack is nicely aligned with the borehole. The modules are attached to a rope with butterfly knots and carabiners. Coax cables and fibers are connected to the antennas and taped onto the rope. The 100 meter string is attached to a 4x4 piece of wood which is put horizontally on the hole which is then covered with wood and marked with a red flag.

The fibers from the deep antennas and the cables from the deep as well as surface antennas are trenched towards the center of the station and connected to the DAQ box, which is located together with the other electronics in a big black weather-proof box. This is also seen in figure 4.8.

The preferred position for the power string is south. This way the calibration pulsers at the helper string are opposite from the power string with respect to the DISC hole (see 4.4) which will function as a hole for calibration measurements. In practice, some of the hole positions changed due to the in-field circumstances. The deployed configurations for the three stations are shown in figure 4.9. Also, the surface calibration pulser for station 21 got placed at a different position, because a spare hole of 6 meters deep was available. Station 22 is deployed as initially designed.

4.4 DISC hole, Calibration Pulsers and Ice Density Measurements

A good understanding of the behaviour of the ice is needed for station calibration and neutrino identification. Every station is equipped with two calibration pulsers which will pro-

vide information on local ice-measurements and antenna performance. Furthermore, a 740 meter deep hole (DISC hole) is located near Summit Camp, which can provide the basis for more global ice-measurements.

4.4.1 Deep Ice Sheet Coring Hole

A few hundred meters from the Big House, a hole with a diameter of 122 mm is located, drilled by Ice Coring and Drilling Services in contract of the National Science Foundation. It is referred to as the Deep Ice Sheet Coring (DISC) hole [118]. Because of the nearby position to the RNO-G stations, as can be seen in figure 4.1, it is ideal for ice measurements. The DISC hole is filled with liquid to make sure the hole does not close, and the top tens of meters are covered with a casing as shown in figure 4.10 right. The last usage of the DISC hole was in 2004 for density measurements of the Greenland ice [111]. In the deployment season of 2021, the DISC hole was retrieved by removing the snow-accumulation of 20 feet. Unfortunately, the hole turned out to be closed at a depth of 99 m. Therefore, no ice measurements using the DISC hole were performed in this year and proper equipment needs to be brought during the next deployment season in order to open up the hole and potentially make it usable again.

Detecting pulses with the antennas from the RNO-G stations from a pulser in the DISC hole can be used for ice measurements. Due to the ray bending, the pulser needs to be deep in the ice in order receive signal in the antennas of the RNO-G stations to overcome that the pulser is in the shadow zone from the receiving antenna, like explained in section 3.6. Furthermore, the signal strength will decrease depending on the distance of the station and suitable pulsers need to be chosen accordingly. Figure 4.10 shows the decrease due to the attenuation for various pulser depths and station distances for antennas at 40 and 100 m depth, the minimum and maximum antenna position depth for an RNO-G station. The decrease is calculated using

$$\text{decrease in dB} = 10 \cdot \log_{10} \frac{a}{l},$$

where a is the factor by which the frequency spectrum is multiplied due to the ice attenuation along the traveled path for which an attenuation model based on data of [106] is used. l is the path length traveled by the radio signal. Due to the changing index of refraction, rays will bend in the ice, resulting in a region in the ice where the signal cannot reach. Therefore, as seen in figure 4.10, the pulser as well as the receiving antennas needs to be deep enough. With a strong enough pulser the closest three stations would be able to detect a signal in the deepest antenna.

4.4.2 Calibration Pulser

Every helper string of the deep stations contains a Vpol pulser, which can be used for calibration purposes, e.g. to verify the antenna responses, the antenna positions and local ice measurements. Also, the pulser data was used to identify that the antenna number mapping as deployed in the field was different than planned. Figure 4.11 left shows the pulses from the pulser at station 11. This data corresponds to the calibration pulser at helper string C, which results in a high amplitude and distorted pulse at antennas on the same string (bottom right, Helper C). The antennas on the power string, detect a signal that reduces in

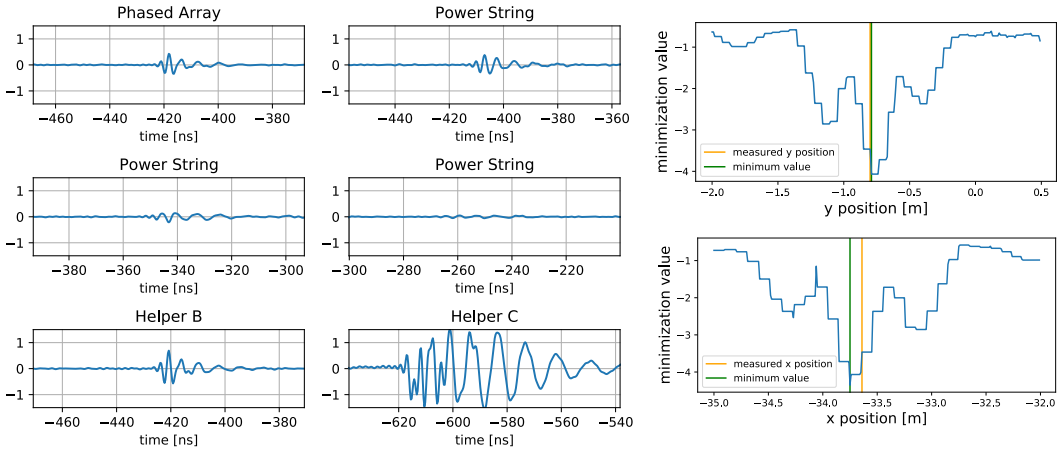

Figure 4.11: Left: Calibration pulser data in station 11. Right: Reconstruction of the calibration pulser position by fitting a spherical wave.

amplitude for higher up antennas. As a first cross check for the antenna positions, the waveform of the deep antenna of the power string (phased array) as well as helper string B were used to reconstruct the position of the calibration pulser. These waveforms are expected to behave very similar and therefore no correction for the antenna response is required. For this, the module `sphericalWaveFitter` is implemented in NuRadioMC (simulation software for radio neutrino detectors, as will be discussed in chapter 5) which fits a spherical wave to the timing differences of the pulses to obtain the pulser position x, y, z. For the antenna positions, the positions that were measured in the field were fixed and the pre-measured cable-delays were used. The result for a single event is shown in figure 4.11 right, and as can be seen, the x, y pulser position can be determined to within a few cm of the measured in-field position.

4.4.3 Ice Density Measurements

As an attempt to verify the density of the ice, ice chips from several depths along the hole were collected. The visual structure of these ice chips varies greatly over depth, getting more transparent and dense near the 100 meters depth, as shown in figure 4.12 right. The density of the various ice chips was determined by measuring the volume per chip: by putting it in Canola oil in a measuring cylinder, and measuring the mass difference of the cylinder with and without chips. The results are shown in figure 4.12 left. Although matching the density as expected, the error bars with this technique are too large to see any depth dependence.

The BigRAID is a mechanical drill that with each iteration removes a core with ice from the hole, and then brings the core back up to remove the ice from it. Because all the ice is preserved and the volume of the core is fixed, this could in further seasons be used for depth dependent ice density measurements by measuring the mass of each core.

4.5 Antenna and Station Design Optimization

In order to maximize the effective volume of RNO-G, stations are deployed on a sparse grid of 1.25 km between stations such that a large ice volume will be covered by the array. Therefore, most events will only trigger a single station. String and antenna spacing are optimized

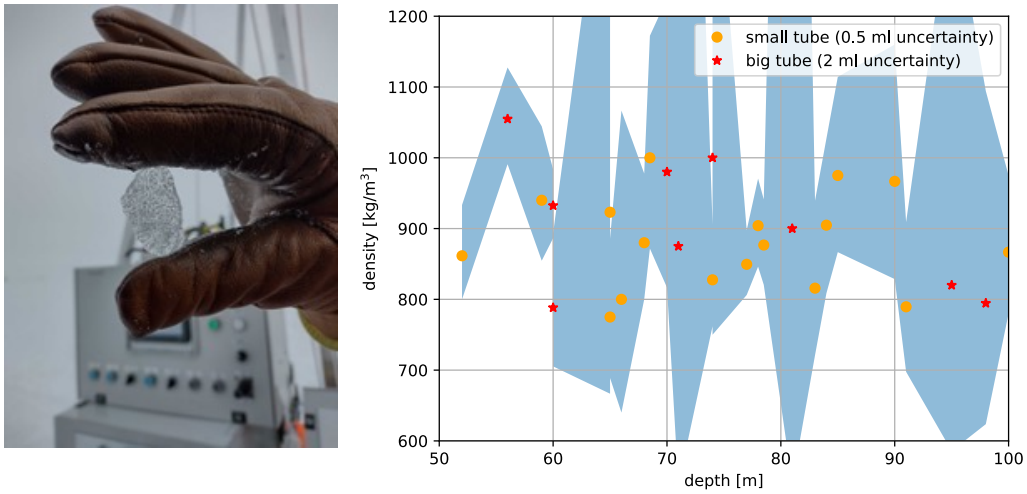

Figure 4.12: Right: Ice chip at 100 meter depth obtained by the BigRAID drill. Enclosed air bubbles are clearly visible. Left: Ice density measurements as function of depth, derived from volume measurements of ice chips using a big (red) and a small (orange) cylinder. In blue the uncertainties due to reading errors from the cylinders are given.

such that a single station can be used for reconstruction of the neutrino properties.

4.5.1 String and Antenna Spacing

In order to reconstruct the azimuth direction of a radio signal, three horizontally spaced measuring points are needed. The helper strings function as the additional two strings to reconstruct incoming direction of the signal, with antennas at 100 m depth to obtain the highest efficiency, since the trigger is also at 100 m depth. The efficiency drops quickly for antennas towards the surface, due to the ray bending in the ice. The larger the spacing of the string, the larger the deviation in electric field seen by the different antennas, since the difference in viewing angle is larger (as explained section 3.4), which helps the pointing-resolution of the neutrino direction. The signal amplitude drops quickly for angles further away from the Cherenkov angle. Therefore, spacing the strings too far reduces the change of observing a signal in both strings.

Figure 4.13 left shows the fraction of events that have an amplitude larger than a specific signal-to-noise (SNR) for different string spacings. The figure shows the fraction compared to a distance of 20 meters. Shown is the amplitude for the lowest amplitude antenna, since signal in each of the strings is required for a signal arrival direction. For increasing spacing a smaller fraction of events will have a large amplitude, i.e. losing almost 10% for 40 meter spacing compared to 20 meter spacing for an SNR of 3. For RNO-G, a string spacing of 20 meters from the center of the station is chosen which corresponds to a string distance of 34 meters to each other.

4.5.2 Antenna Design

The deep trigger consists of four Vpols, and therefore the effective volume completely depends on the performance of the Vpols. The effective volume is maximized when the peak

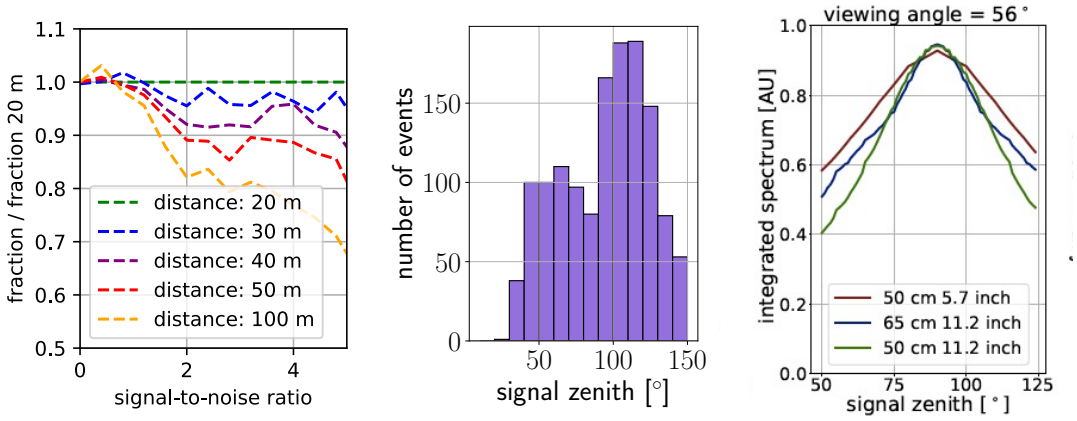

Figure 4.13: Left: Effect of the horizontal distance between the strings on the received signal in antennas at 100 meter depth. The two helper strings are horizontally displaced over larger distances while the triggering string (single dipole trigger 2σ) is fixed. Shown is the fraction compared to a station with 20 meter separation, for the minimum amplitude in the helper strings. Middle: Distribution of the zenith direction of the signal received at the antenna. Right: Example plot for the comparison of the relative frequency content for 80-600 MHz for antenna types of various various lengths and in a narrow (5.7 inch) and wider (11.2 inch) borehole.

frequency of the Vpol vector effective length has its maximum around the maximum of the frequency spectrum for the most frequent viewing angle. Figure 4.14 shows the effect on the effective volume for one of the final iterations in the Vpol design. Antennas of length 50 and 65 cm in bore holes of 11.2 and 5.7 inch are compared. This study was performed due to the possibity to make wider boreholes (11.2 inch) compared to previously planned (5.7 inch) and to varify the impact of the Vpol antenna choice regarding this change. Noiseless single antenna 100-240 MHz simulations were performed for the *Alvarez2009* model (see chapter 5). The ratio shown in the trigger is compared to the effective volume of a 50 cm Vpol in a 11.2 inch borehole for a 1.5σ trigger, which is a threshold thrigger of 1.5 times the root mean square of the thermal noise. Shown is an increasing effective volume for the same Vpol in a narrower borehole of 5.7 inch. Because a broader borehole benefits and simplifies the design of the Hpol, a broader borehole is preferred. Therefore, also the 65 cm Vpol was simulated in the 11.2 inch borehole which results in very similar performance as the smaller Vpol (50 cm) in the narrower borehole (5.75 inch).

To study the effect of different Vpol geometries on the reconstruction the impact on the power in the frequency band for the various kind of antennas was studied. Most triggering neutrinos for RNO-G are from the 75° zenith band. The radio signal arrival direction peaks around 70° and 110° (figure 4.13 middle) which is 20° off from the horizontal where the antenna is the most sensitive. For this distribution an RNO-G event set is used, using the flux described in 7.1.1. The performance of the antenna off-boresight (figure 4.5 right) is therefore important. An example result for studying the impact on the power off the frequency spectrum for the same antenna types as for the effective volume study in figure 4.14 is shown in 4.13 right. The 65 cm Vpol, with antenna response as shown in figure 4.5 is the design chosen for RNO-G.

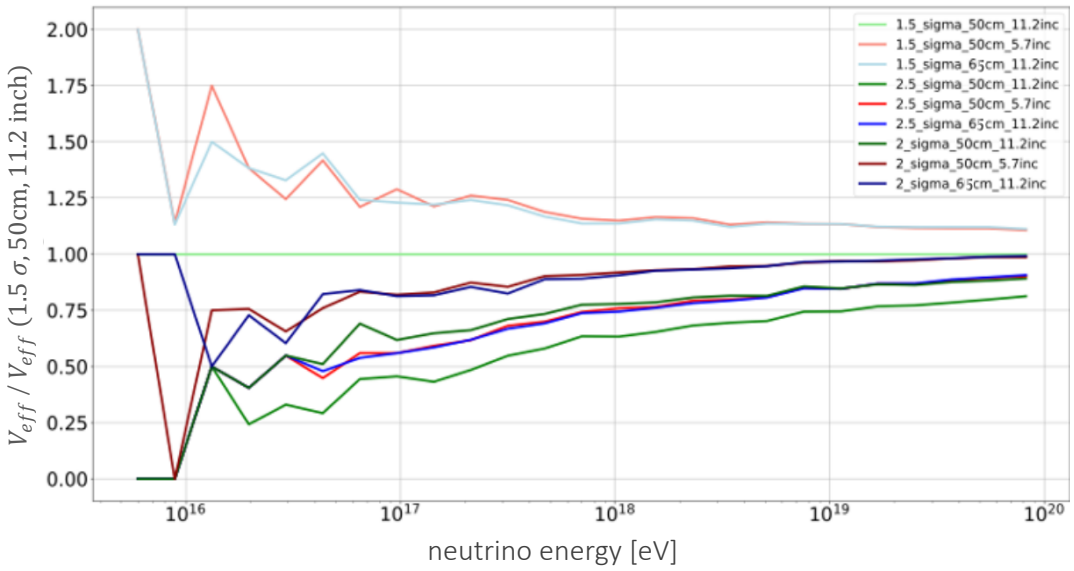

Figure 4.14: Effect of different simulated Vpol antenna responses on the effective volume of RNO-G. Used is a the single bicone trigger for σ_{noise} of 1.5, 2, and 2.5 as a phased array proxy. A bicone antenna of 50 cm in a borehole of 11.2 inch and a borehole 5.7 inch is used in the simulation, as well as a 65 cm antenna in the broad borehole. The effective volume is given compared to the 50 cm antenna in the broad borehole.

Chapter 5

Simulation and Reconstruction Framework

iglu.

— *Greenlandic for* building of any kind

For the work in this thesis the radio neutrino software NuRadioMC is used [119; 120]. The python-based package includes several pillars for full neutrino events and detector simulations: *event generation*, *signal generation*, *signal propagation* and the *detector simulation*. NuRadioMC is set up such that each pillar can be easily exchanged by an improved or different module. Part of NuRadioMC is NuRadioReco, which is the framework for reconstructions and includes the detector simulation. Section 5.1 will describe the simulation chain of NuRadioMC and addresses the four pillars, with the main focus on the variety of signal models (signal generation) and the signal propagation as it is of importance for this work. Furthermore, in section 5.2, the main modules in NuRadioReco used are briefly described and the implementation of the new reconstruction modules within this framework are detailed. Then, section 5.3 describes the ray tracing code RadioPropa, since it is implemented as an exchange module for the signal generation pillar.

5.1 NuRadioMC

NuRadioMC contains the pillars event generation, signal generation and signal propagation. Each pillar will be outlined in the temporal order of the physical processes.

5.1.1 Event Generation

The event generator specifies all neutrino properties and creates a list with neutrino interaction vertices. The event generation specifies the following parameters:

- the *vertex position*, i. e. the position of the interaction of the neutrino. The vertex position is randomly placed in a cylinder with specified volume.
- the *neutrino flavor*. The flavors and the corresponding ratios can be specified.
- the *neutrino energy*. The energy is drawn from a specified energy spectrum between a minimum and maximum energy.
- the *neutrino direction*. The neutrino direction can be specified between minimum and maximum zenith and azimuth directions.
- the *interaction type*, i.e. whether the neutrino undergoes a neutral current (NC) or charged current (CC) interaction.
- the *inelasticity*, i.e. the fraction of the neutrino energy going into the hadronic part of the interaction.

The lists with parameters are stored in an HDF5 file. In order to also track secondary losses of all types of leptons, the particle decay code PROPOSAL is included in NuRadioMC [121].

The neutrino events are generated uniformly in vertex positions, zenith and energy, or according to a by the user defined energy spectrum. However, this does not include the probability of this event reaching the detector volume. In order to account for this, several weighting functions are implemented in NuRadioMC. The one used in this work includes the density of the earth and the traveled path through the earth to the interaction vertex as described by the Preliminary Reference Earth Model (PREM) [122].

5.1.2 Signal Generation

Several Askaryan modules are implemented in NuRadioMC, from which most of them are frequency domain parametrizations as well as an semi-analytical calculation. The signal models depend on the viewing angle Θ_{view} of the signal and the energy E_{sh} of the shower. The signal is calculated in one dimension, and is later on in the simulation composed in three polarization components, dependent on the geometry of the system.

The *Alvarez2009* parametrization as well as the semi-analytic *ARZ2020* will be discussed in more detail, because these are the models worked with in this thesis.

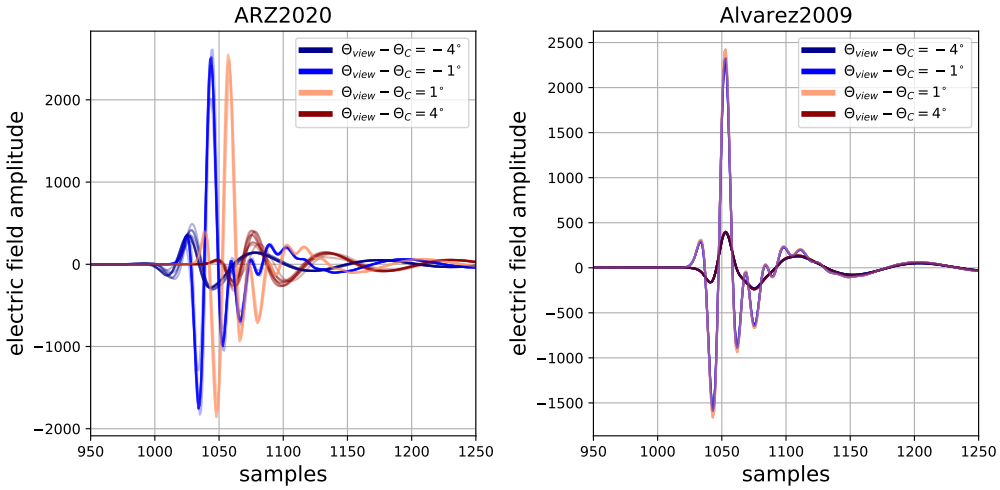

Figure 5.1: Electric field of a hadronic shower in the time domain for a neutrino with a shower energy of 10^{18} eV and with a viewing angle of 1° and 4° on both sides of the Cherenkov angle for the ARZ2020 model (left) and the Alvarez2009 model (right). For ARZ2020, electric fields for ten showers per viewing angle are shown, which results in small variations.

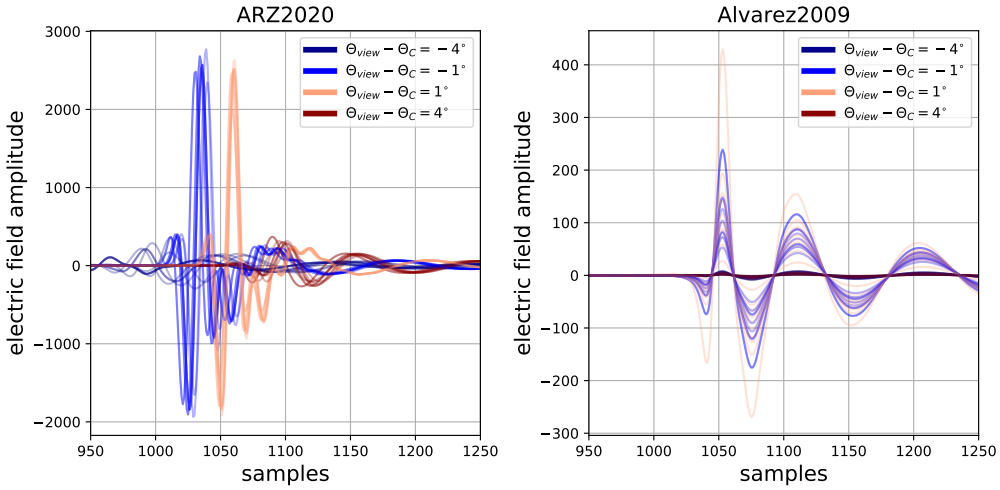

Figure 5.2: Electric field of an electromagnetic shower in the time domain for a neutrino with shower energy of 10^{18} eV and for a viewing angle of 1° and 4° on both sides of the Cherenkov angle for the ARZ2020 model (left) and the Alvarez2009 model (right). For ARZ2020, electric fields for all ten showers per viewing angle are shown, which results in small variations.

5.1.2.1 Alvarez2009

NuRadioMC includes two signal parametrizations: *Alvarez2000* and *Alvarez2009* [123; 124]. *Alvarez2000* is included in NuRadioMC for comparisons with previous works and other codes, but it overestimates the Askaryan amplitudes by roughly 20-30%. The improved *Alvarez2009* is used in this thesis and is in good agreement with the more precise ARZ time domain calculation, which will be described in section 5.1.2.2.
The *Alvarez2009* module, as implemented in NuRadioMC, depends on the viewing angle $\theta_{X_{\max}}$ which is the angle between the radio emission as coming from the shower maximum and the shower axis. The parametrization is a product of this viewing angle, a scaling function that grows linearly with the primary energy, frequency and two functions that are cutoff factors that account for deviations from linearity due to incoherence effects associated to the longitudinal and lateral extensions of the shower. A shortcoming of such parametrizations is that no phase information is provided which leads to inaccuracies in the time domain. The phases are approximated being a constant function of frequency,. While this may be a reasonable approximation for many cases, it does not capture the details of the shape of the pulses and does not account for physical time delays. This results in a very symmetric behaviour around the Cherenkov angle, as can be seen in the time domain electric-field traces in figure 5.1 right.

Alvarez2009 provides parametrizations for hadronic and electromagnetic showers separately. The Landau–Pomeranchuk–Migdal (LPM) effect in the electromagnetic showers is taken into account by stretching of a smooth shower profile. This is shown in figure 5.2 right. This does not take into account the stochastic nature of the process and the fact that first few particles of an electromagnetic shower are impacted differently by the LPM effect as the energy is not equally distributed.

5.1.2.2 ARZ2020

With the *ARZ2020* model, the Askaryan radiation is calculated from detailed charge-excess profiles in the time domain. NuRadioMC contains a shower library per shower energy of 10 showers, where the simulation of the particle shower in ice is simulated with ZHAires [68]. The simulation of the first neutrino nucleon interaction is simulated with HERWIG [125]. Showers are available for shower energies up to $10^{20.5}$ eV in steps of $\Delta \log_{10}(E) = 0.1$ and energies that are not explicitly simulated, the shower amplitude with the nearest energy is rescaled by a factor $\frac{E_{\text{event}}}{E_{\text{library}}}$.

Showers are available for electromagnetic as well as hadronic showers. In general, hadronic showers exhibit little shower-to-shower fluctuations. Figure 5.1 left shows time domain electric-field traces for all available charge-excess profiles for a small variety of viewing angles for hadronic showers. Seen are the small shower-to-shower fluctuations. Furthermore, seen is the slightly different shape for two showers at opposite sides of the Cherenkov angle, which is caused by frequencies arriving in different times due to a proper accounted for phase modelling in the simulations.
Electromagnetic showers undergo the LPM effect which results in large shower-to-shower fluctuations on a single event basis, which can be nicely described, since the model is based on a realistic shower library, instead of describing the average behaviour. The model captures subtle features of the cascades like sub-showers and accounts for stochastic fluctua-

tions in the shower development which can alter the Askaryan signal amplitudes significantly [126]. Electromagnetic showers are shown in figure 5.2 left for a shower energy of 10^{18} eV.

The computation time for the *ARZ2020* model is large (factor 10 with respect to parametrizations), as it involves computationally expensive convolutions of the Askaryan vector-potential with Monte-Carlo generated cascade profiles. The agreement between the electric field predicted by the ZHaires Monte Carlo and the one obtained with the ARZ model is only a few percent of, up to 2 GHz.

Future optimizations for more precise shower models could contain a full Monte Carlo simulation where each shower particle is tracked and the radio emission is calculated from the acceleration and creation of each charged particle, like done by CoREAS and ZHaires for air-shower experiments [67; 68]. Whereas usage of new models is user friendly within the current NuRadioMC framework, this level of precision is no urgency for radio neutrino detectors, due to the experimental uncertainties and the high computational costs.

5.1.3 Signal Propagation

The signal propagation pillar of NuRadioMC handles the propagation of the Askaryan signal through the medium to the observer positions. Assuming that the radio waves propagate as individual rays, the different ray paths connecting the vertex position and an antenna can be classified as *direct*, if the depth is monotonously decreasing along the path between emitter and receiver, as *refracted*, if the path shows a turning point, and as *reflected*, if the ray is reflected off the ice-air interface at the surface.

Two methods have been implemented in NuRadioMC to perform the raytracing. An analytic raytracing approach, where the path is found by solving an analytical function and a numerical raytracing approach. The latter uses the raytracing software RadioPropa, which find the propagation path numerically [127].

5.1.3.1 Analytic Raytracing

The analytic raytracing approach uses the assumption that the refractive index of the ice can be described as an depth-dependent exponential function n(z), given by:

$$n(z) = n_{\text{ice}} - \Delta e^{\frac{z}{z_0}} \tag{5.1}$$

where z is the depth and n_{ice}, Δ_{n} and z_0 are the model parameters which are n_{ice} = 1.78, Δ_{n} = 0.51 and z_0 = 37.25 for the Greenland ice, which is equation 5.1 fitted to the data of [111]. For the specific exponential model of equation 5.1, an analytic solution of the raypaths exist for a given start (neutrino vertex) and end (antenna) point.

5.1.3.2 Numerical Raytracing

For any smooth density profile beyond the single exponential function of equation 5.1 a numerical raytracer is needed in order find the allowed raypaths between emitter and ob-

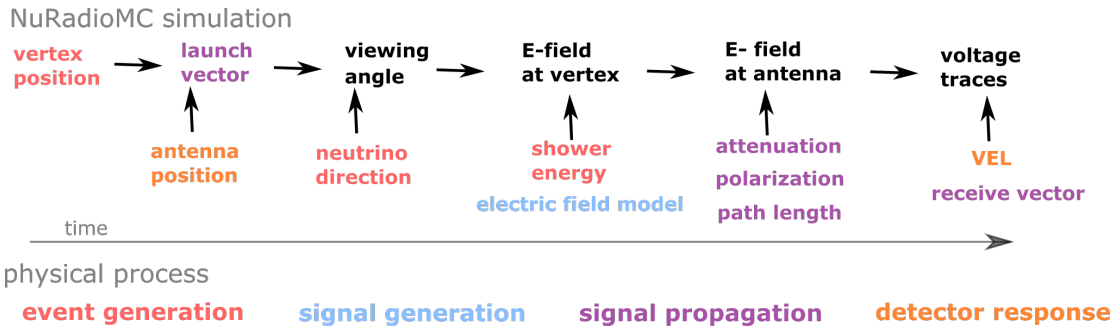

Figure 5.3: Schematic of the NuRadioMC simulation chain.

server. For this numerical raytracer, the software package RadioPropa is included in NuRadioMC. A more detailed description of the software RadioPropa and the implementation in NuRadioMC is given in section 5.3. The approach used is that several rays from the vertex position are launched and tracked during their propagation until the ray reaches the defined observer position. Obviously, this method is more time-consuming than the analytic raytracing approach. An advantage of this method is that any density model can be included, which does not have to be exponential or azimuthal symmetric. Furthermore, the RadioPropa package allows for the implementation of other behaviours beyond the standard propagation, like *horizontal propagation*. The impact of the usage of RadioPropa is described in chapter 7.

5.1.4 NuRadioMC Simulation Chain

Once the propagation path is established, several quantities are derived in order to use for the simulation:

- The *launch vector* $\vec{l}$ and *receive vector* $\vec{r}$, which are the angles between the horizontal and the start of the ray path, and the horizontal and the end of the ray path respectively. The launch vector is needed in order to calculate the viewing angle. The receive vector is needed to evaluate the antenna response for the arrival direction of the incident radiation.
- The *viewing angle* Θ_{view}, which is the angle between the shower axis s and the launch vector $\vec{l}$.
- The *polarization* $\vec{p}$, which is determined using $\vec{l} \times (\vec{s} \times \vec{l})$. The polarization vector is used to obtain the three components of the electric field. An additional polarization correction is applied to the electric field for *reflected* rays, using Fresnel's equations.
- The *path length* R is needed in order to correct the electric field for the $\frac{1}{R}$ attenuation of the radio signal due to the propagation.
- The *ice attenuation*. The electric field is corrected for the attenuation of the signal due to the propagation in the ice, using a frequency and depth dependent attenuation. An polynomial function is fitted to the data of [128] for the attenuation model (*GL1*).
- The *focussing factor*. Due to the raybending, for rays with no surface reflection and if the receiver is above the source, convergence is expected resulting in an amplification of the signal.

In a full neutrino simulation, the sequence in which the above mentioned pillars are used is not linearly. First the raytracing is performed for the generated event, to derive the quanti-

ties used for the signal generation: the signal models all depend on the shower energy and the viewing angle. This is schematically illustrated in figure 5.3. Then, the obtained electric field is corrected for the ice attenuation, for which the signal propagation pillar is again required. Furthermore, the obtained electric-field is corrected for the polarization and for the travel attenuation. Using the *receiving vector*, the antenna response for the incoming radio signal can be calculated to convert the electric field in voltage using NuRadioReco, as will be discussed in section 5.2.

5.1.5 Connecting of the Pillars

In the NuRadioMC simulation software, the signal propagation and signal generation pillar are completely decoupled: the signal propagation is based on pure geometry and performed without any knowledge of the signal. Parameters (Θ_{view} and R) obtained from the raytracing are then used for the calculation of the signal. Especially in an inhomogeneous medium, like a big natural ice volume, where trajectories are refracted in the firn, the decoupling of the propagation and signal generation can lead to noticeable inaccuracies. The most precise method to take this into account is the finite-difference time domain (FDTD) method that calculates Maxwell's equations at each point in time and space [129]. While this is accurate and combines the signal propagation and generation, it also allows for using arbitrary density profiles and gives solutions for the special cases, like shadow zone signals. While FDTD may be useful for cross-checks on a single event bases (like done in [111]), the usage is inpractical for simulations on a full event set bases, due to the high computational cost of simulating a full detector volume on the order of km^3 which could take $O(10^{17})$ CPU-hours.

An in-between step may be the implementation in NuRadioMC of the parabolic equations (PE) method, which approximates the full wave equation, making it possible (at the expense of accuracy) to calculate the electric-field in a point in space only based on the previous point of the propagation, making it less time-consuming than FDTD [130]. Since PE combines the generation and propagation of the signal in order to calculate the electric field directly at the antenna position, it takes the interference of various viewing angles into account.

5.2 NuRadioReco

NuRadioReco is the part of NuRadioMC that takes care of the detector description and for the simulation of the footprint of the neutrino interaction seen in the detector. Furthermore, all the modules for reconstruction are part of NuRadioReco. This section describes the detector simulation and outlines the implementation of the neutrino reconstruction modules that are written for this work.

5.2.1 Detector Simulation

The detector description consists of the description of the detector layout and of the signal chain of the detector. The detector layout used in this thesis is specified using *json* files, which indicates all the antenna positions, antenna types, cable delays etc. In the near future, the RNO-G database will be directly coupled to NuRadioReco in order to read in the detector description with a MySQL connection, like also done for the AERA experiment. This

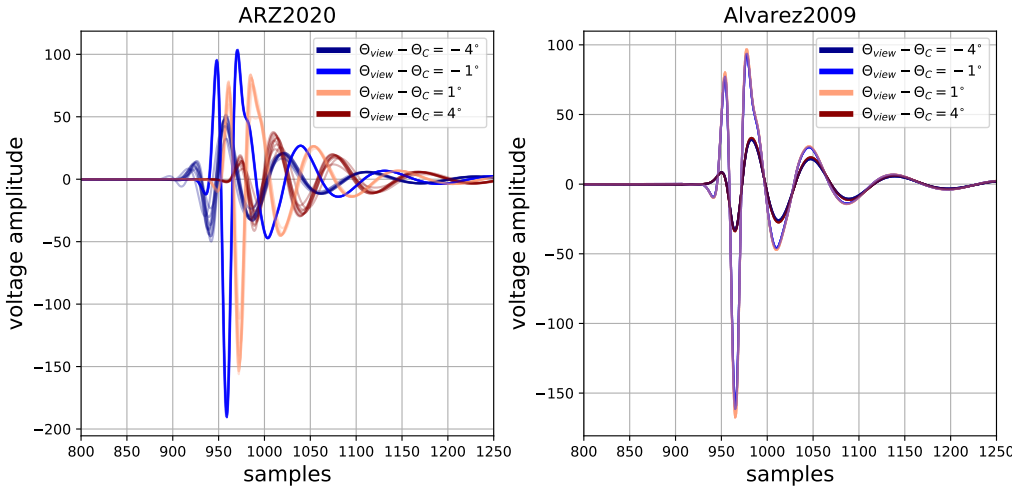

Figure 5.4: Voltage traces of a hadronic shower in the time domain for a neutrino of with a shower energy of 10^{18} eV and with a viewing angle of 1° and 4° on both sides of the Cherenkov angle for the ARZ2020 model (left) and the Alvarez2009 model (right). For ARZ2020, electric fields for ten showers per viewing angle are shown, which results in small variations.

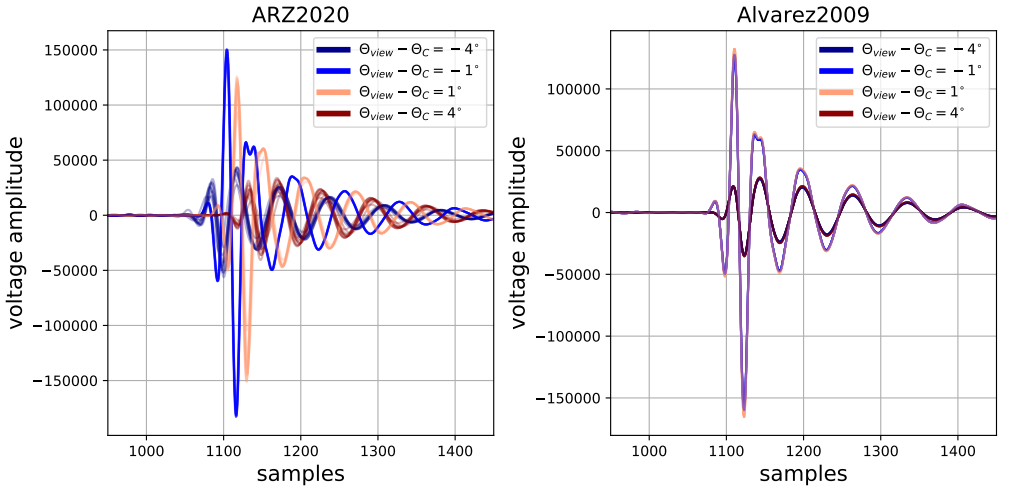

Figure 5.5: Amplified voltage traces of a hadronic shower in the time domain for a neutrino of with shower energy of 10^{18} eV and for a viewing angle of 1° and 4° on both sides of the Cherenkov angle for the ARZ2020 model (left) and the Alvarez2009 model (right). For ARZ2020, electric fields for ten showers per viewing angle are shown, which results in small variations.

enables the access of all components for large scale detectors and for time-dependencies. Other detector specifics, like filters and triggers, are incorporated by NuRadioReco modules.

5.2.1.1 Antenna Patterns

The antenna pattern simulations for the Vpol, Hpol and the LPDA (as discussed in section 4.2.3) are all stored in the same data structure in NuRadioReco as a *pickle* file. The antenna response files are stored at a central server and downloaded automatically when they are called for. NuRadioReco uses the vector effective length as quantification of the antenna response, which is the frequency and incoming signal direction dependent factor $H(\Theta, \phi, f)$ between electric field $E(\Theta, \phi, f)$ and voltage output $V(f)$ of the antenna:

$$V(f) = (H^{\theta}(f), H^{\phi}(f)) \cdot (E^{\theta}(f), E^{\phi}(f))^{T} \tag{5.2}$$

The antenna response for the Vpol and Hpol are shown in figure 4.5. The $H(\Theta, \phi, f)$ values are obtained by using a linear interpolation of the nearest data points in the available file. Dependent on the spacing of the directions and frequencies in the antenna simulations, an extra cubic interpolation is performed, before converting to the NuRadioReco format.

Most antenna simulation software does not output the vector effective length, but moreover the frequency and angle dependent gain of the antenna. $H(\Theta, f)$ can be calculated using

$$|H_{rl}|^2 = \frac{c_0 2}{f^2 4\pi} \frac{50}{\pi Z_0} G_{rl}(\omega) \tag{5.3}$$

with f the frequency, c_0 the speed of light, Z_0 the impedance, n the refractive index of the medium and G_{rl} the realized gain. For simulations performed in air, $H(\Theta, f)$ can be calculated by shifting to lower frequencies according to $f = \frac{f_{\text{air}}}{n}$, with n the refractive index of the medium.

5.2.1.2 Description of Detector Simulation Modules

A number of modules in NuRadioReco enable the detailed simulation of the used detector. The detector simulation modules used in this thesis are:

- The `efieldToVoltageConverter` module calculates the voltage waveform that an electric field produces in the antenna. The module convolves the electric field with the vector effective length retrieved from the detector description.
- The `channelGenericNoiseAdder` module generates the thermal noise of the antennas and adds this to the simulated voltage traces. A variety of noise distributions are available. In this thesis, the mainly used noise distribution is noise that is Rayleigh distributed in amplitude and added in the frequency domain.
- The `triggerSimulator` module simulates the phased array trigger. It simulates eight different beams of incoming directions and adds the waveforms of the phased array, which uses a threshold in the power of the combined waveforms as trigger. This trigger is mainly used in this thesis. Another simulated trigger available in NuRadioReco which is used is the *SimpleThreshold* trigger, which triggers after an by the user defined

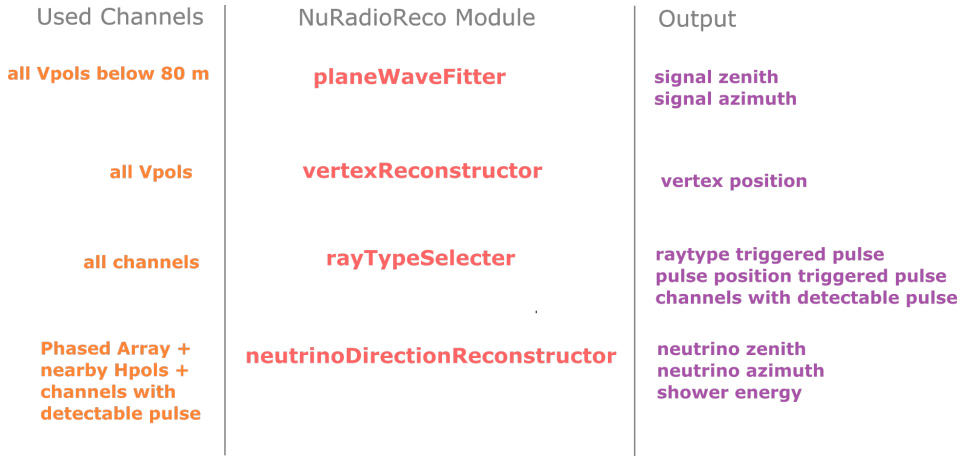

Figure 5.6: Schematic of the modules (middle column) implemented in NuRadioReco to reconstruct the direction of the neutrino. The modules are used in the reconstruction in the order from top to bottom. The left column indicates which antennas of an RNO-G station are used for the specific step, and the obtained property of the module is noted in the right column.

amount of channels reaches an certain amplitude. This trigger is sometimes used as proxy for the phased array (2-σ dipole trigger), and sometimes as pre-simulation to make the event set for the phased array simulations smaller. The raytracing is performed for each channel, which is the most time-consuming part of the simulation, and therefore using a pre-trigger for a single dipole reduces the time of the simulations significantly.

- The `hardwareResponseIncorporator` module includes all the amplifiers and cable delays.
- The `channelBandPassFilter` module includes filters to the signal. Different filter types are available, which can be applied to any frequency band.
- The `channelResampler` module enables the up- and down sampling of the traces.

Figure 5.4 shows voltage traces for the *ARZ2020* and *Alvarez2009* model by convolving the electric field from figure 5.1 with the vector effective length of the Vpol using the `efieldToVoltageConverter`. The traces are amplified with the IGLU amplifier using the `hardwareResponseIncorporator` in figure 5.2. Besides amplifying the signals, the amplifier adds group delay to traces, as can be seen in the figure.

5.2.2 Implementation of Neutrino Reconstruction Modules

The main focus of this thesis is developing an algorithm to reconstruct the arrival direction of the neutrino. Therefore, this section gives some more details on the specifics of the implementation in NuRadioMC/Reco.

There are a couple of modules that are part of the direction reconstruction:

- The `planeWaveFitter` module reconstructs the zenith and azimuth direction of the incoming signal using the lowest channels of the deep detector. It has the option for a brute-force approach or a `scipy` minimizer. For neutrino signals, a voltage template is correlated with the traces in order to find the position of the pulses and to determine

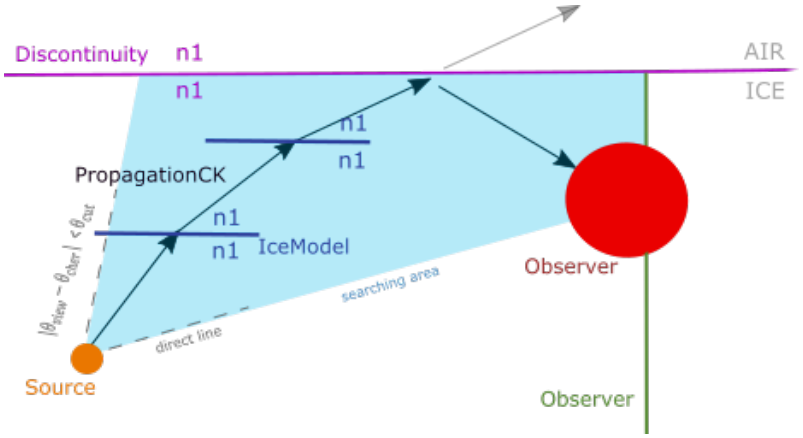

Figure 5.7: Schematic of the RadioPropa raytracer code. The blue shaded area indicates the searching area as implemented in NuRadioMC.

Δt for different channel pairs. Using the module for any other sources (RFI, pulsers) the direction is determined by getting the Δt of channel pairs by correlating the traces itself.

- The `vertexReconstructor` module reconstructs the interaction vertex position of the neutrino. It uses the output direction of the *planeWaveFitter* in order to reduce the possible vertex positions to a 3D cone, which is completely scanned. The correlation of all the channel pairs are maximized due to the travel timings of all ray types for a specific vertex position. The timings can be calculated either using raytracing, or using look-up tables.
- The `rayTypeSelecter` module determines the ray type of the triggered pulse in the phased array. It uses the reconstructed vertex position of `vertexReconstructor` to determine the time differences between channels of the phased array and finds the most likely ray type (direct, refracted or reflected). Also, it stores the pulse position of the triggered pulse in the phased array. Moreover, the `rayTypeSelecter` uses the reconstructed vertex position and the triggered pulse position, to determine all the time-windows of the arriving pulses the antennas of the entire station. Then, it selects the antennas which have a detectable pulse using an amplitude threshold.
- The `neutrinoDirectionReconstructor` module uses the reconstructed vertex from `vertexReconstructor` and the ray type and triggered pulse position of `rayTypeSelecter` to reconstruct the neutrino direction, by fitting a parametrization for the voltage traces to the data. It includes the channels in the fit which are selected by the `rayTypeSelecter`. A brute-force method and a `scipy` minimizer are implemented.

A schematic of the modules part of the neutrino direction reconstruction is shown in figure 5.6.

5.3 RadioPropa

RadioPropa is a numerical raytracing software written in C++ and forked from the cosmic-ray propagation code CRPropa [127; 131]. For this work, RadioPropa is implemented in NuRadioMC in order to handle more complex icemodels in NuRadioMC than purely simple exponential functions. All the work described in this thesis regarding RadioPropa has

been performed together with Bob Oeyen (UGent). Details will be published in his forthcoming thesis.

RadioPropa uses geometric optics to calculate the propagation of the radio waves, assuming that they propagate as individual rays. For each small propagated path ds, the bending of the ray is calculated due to the change in refractive index, as is illustrated in figure 5.7, together with the usage of several modules in RadioPropa. The implemented modules in RadioPropa which are of use for the implementation within NuRadioMC are: `Source`, `PropagationCK`, `IceModel`, `Observer`, and `Discontinuity`.

- The `Source` is the starting point (neutrino interaction vertex) of the ray tracing and specifies the location, amplitude and direction of the signal.
- `PropagationCK` handles the propagation of a radio ray by calculating every distance step the bending of the path due to the change in refractive index. The propagation is determined by solving a simplified version of the eikonal equation, in which is assumed that in every change of refractive index along the path the change in path ds is small. The Cash-Karp solver implemented in CRPropa is used to solve this [132].
- The `IceModel` module gives for every point in space the refractive index.
- The `Observer` is a surface with a specified position and shape, which denotes the end of the ray tracing once the surface is reached. They function mainly as the antennas, but could also be used to stop the raytracing by placing observers at the borders of the searching area. The `Observer` used as the antenna is a sphere with radius R and the `Observers` used as end-points are planes indicated by a normal vector.
- `Discontinuity` is a surface that describes a non-continuous change in refractive index and calculates the reflection and transmission coefficient according to Fresnel's law and changes the amplitudes of the rays accordingly. The module creates a secondary ray for the reflected part of the ray, which is also propagated further. The `Discontinuity` module is for example used at the ice-air boundary.

Finding the correct raytracing solutions with RadioPropa as part of the NuRadioMC is done by scanning a range of launch directions. By using geometric restrictions, the time needed to find the correct solution is limited. Furthermore, since the antenna `Observer` needs to be a finitesimal point in order to be reached and small enough to get good accuracy which increases the computing time due to the required smaller $\Delta\phi$, an iterative method is implemented in which the sphere size of the antenna `Observer` reduces. The measures taken for the implementation to reduce computing time are:

1. RadioPropa can handle icemodels defined at any position x, y, z in space. However, since currently only 2D data models are available, there will be no ray bending in the x, y-plane. Therefore, the raytracing is performed in 2D by restricting the ray to a vertical plane in which $\Phi = \Phi_{\text{antenna}}$.
2. Because the refractive index increases with depth, the rays will always be refracted downwards, as long as there are no reflective layers. Therefore, rays shot at a zenith Θ below the antenna's zenith Θ_{antenna} will never reach the antenna. Therefore this region is excluded.
3. The raytracer scans the residual search region in successive steps where each step limits the search region further for the next iteration. In each step the angular stepsize reduces and the radius R of the `Observer` antenna reduces until the necessary accuracy is reached. This is nicely visualized in figure 2 of [133].

4. The viewing angle is used to make a cut on the search region, since the amplitude decreases rapidly for off-cone events, and therefore these events will not result in any detected signal, although a raytracing solution might exist.

The entire path of the RadioPropa is saved and from that the receive and launch vector, as well as the propagated length, are calculated, which are needed for the NuRadioMC simulations. Furthermore, the effect of the depth dependent ice attenuation on the pulse is calculated using the full propagated path.

The current status of using RadioPropa as raytracer for neutrino simulations in NuRadioMC takes about 50 times as long as the analytic raytracer. However, other searching algorithmes are possible for future improvements, like a minimization, which can further reduce the timing.

In order to verify the solution of the RadioPropa raytracer, the numerical raytracing is compared with the analytic raytracing. For this comparison the *greeland simple* model implemented in NuRadioMC is used as ice model, which is the smooth exponential model fitted to the density data of [111]. The parameters that are compared are the viewing angle, arrival time, signal arrival direction and the polarization and the distributions of the spread are given in figure 3 from [133]. The arrival time is accurate within a nanosecond and the viewing angle is precise within 0.02°. The zenith distributions of the arrival direction of the signal, although having very high accuracy, has a small shift towards higher zeniths angles for RadioPropa. These, aleady very small, deviations can be furthermore reduced by adding another iterative step to the raytracer which a smaller final sphere size R, which is the main caus of the deviations. This however, of course, comes at the cost of an even longer runtime.

Chapter 6

Neutrino Direction Reconstruction

Suminngaaneerpit?

— *Greenlandic for* Where are you from?

This chapter outlines the methodology for obtaining the neutrino arrival direction for detected events with an RNO-G station. The implementation is within the software framework NuRadioMC, as is described in chapter 5. The methodology described here is a model based method, referred to as the *forward-folding* approach. The reconstruction procedure will be discussed (section 6.2 and 6.3) as well as the resulting performance for an RNO-G station (section 6.4). Next, in section 6.5, possible improvements for the outlined reconstruction procedure are given. The chapter ends with the implications of the ice for the reconstruction of the neutrino proeprties (section 6.6). First, section 6.1 gives an overview of the current reconstruction methods for in-ice neutrino detectors and their performance as well as an application of the forward-folding method to cosmic-ray data from ARIANNA.

6.1 Forward-Folding Reconstruction Method

While the radio neutrino community is working hard to build vast detectors to detect for the first time the radio emission stemming from a neutrino interacting in the ice, reconstructions need to be developed in order to quantify the characteristics of this neutrino once it is there. This section gives a brief overview of the current reconstructions that are developed, of which some have been extensively used and tested on cosmic rays. Likewise, the forward-folding approach, which is the main work of this thesis, will be applied to cosmic rays as a proof of concept. Next, an introduction is given to the geometry and requirements for neutrino direction reconstruction as well as to the application of the forward-folding for in-ice radio signatures of neutrinos.

6.1.1 Neutrino Reconstruction Methods

To infer the neutrino properties, the waveforms detected in the antennas need to be translated to the neutrino arrival direction and energy. The Askaryan effect has been confirmed and is well understood, but no neutrino has yet been detected with the radio technique, and therefore electric-field predictions rely completely on simulations [69]. As explained in 3.7, the neutrino direction can be established with a measure of the radio signal direction, the viewing angle and the polarization. Timing differences of arriving pulses are used to obtain an estimate for the signal direction. The electric field can be extracted from the voltage waveforms, for which the viewing angle can be determined from the spectrum and the polarization from the amplitude difference in orthogonal antennas. Alternatively, assumptions about the electric-field can be made and compared to the waveforms, such that neutrino properties like shower energy and direction can be obtained directly. Methods have been development for either translating the voltage waveforms to the electric-field, to obtain the neutrino properties, or using the voltage data directly.

The method used for inferring the signal direction for in-ice radio detectors is by estimating the timing differences of arriving pulses at spatially seperated antennas using *cross correlation* of the waveforms. This method will be discussed in more detail in 6.2, since it is the approach used for the signal direction reconstruction in the method outlined in this chapter. ARA as well as ARIANNA make use of the data of an fat-dipole pulser lowered to 1700 meters depth in the South Pole ice (SPICEcore) to estimate their signal direction resolution, resulting in subdegree resolution for both experiments [134; 112; 135].

Information about the viewing angle and the polarization of a neutrino event, can be obtained from the spectrum and the amplitude of the electric field. One approach to obtain the electric field from the waveforms is by deconvolving the voltage data with the antenna response, using

$$\begin{pmatrix} V_1(f) \\ V_2(f) \\ \dots \\ V_n(f) \end{pmatrix} = \begin{pmatrix} H_1^\theta(f) & H_1^\phi(f) \\ H_2^\theta(f) & H_2^\phi(f) \\ \dots & \dots \\ H_n^\theta(f) & H_n^\phi(f) \end{pmatrix} \begin{pmatrix} E^\theta(f) \\ E^\phi(f) \end{pmatrix} \tag{6.1}$$

in which $V(f)$ is the frequency dependent voltage, $E(f)$ the frequency dependent electric

field and $H_i^{\theta,\phi}$ the frequency and incoming signal direction dependent antenna response of antenna i to the ϕ and θ component of the electric field. Due to the noise contribution on the measured waveforms, there is no perfect solution for the electric field, hence the electric field can be determined by minimizing the resulting voltage with V in the frequency domain. This method has been frequently used for cosmic-ray analysis and has shown to work reliably, as long as the used antennas are close enough such that they record the same electric field, and as long as the waveforms have a large SNR. For frequencies or arrival directions where the system is not very sensitive, no physics signal should be measured besides the thermal noise contribution. Due to this low voltage contribution, the expected signal stemming from a real physical process is highly overestimated. In other words, a small signal is divided by an even smaller sensitivity, vastly overestimating the original signal.

The method of unfolding with the antenna response, is currently used by ARA [136] and result in a polarization resolution of 6° for SPICEcore data [137]. Since neutrinos have not yet been observed using the in-ice radio technique, a benefit from the unfolding method (equation 6.1) is that it is completely model independent to obtain the electric field. However, most neutrino events will be expected to be around the trigger threshold, meaning that they will have a very low SNR, making the method described above less favorable.

As the standard unfolding approach does not give reliable results for signals with low SNR, a forward-folding method was developed for the reconstruction of cosmic-rays in [120]. With this method, an analystic model of the electric-field pulse is used. Electric-field pulses of Askaryan emission are assumed to be viewing angle and energy dependent, and therefore comparing the expected voltage traces to a variety of electric fields can give an estimate ont he neutrino properties. Application of this method to cosmic-ray data to infer the polarization is described in section 6.1.2 and results in a resolution for the polarization of 1.3° [83]. The method was applied to cosmic-rays detected by ARIANNA to obtain an estimate on the air-shower energy in [138]. The rest of this chapter shows the usage of the forward-folding method applied to neutrinos for the RNO-G deep station. A similar approach has been applied to the surface station of ARIANNA in [139], resulting in a polariation estimation of $\approx 3°$ for a simulation study for a full ARIANNA expected event set.

Another model independent electric-field reconstruction was developed using *Information Field Theory* which uses Bayesian inference to calculate the most likely radio signal, given the recorded data [140]. Since it also uses the approach of comparing the time-domain voltages, this method is applicable to low SNR events. A simulation study showed that for high SNR events this method results in a polarization resolution of 5°. However, since it is model independent, it requires that the used antennas are close-by such that they measure the same electric field, similar to the approach of unfolding with the antennas response, and unlike the forward-folding method.

Finally, diverse work is ongoing for the reconstruction of neutrino properties using machine learning techniques which have shown promosing results [141; 142].

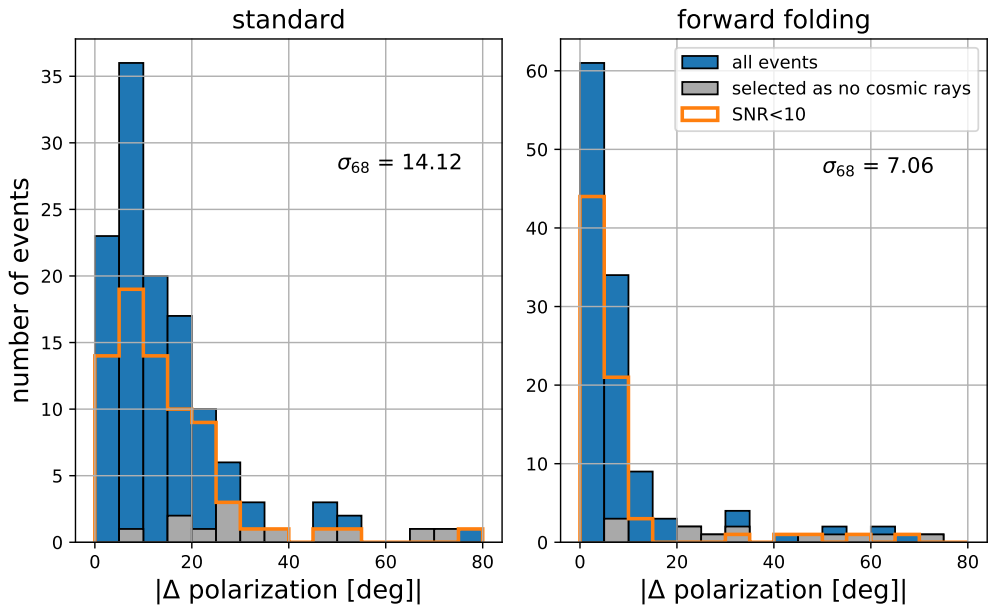

Figure 6.1: Polarization reconstruction as obtained from cosmic rays measured with ARIANNA by deconvolving with the antenna response (standard) (left) and using the forward-folding technique (right). After the event selection, a number of events were identified as background based on their waveform, by visual expection. These are shown in grey and cause most, however not all, of the outliers. These events are excluded for the calculation of the 68% quantile. The reconstructed polarization value is compared to polarization expected due to the geomagnetic emission mechanism.

6.1.2 Forward-Folding: Applied to Cosmic Rays

For cosmic-ray data, unfolding with the antenna response has shown to give unreliable results for low SNR events. Therefore, a forward-folding approach, in wich an analytic discription of the electric field dependent on the frequency f is used, has been established in [120]. As a description of the electric field, an exponential function is used:

$$\begin{pmatrix} E_\Theta \\ E_\phi \end{pmatrix} = \begin{pmatrix} A_\Theta \\ A_\phi \end{pmatrix} 10^{f \cdot m_f} \exp(\Delta j) \tag{6.2}$$

The parameters that describe the electric field are the amplitude components $A_{\theta,\phi}$, the frequency slope m_f and the phase offset Δj. The best fitted values of A_Θ, A_ϕ and m_f are found using an iterative approach [120]. The polarization of the cosmic-ray event can be established using the reconstructed electric fields, using

$$p = \arctan\left(\frac{\sqrt{E_\phi}}{\sqrt{E_\theta}}\right) \tag{6.3}$$

in which E_ϕ and E_θ are the energy fluences in θ and ϕ component respectively.

The main radio emission process for air showers is the geomagnetic effect, and therefore an estimate of the polarization of the electric field can be obtained using only the cosmic-ray direction, with:

$$\vec{p}_{\text{exp}} = \vec{v} \times \vec{B} \tag{6.4}$$

in which $\vec{v}$ is the air shower arrival direction and $\vec{B}$ is the local magnetic field vector. Because

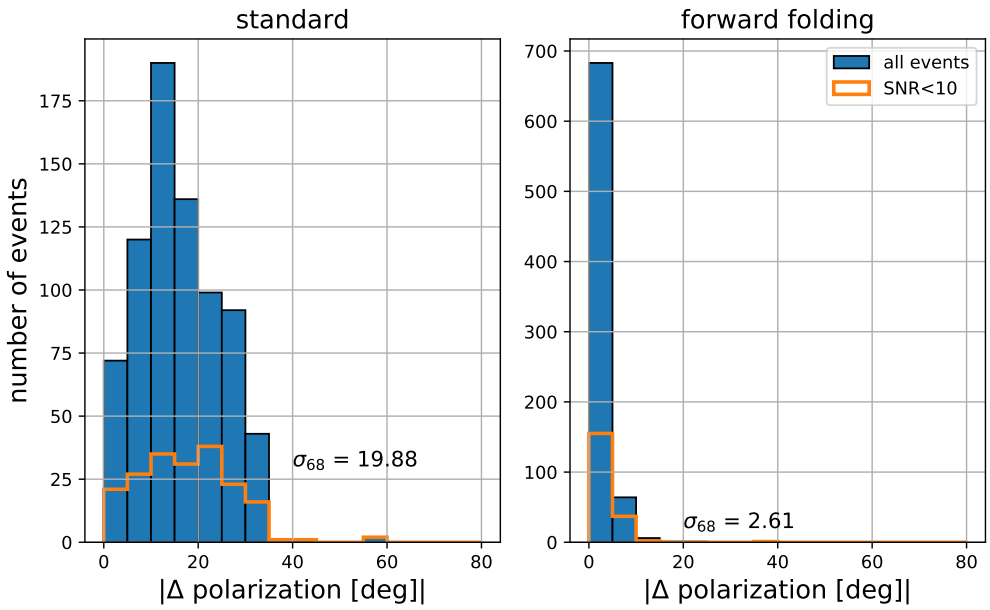

Figure 6.2: Polarization reconstruction as obtained from a simulation study using CoREAS cosmic-ray simulations with deconvolving with the antenna response (standard) (left) and using the forward-folding technique (right).

the Cherenkov angle in air is $\approx 1°$, the arrival direction of the cosmic ray can be estimated by the direction of the radio signal. The polarization calculation from the reconstruction can be compared with this expected polarization due to the Earth magnetic field and therefore the reconstruction method can be verified. The subdominant contribution to the radio emission due to the Askaryan effect, depends on the strength of the geomagnetic effect, which depends on the angle between $\vec{v}$ and $\vec{B}$. For this study, ARIANNA data (Ross-Ice Shelf) is used, where the magnetic field is almost vertical. This means that the contribution of the geomagnetic effect is dominated by the zenith direction Θ . Since the strength increases with air density, the influence of the Askaryan emission is minimized for large Θ, meaning that $\vec{p}_{\text{exp}}$ should give more accurate results for near horizontal events.

To study the performance of this reconstruction method, ARIANNA data is used from the 2017-2018 season for the 4 upward pointing LPDAs from station 32. An ARIANNA station contains two parallel pair LPDAs separated 8 meters from each other. For the cosmic-ray selection, the approach described in [82] is used. For each event, a correlation coefficient χ is defined, which is obtained by correlating the traces with simulated noiseless templates with a variety of energies. The waveforms of thermal fluctuation triggers will result in a low χ value, because their waveforms will not be similar to noiseless simulated templates, and therefore they will efficiently be filtered out. The selection is made on a relation of χ with the maximum amplitude of the event, for which the cut of [82] is used. Furthermore, a cut is made based on the trigger rate, rejecting high-rate periods. Cosmic rays are expected to be distributed randomly in time, whereas man-made signals and other backgrounds tend to cluster in time. After the cosmic-ray selection, an additional cut is perfomed which requires all antennas to have a SNR > 4 to make sure the arrival direction of the cosmic-ray is well established, which is required for a good performance check of the forward-folding technique.

The polarization resolution is shown in figure 6.1 for the forward-folding technique (right)

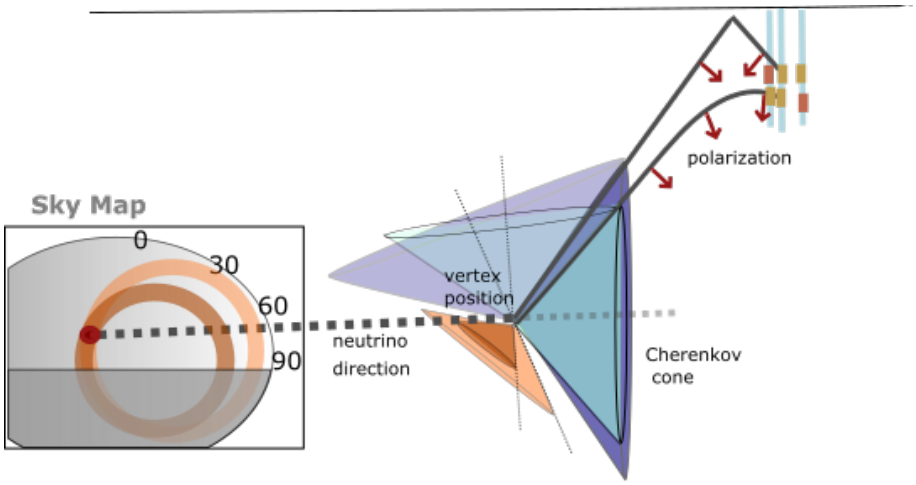

Figure 6.3: Schematic of the resulting emission cone and radio rays due to a neutrino interaction. A direct and a reflected ray are indicated. In orange, the cone that indicates the restricted region for the neutrino direction according to the signal direction and the viewing angle is shown, which limits the direction to a band on the sky (left). In dark en light orange for the direct and reflected ray spectively. In red, the polarization is indicated, for which a measure will restrict the neutrino direction a small ellipsoid.

and for the approach of unfolding with the antenna response (left). The forward-folding technique gives for the full event set a σ_{68} of 7.06°, which is a large improvement compared to the $\sigma_{68} = 14°$ of the standard approach. The polarization resolution can be compared with the obtained values using CoREAS simulations, instead of ARIANNA data. Here, the simulated data set is created with a slightly different detector than the detector used for reconstruction, in order to mimic detector uncertainties. The antennas are moved by 10 cm in random directions and the amplifier is taken to be 10% different. For this simulation set the polarization resolution is σ_{68} = 2.61° using the forward-folding technique, as shown in figure 6.2 right, which is significantly better than the resolution obtained with the standard unfolding approach (left). A follow-up study done by [83] retrieved a polarization resolution of 2.5° for ARIANNA data of season 2018-2019 using the same station 32, which is consistent with the resolution of the simulated data set. Furthermore, [83] obtains a resolution of 1.3° for near horizontal events (zenith larger than 70°), which are consistent with in situ pulsing measurements in [112].

The difference between the polarization resolutions between the 2017-2018 and the 2018-2019 season can most likely be attributed to the snow-accumulation that happened during that year. The LPDAs were deployed very shallow in the ice, and according snow accumulation records the antennas were 1.1 m lower in the ice in 2018-2019. Presumably, in the first season the antennas were too close to the surface of the ice to assume that they were surrounded with infinite snow, which is used in the modelling of the antenna response.

6.1.3 Forward-Folding: Neutrino Direction Reconstruction

Whereas the direction of cosmic-rays can be established by reconstructing the signal arrival direction at the antennas, this does not apply for the detection of in-ice neutrino induced radio emission. The radio signal is strongest on the Cherenkov cone ($\approx 56°$), as is explained

in section 3.4.3 and therefore a reconstruction of the signal arrival direction does not result in an estimate for the direction of the neutrino. Since the emission process in ice is the Askaryan effect (section 3.1.1), the electric field is polarized towards the shower-axis and therefore a measure of the polarization will break the degeneracy and enable to pin-point the neutrino to its origin.

As illustrated in figure 6.3, a measure of the viewing angle will limit the neutrino arrival direction to a band on the sky with a width determined by the resolution of the viewing angle. Even with only a measure of the signal arrival direction, the neutrino direction can be limited to a wide band on the sky with a width of $\approx 10^{\circ}$, since most events will have a viewing angle within a few degrees of the Cherenkov angle. A measure for the viewing angle will narrow this band to a thin band on sky with allowed neutrino directions. A measure for the polarization limits to an ellipsoid on this band.

Due to the depth dependent refractive index in the ice, rays are bent within the ice resulting in various ray types that can reach the detector. When a direct and a reflected ray type will reach an antenna, each of them will have a different viewing angle and therefore each of them will limit the neutrino direction to a different band. The overlap of these bands can limit the area for the neutrino direction, as is shown in the same figure 6.3. Also signals arriving at antennas horizontally and vertically spaced can result in a small variety of viewing angles, already limiting the allowed region for the neutrino direction. This is especially useful, since the Hpols have low sensitivity compared to the Vpols and therefore do they do not always contribute in limiting the construction of the polarization.

A measure for the viewing angle, polarization and the signal arrival direction can be combined to obtain the neutrino direction. The forward-folding method used in this work, however, does not rely on a seperate measurement of each ingredient. While the signal direction is obtained separately, the forward-folding approach fully models the voltage traces as expected by using a description for the electric field, obtaining the direction (Θ ,ϕ) and shower energy E_{sh} directly. We emphasize that this forward-folding approach allows for the usage of antennas which are displaced from each other, since it takes into account the positions of the specific antenna and therefore allows to calculate the expected electric field at its position. Consequently, the vertex position is first reconstructed and used as an input for the forward-folding.

The neutrino direction reconstruction approach outlined in this chapter consists of three steps:

1. The **signal direction** is obtained, which is then used as input to reconstruct
2. the **vertex position**, which is then used as the neutrino interaction point
3. as starting point for the forward-folding approach, to obtain the **neutrino direction**.

6.2 Neutrino Interaction Point

The forward-folding method requires a vertex position as starting point, to estimate the expected viewing angles at each antenna position. First, the signal arrival direction is deter-

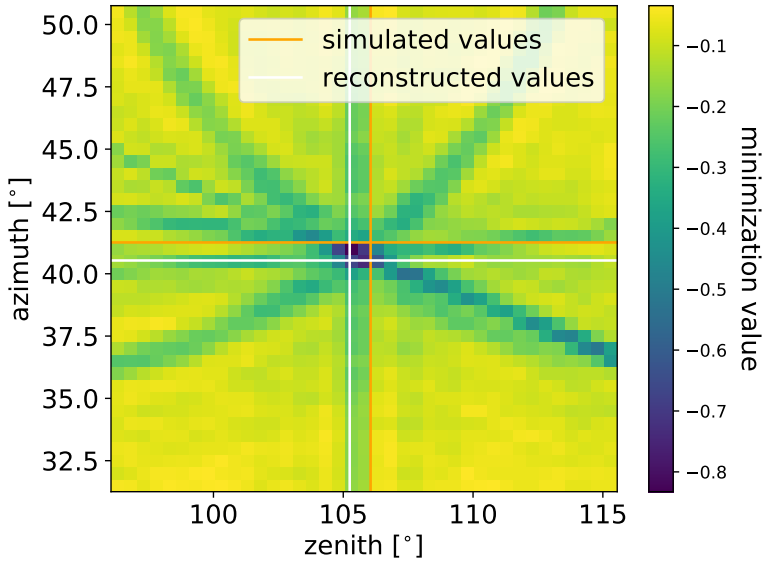

Figure 6.4: Minimization landscape for reconstructing the signal direction using a plane wave approximation. Whereas each antenna pair restricts the direction to a small band in zenith and azimuth, using all anntenna pairs uniquely defines the signal arrival direction.

mined of the ray type of the pulse that triggered the phased array. Since most vertices are far away, the signal direction is determined by assuming the wavefront arrives as a planewave. Then, since the direction of the vertex position is similar to the signal arrival direction, the vertex position can be limited to a narrow cone. The vertex position is reconstructed using this searching area.

The RNO-G event set used for verification of the method outlined in this section is based on the *ARZ2020* emission model and contains an extension of the IceCube flux and a GZK model. The flux model and the quality cuts used are discussed in section 7.1.1 and section 7.1.2.

6.2.1 Signal Direction Reconstruction

The signal direction is determined using the timings of the waveforms at the lowest antennas of an RNO-G station. The timing differences δt of the waveforms at different antennas are calculated and used to find the most likely zenith and azimuth direction assuming a planewave.

6.2.1.1 δt Calculation

To calculate the timing difference for an antenna pair with waveforms i, j they are cross-correlated with a neutrino voltage template t ($\Theta_{\text{view}} = 54°, \phi = 70°$). The cross-correlation of waveform i and template t is defined as

$$c_i[k] = (i \cdot t)(k - N + 1) = \sum_{l=0}^{||i||-1} i_l t^*_{l-k+N-1} \tag{6.5}$$

with N the length of waveforms t and i, and in which k is the sample corresponding to Δt. Then, the most probably time-delay for waveform i and template t is Δt for which $c[k]$ has its maximum value. The time-delay for antenna pair i, j corresponds to k for which the convolution of z_i and z_j (c_{ij}) has its maximum.

To obtain the direction of the signal, multiple antenna pairs are included by combining c_{ij} for each channel. The reconstructed direction is given where C has its maximum, with C:

$$C = \sum_{i=1}^{n} \sum_{j=1 \neq i}^{n} c[\Delta t_{ij}] \tag{6.6}$$

with n the number of antennas used, and with the time-delay t_i for each channel being calculated with a plane-wave approximation using

$$t_i = -\frac{1}{v}(\sin(\theta)\cos(\phi), \sin(\theta)\sin(\phi), \cos(\theta)) \cdot (x_i, y_i, z_i)^T \tag{6.7}$$

with zenith θ, azimuth ϕ, $v = \frac{c}{n}$. Here the refractive index for the antennas at 100 meter is used, i.e. $n = 1.74$. Then the time-delay for antenna pair ij is given by $\Delta t_{ij} = t_i - t_j$.

6.2.1.2 δt Calculation for Non-Neutrino Signals

The advantage of correlating the waveforms with a neutrino voltage template is that the impact of the thermal noise is minimized, such that the pulse position and therefore the timedelay δt_{ij} for antenna pair ij can be very well established. With this approach, waveforms for which the noiseless trace has a signal-to-noise ratio (SNR) > 2.5 are identified correctly. The SNR is defined as the difference between the maximum and the minimum of the signal, devided by two times the σ of the noise distribution. However, this requires a good model for the neutrino voltage waveforms. To identify the direction of other emitters, like pulsers, cosmic rays or RFI sources, the time-delays can be determined by correlating the waveforms i and j directly (equation 6.5 with $t = j$). In order to reduce noise for this method, the pulse for the waveform is selected by taking the maximum amplitude, and the trace is set to zero 50 nanoseconds around this value. Note that this method only works for far-away emitters, due to the plane wave approximations, and only for including the same antenna type since cross-correlation assumes that the waveforms have similar shape.

6.2.1.3 Signal Direction Resolution

The signal direction is calculated by minimizing -C in equation 6.6. The minimization landscape of an example event is shown in figure 6.4. Since multiple ray types can reach the detector, the signal arrival direction is not uniquely defined. A nice benefit of the definition of C is that $c[\Delta t_{ij}]$ is larger for larger amplitude traces and will contribute larger to the minimzation. Adding all the different c components for all the different time-delays will make sure that no intereference of the two ray types take place, and that two individual minimia will be found. One of them is the global minmia, which corresponds to the larges amplitude solution, i.e. the triggered pulse.

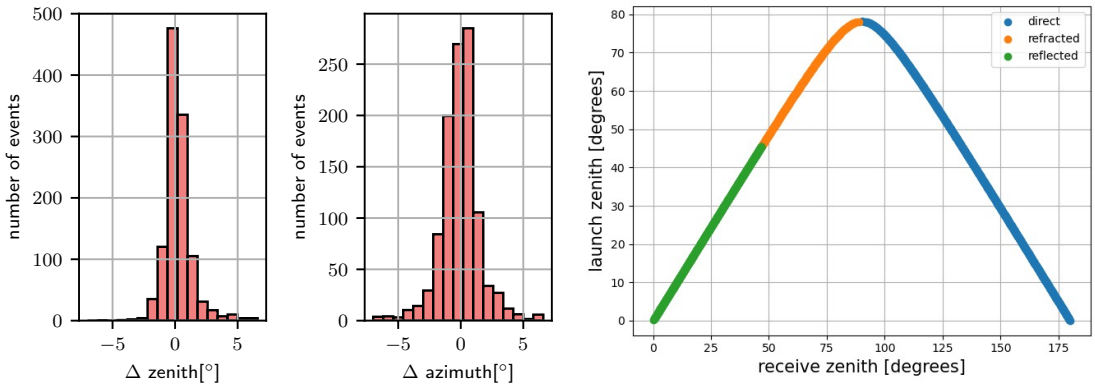

Figure 6.5: Left and middle: Resolution for zenith and azimuth of the signal direction. Right: Relation between the launch zenith and the receive zenith of the signal for an antenna located at -97 m (phased array). Indicated in green, orange and blue are the directions that corresond to refracted, reflected and direct rays.

In order to reconstruct the signal direction, signal in three horizontally spatially displaced antennas is needed in order to obtain an azimuth reconstruction. Furthermore, one vertically spatially separated antenna is needed in order to obtain the direction of the zenith reconstruction. Therefore, a Vpol on each helper string, as well as 2 Vpols from the phased array and the antenna at -80 m are included in the reconstruction. Resolutions for the zenith and azimuth direction are shown in figure 6.5. The reconstructed direction is compared to the simulated arriving direction of the signal arriving in the lower antenna of the phased array of the triggered pulse.

The plane wave approximation especially works very well for events with far away vertices, resulting in a subdegree resolution for this subset. Figure 6.6 shows in the two right plots the fraction of events with a good reconstruction for zenith and azimuth, indicated with the yellow line. As can be seen, 80% of the events can be reconstructed in 1° and 2° for zenith and azimuth respectively. Also the fraction is shown restricted to the events with signal in each helper string, which is a requirement for the azimuth direction of the signal. This increases the fraction by almost 10%.

6.2.2 Vertex Position

The forward-folding technique requires a vertex position as input value. When there is only a single ray type that leaves a noticable signal in the antennas, the distance of the vertex position is not important. Due to the constant index of refraction in the deep ice, a further away vertex corresponds to the same signal arrival direction. However, when multiple ray types reach the detector, the viewing angle of the second ray type depends on distance of the vertex. Therefore, a more exact vertex position is required for the forward-folding approach.

The vertex position can be determined using the timing difference between a direct and reflected ray type in the same channel, because this time-delay increases for vertices further away. This is examined in [143] and especially helpful for shallow detectors, due to their large fraction of events with a direct as well as a reflected signature. This is approach is also used in this vertex reconstruction. To reconstruct the vertex position, a similar approach

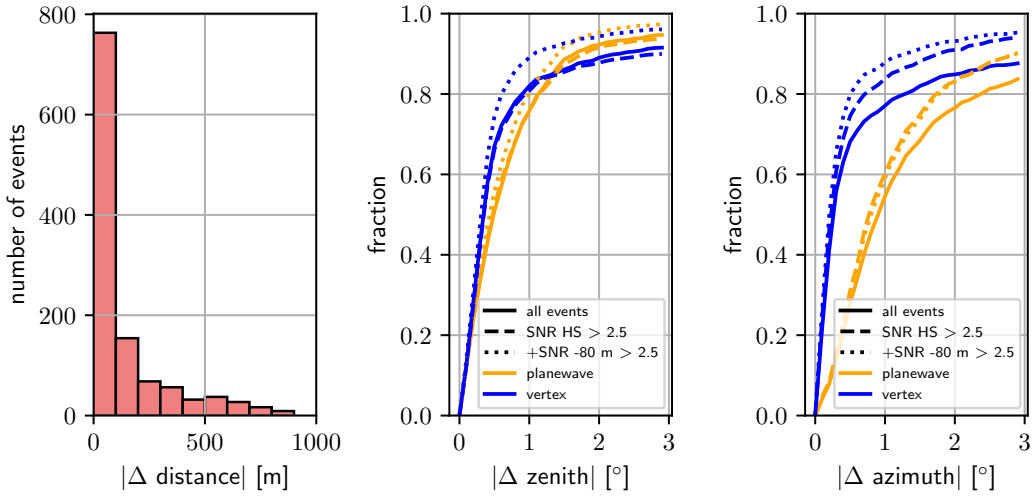

Figure 6.6: Left: Resolution of the vertex distance. Middle: CDF for the resolution of zenith and azimuth (right). Indicated are the results for the signal direction for the planewave approximation (orange) and from the vertex position (blue). Seen is that a vertex reconstruction improves the signal direction with respect to a planewave fit. Results are shown for the full event set (solid), for signal in atleast each string (dashed) and for also signal in the channel at -80 m (dotted).

is used as discussed in the previous section for the signal direction reconstruction. The maximum correlation is determined, this time using time-difference for two antennas due to the full raytracing from a specific vertex position. All the various raypaths are included; direct, refracted and reflected. Especiallly these extra raypaths give a good precision on the vertex position. To find the vertex position, C is maximized, which is not only a sum over the antenna pairs, but also over the various ray types r:

$$C = \sum_{i=1}^{n} \sum_{j=1 \neq i}^{n} \sum_{n=1}^{r} c[\Delta t_{ij}] \tag{6.8}$$

Since the signal arrival direction is known, the position of the vertex can be narrowed down to a small cone. The resolution of the vertex distance is shown in figure 6.6 left. As can be seen in figure 6.6 middle and right, the signal arrival direction due to the vertex reconstruction improves in zenith and azimuth. Restricting to events with signal in each helper string, as required for a good signal direction, results in a slightly worse performance for zenith compared to the performance of the planewave, i.e. some events are not as well reconstructed as with the plane wave approximation. These events correspond to very horizontally arriving signals, and therefore these events do not have signal in any other antenna than the deepest ones, due to the raybending. Adding the requirement of signal in the antenna at -80 m improves the resolution and results in a better resolution than for the plane wave approximation, as expected. These criteria will define the analysis efficiency for RNO-G, as will be discussed in chapter 6.

6.3 Method of Forward-Folding

The forward-folding technique is a model based approach, here used to reconstruct the properties of a detected neutrino. It uses a parameterization for the electric field which is

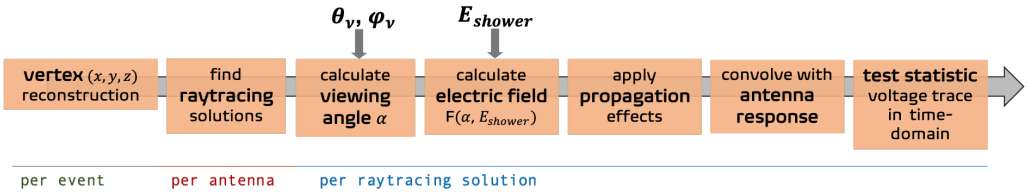

Figure 6.7: Schematic of the neutrino direction reconstruction using the forward-folding approach for neutrinos.

compared directly to the voltages in the time-domain. The input parameters are the neutrino direction (Θ_ν and ϕ_ν) and the shower energy E_{sh}. The reconstructed vertex position is used as input for this reconstruction. For each antenna the raytracing can be performed starting from this vertex position. Because the propagated path of the signal is known, for each possible neutrino direction the viewing angle can be calculated, similar to how the neutrino simulations are performed as outlined in section 5.1.4. This viewing angle together with the shower energy E_{sh} is the input for the electric-field parametrization. The electric field is corrected for the distance R the signal propagated by a $\frac{1}{R}$ correction. Furthermore, the ice-attenuation the signal experiences can be calculated using the propagated path and reduces the amplitude of the electric field as seen at the antenna. Lastly, the electric field is corrected for the polarization. Then, the traces are convolved with the direction dependent antenna-pattern of the specific antenna. This way, the resulting waveforms are exactly mimiked and the most likely neutrino properties can be probed by comparing these expected waveforms with the data. A schematic of this approach is also shown in figure 6.7.

This section describes the details of the method. It discusses a variety of test statistics used and explains the details of the fit, as well as decisions made on applied time-windows and filters, the analytic model used for the electric field and the input parameter space for the minimization.

6.3.1 Test Statistic

The voltage neutrino traces are covered with thermal noise. Thermal noise as produced by the antennas is due to independent fluctuations of the electrons and is therefore mostly Gaussian, as discussed in 3.5.1. This is simulated with a Rayleigh distribution in the frequency domain, like described in section 5.2.1.2. Because of the Gaussian nature of the noise, the test statistic used is the χ^2:

$$\chi^2 = \sum_{V_{\text{H}}=1}^{v_{\text{H}}} \sum_{i=1}^{n_{\text{H}}} \frac{(x_i - f_i(\theta, \phi, E))^2}{\sigma_{\text{H}}^2} + \sum_{V_{\text{V}}=1}^{v_{\text{V}}} \sum_{i=1}^{n_{\text{V}}} \frac{(x_i - f_i(\theta, \phi, E))^2}{\sigma_{\text{V}}^2} \tag{6.9}$$

with x_i the measured voltage at sample i, $f_i(\theta, \phi, E)$ the voltage for sample i for direction θ, ϕ and shower energy E_{sh} according to model f. v_H and v_V are the number of Hpols and Vpols included in the reconstruction respectively, each with number of samples n_H and n_V. σ is the root mean squared of the noise, which is in this work taken as the Monte Carlo true value, taken from the distributions shown in appendix G.

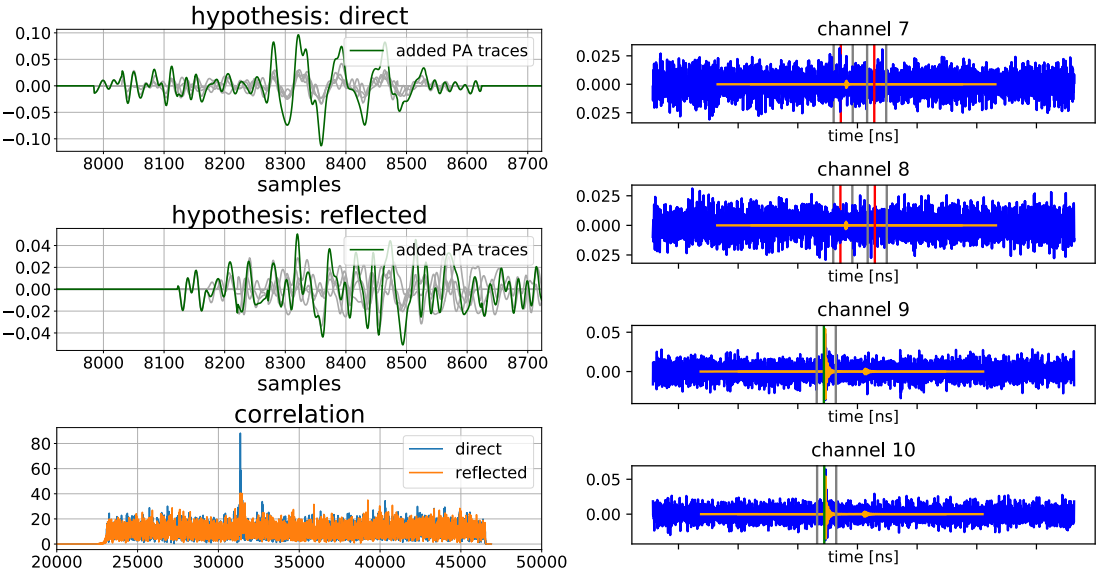

Figure 6.8: Example event for pulse and ray type selection using the four Vpols in the phased array. Left: Determining the ray type of the triggered pulse. Adding the correlations of each antennal correlated with a neutrino template clearly shows a maximum for the direct pulse (bottom figure). The top two figures show the added traces shifted in time due to the two ray type solutions, where the pulses nicely add up coherent for the direct ray. Right: Determining of the pulse windows using the reconstructed vertex position and establishing if a pulse is present in the specific time-window. The data is shown in blue, the simulated trace (noiseless) in orange. The grey lines show the time-window, and the green (red) lines the pulse position. The color green (red) is used if there is (not) a detectable pulse present, with a criteria of SNR > 3.5. If a pulse is present, the antenna is selected to be used for the reconstruction.

6.3.2 Pulse Windows and Ray Type Determination

To compare the voltage templates with data, they need to be alligned in time. To do so, we determine the position and the ray type of the triggered pulse in the phased array, which together provides enough information to fix the global timing and shift the voltage templates accordingly. The pulse position is found correlating each phased array antenna with a neutrino voltage template, very similar to what is explained in 6.2.2. These correlations are shifted in time with the expected timing differences according to the vertex position by performing the raytracing. Adding up these correlations then result in a maximum at the same position for the correct ray type. An example is shown in figure 6.8 left, bottom figure. The correlation with the largest maximum is used as the selection of the ray type and the timing of the maximum correlation is used as the pulse position of the triggered type. The top figures of the same figure show the combined voltage traces due to the timing shifts from the vertex position. Seen is that for the direct ray type all the voltage traces nicely add up coherently.

After the ray type selection of the triggered pulse, the pulse positions of the other pulses reaching the antennas can be determined by raytracing from the vertex position. The time-windows of the pulses are determined and checked if a detectable pulse (by SNR > 3.5) is present in the time-window, as shown in figure 6.8 right.

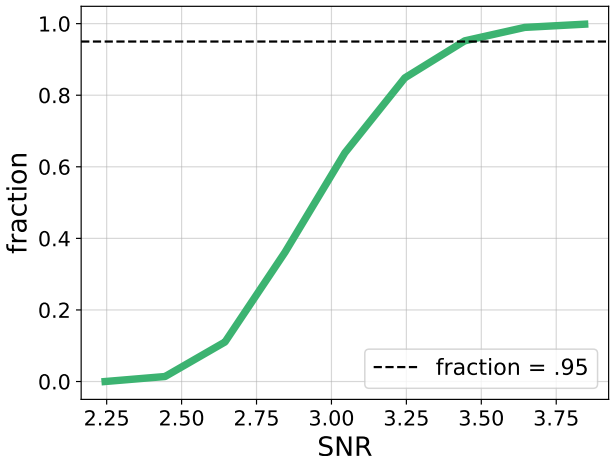

Figure 6.9: CDF of the SNR of the noise distribution for the time-window (60 ns) used in the Vpol. For the pulse selection, a SNR of 3.5 is chosen.

6.3.3 Pulse Selection

Although the global timing is determined, due to an imperfect vertex reconstruction and an inperfect signal model, the exact positions of the other pulses cannot be verified exactly from this. However, the rough pulse position can be determined. Therefore, the reconstruction voltage template is correlated with the data in a time-window around this pulse position to match the template exactly with the data.

Finding the exact pulse-timing for the waveform with the use of correlation will for low SNR events however be highly influenced by noise and the position will be determined by noise fluctuations. Therefore, including low SNR traces will always overestimate the power in the specific pulse. Thus, we determine if there is a pulse in the specific time-window by an SNR > 3.5 cut, which is used as a basic pulse selecter. Figure 6.9 shows the distribution of SNR for pure noise for the time-window used in the fit. 95% of the noise corresponds to an SNR < 3.5.

6.3.4 Fitting Options

Various options have been studied, in order to evaluate the performance for the direction reconstruction for an RNO-G station.

Phased Array Cluster The first option includes only the triggered pulse in the phased array and uses the phased array and the nearby Hpols for the reconstruction. The position of the triggered pulse in the phased array can be established as described in section 6.3.2. On top of the phased array, with only 1 meter seperation, two additional Hpols are included, for which the pulse position can also be fixed using the expected time delays with respect to the recontructed vertex position. Here, the shape of the waveforms in the phased array give information for the viewing angle, whereas the additional Hpols give constrains on the polarization. The test statistic for the single pulse fit with the phased array cluster is:

$$\chi^2 = \sum_{V_{\mathrm{PA_V}}=1}^{v_\mathrm{V}} \sum_{i=1}^{n_\mathrm{V}} \frac{(x_i - f_i(\theta,\phi,E))^2}{\sigma_\mathrm{V}^2} + \sum_{V_{\mathrm{PA_H}}=1}^{v_\mathrm{H}} \sum_{i=1}^{n_\mathrm{H}} \frac{(x_i - f_i(\theta,\phi,E))^2}{\sigma_\mathrm{H}^2} \tag{6.10}$$

+ Pulses SNR $>$ 3.5 The advantage of the forward-folding approach is that all antennas and different ray types can be included in the same minimization. This option includes besides the phased array cluster also all time-windows that include a noticable pulse, as described in section 6.3.3. Consequently, the test statistic is:

$$\begin{aligned}\chi^2 = &\sum_{V_{\mathrm{PA_V}}=1}^{v_\mathrm{V}} \sum_{i=1}^{n_\mathrm{V}} \frac{(x_i - f_i(\theta,\phi,E))^2}{\sigma_\mathrm{V}^2} \\ &+ \sum_{V_{\mathrm{PA_H}}=1}^{v_\mathrm{H}} \sum_{i=1}^{n_\mathrm{H}} \frac{(x_i - f_i(\theta,\phi,E))^2}{\sigma_\mathrm{H}^2} \\ &+ \sum_{V_{\mathrm{SNR}>3.5_\mathrm{V}}=1}^{v_\mathrm{V}} \sum_{i=1}^{n_\mathrm{V}} \frac{(x_i - f_i(\theta,\phi,E))^2}{\sigma_\mathrm{V}^2} \\ &+ \sum_{V_{\mathrm{SNR}>3.5_\mathrm{H}}=1}^{v_\mathrm{H}} \sum_{i=1}^{n_\mathrm{H}} \frac{(x_i - f_i(\theta,\phi,E))^2}{\sigma_\mathrm{H}^2}\end{aligned} \tag{6.11}$$

This option uses only the antennas in the fit (besides the PA cluster) that are selected to have pulses SNR $>$ 3.5 in the pulse windows according to the vertex position, by `rayTypeSelecter` as described in section 6.3.2, which significantly reduces computing time with respect to including all antennas of the station.

6.3.5 Filters and Time-Windows

The Vpol waveforms are filtered with a high-pass filter of 50 MHz and a low-pass filter of 700 MHz, which is the sensitivity regime of the IGLU amplifiers. Since the Hpol is sensitive in a smaller frequency band, for the Hpol a high-pass filter of 200 MHz and a low-pass of 500 MHz is used.

Since the Vpol is more broadband, and because of the larger group-delay of the Vpol than the Hpol, the Vpol pulses are longer in time. For the Vpol, a timewindow per pulse of 60 ns is found to work reliably. The pulse position found by the *rayTypeSelecter* corresponds to the position near the maximum of the waveform. The time-window for a Vpol pulse corresponds to 10 ns before this pulse position and 50 ns after. The corresponding positions for the Hpol are chosen to be 10 and 40, both after the pulse-position, resulting in a total time-window of 30 ns.

Filters and time-windows can be given as an option for the reconstruction easily, both seperate for the Vpols and Hpols, where the above mentioned settings are the default options.

6.3.6 Overlapping Pulses

When two pulses arrive very closely in time at the same antenna (direct and a refracted ray), the time-windows of the two pulses can overlap. This might result in that the wrong

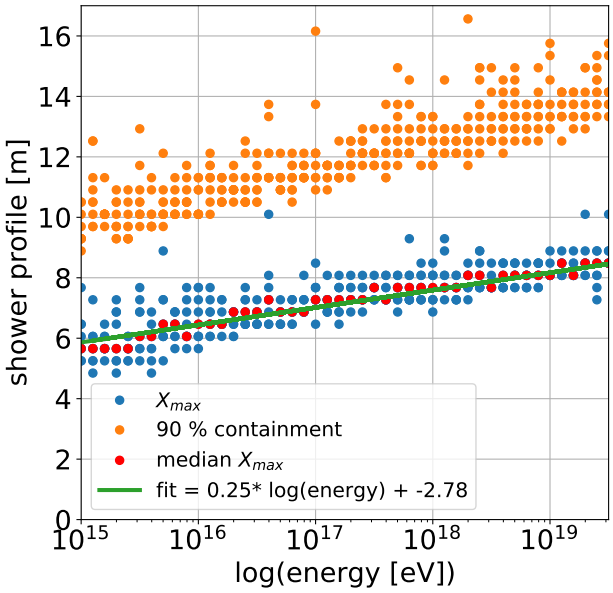

Figure 6.10: The *ARZ2020* shower library, indicating the shower maximum X_{max} (blue) dependent on the shower energy E_{sh}. In orange, the 90% containment of the charge excess is indicated. In red, the median X_{max} per energy is shown, which is used to parametrize $X_{\text{max}}(E_{\text{sh}})$.

pulse is found while correlating the template with the data within the time-window, leading to a miss-reconstructed neutrino direction. Since perfect-timing is not known due to a non-perfect vertex position, and a non-perfect electric-field model, this is at this stage unovercomable and therefore the antennas with overlapping time-windows are excluded from the fit.

6.3.7 Electric-Field Models

There are two options given for electric-field models used in the reconstruction. The *Alvarez2009* parametrization and templates of the *ARZ2020* model. Each of the electric-field models are extensively described in section 5.1.2. In theory every parameterization in NuRadioMC can be easily used for the reconstruction, although in this work only the impact of *Alvarez2009* parametrization is shown, since it is the most realistic parameterization available.

***Alvarez2009* parametrization** As explained in section 5.1.2, the *Alvarez2009* model parametrizes the electric field for the shower energy E_{sh} and the angle between the shower axis and the observer, the viewing angle Θ_{view}. Here, the viewing angle is calculated with respect the position of the shower maximum X_{max} , i.e. where most of the radio emission comes from ($\Theta_{\text{view}} = \Theta_{X_{\text{max}}}$). The viewing angle with respect to the vertex position ($\Theta_{\text{view}} = \Theta_{\text{vertex}}$, as used in NuRadioMC) can be obtained by geometry (section 5.1.4). Then, $\Theta_{X_{\text{max}}}$ is estimated by parametrizing the shower maximum X_{max} dependent on energy, using

$$\Theta_{\text{max}} = \arctan\left(\frac{R \cdot \sin(\Theta_{\text{vertex}})}{R\cos(\Theta_{\text{vertex}}) - X_{\text{max}}(E_{\text{sh}})}\right). \tag{6.12}$$

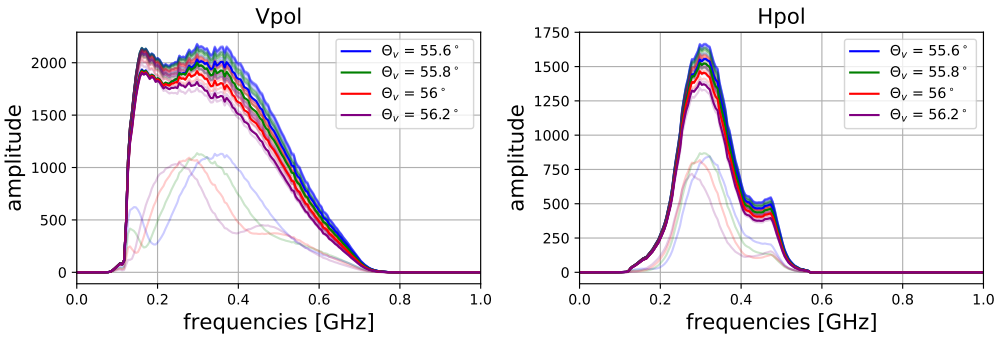

Figure 6.11: Voltage traces in the frequency domain for the Vpol (left) and Hpol (right) for four viewing angles around the Cherenkov angle. The transparent colors are the traces due to the various shower profiles available for the *ARZ2020* model. The dark lines indicate the voltage due to averaged shower profile of these showers, which is used to generate the *ARZ-templates*. Shown is that most showers from the library result in very similar shapes, only varying in amplitude. However, sometimes a neutral pion decays instead of interacting leading to an electromagnetic sub-shower, which experiences the LPM effect, which explains the low amplitude spectra.

Here R is the propagated distance of the radio signal. $X_{\max}(E_{\text{sh}})$ is estimated by a linear fit performed to the median $X_{\max}$ per E_{sh} as shown in figure 6.10, using the shower profiles of the *ARZ2020* library (the library is explained in section 5.1.2).

***ARZ2020*-templates** Calculation of the *ARZ2020* electric field is computationally expensive since it involves convolutions of the Askaryan vector-potential with Monte-Carlo generated shower profiles. Reconstructing with the *ARZ2020* semi-analytic model is therefore time-consuming. Moreover, a variety of showers is available for the charge distributions, resulting in small fluctuations for the showers. To overcome both problems, electric-field traces of the *ARZ2020* model are tabulated and used for the reconstruction. The averaged shower profile of the available showers is used to create an electric-field template, as shown in figure 8.5 of appendix D. The variety for a single event for near Cherenkov angle events is shown in figure 6.11, where the dark lines indicate the shower due to the averaged shower profiles. For these templates, a viewing angle spacing of 0.2° is used and an energy E_{sh} spacing of 0.02 in $\log(E_{\text{sh}})$ is used. Furthermore, the *ARZ2020* model is slightly propagation distance dependent and therefore a variety of distances are tabulated. The template is then scaled with $\frac{E_i}{E_{\text{template}}}$ and $\frac{R_{\text{template}}}{R_i}$, where E_i and R_i are the input energy and propagation distance for the reconstruction respectively.

6.3.8 Parameter Space

As mentioned in 6.1.1, knowledge of the signal arrival direction restricts the neutrino direction to a broad band of $\approx 10^\circ$ on the sky. This is illustrated with the red band in figure 6.12. A more precise knowledge of viewing angle reduces this region. This determines the allowed neutrino arrival directions for the reconstruction, as indicated by the orange band in the figure.

The reconstruction uses a brute force approach to find the most likely value and then runs a scipy minimizer around this value. For the signal arrival direction, a range of viewing angles Θ_{view}, and all angles R in $[0^\circ, 360^\circ]$, the neutrino direction is determined and used as

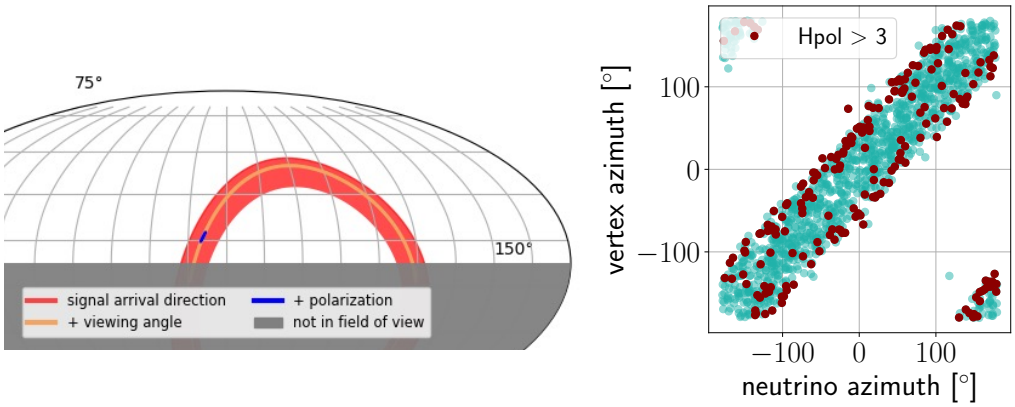

Figure 6.12: Left: Geometry of limited region for the neutrino direction if the signal direction (red), viewing angle (orange) and polarization (blue) is known. The orange band is used as the parameter space for the recontruction. Right: Due to the geometry of the shower, the azimuth direction of the neutrino is roughly oriented towards to the direction of the neutrino. Therefore, this is used to limit the parameter space for the azimuth direction for the reconstruction.

input. Furthermore, a range of shower energies is scanned per Θ_{view} and R.

To limit the range of viewing angles and shower energies, the phased array cluster is used to get a rough estimate on the energy and the viewing angle, which are mainly determined by the amplitude and the shape of the waveforms in the Vpols respectively.

Furthermore, since upgoing neutrinos will not reach the RNO-G detection volume due to earth absorption, the zenith direction can be limited to 100°. Also, since the emission is in the direction of the shower propagation, geometry restricts the azimuth direction of the vertex position to ≈100° in azimuth, as shown in figure 6.12 right.

6.4 Forward-Folding Performance for RNO-G

In this section, the performance of the reconstruction will be shown. The purpose of this section is to show the impact and the potential of an RNO-G station, as well as the influence of the chosen emission model and electric-field description. This section describes the performance of the fitting procedure and chapter 7 will outline the angular resolution for RNO-G, i.e. the physics implication.

First, the impact on the angular difference between the reconstructed and the true value due to the combination of different antennas with an RNO-G station and ray types is shown. Next, the reconstruction performance will be shown limited to the phased array and the corresponding Hpols (phased array cluster). Additionally, the full RNO-G station is used. These studies will be performed with *Alvarez2009* simulations, using an event set of a single energy of 10^{18} eV, to purely study the effect of the station and the variety of antennas within the station. For most sub-studies the simulated vertex is used as input for the forward-folding, unless explicitely stated otherwise.

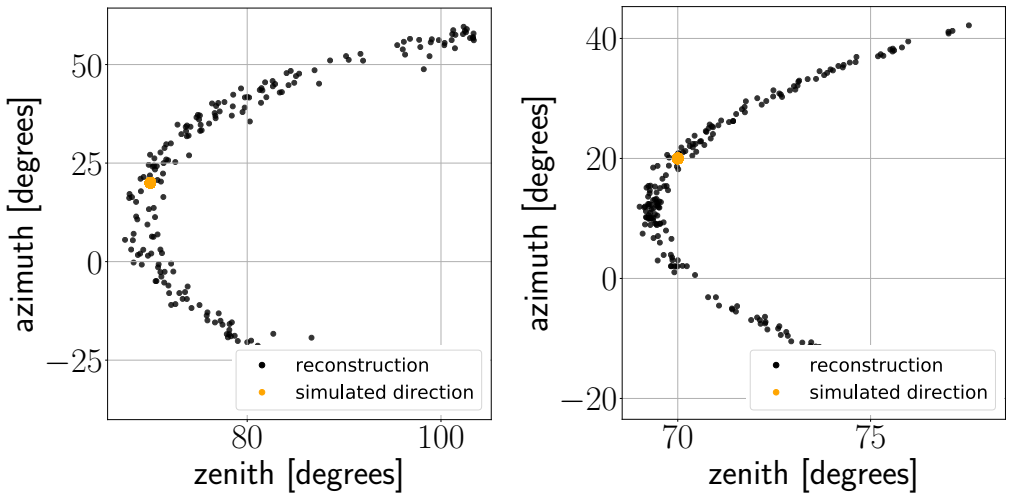

Figure 6.13: Left: Spread of the neutrino direction reconstruction using a single antenna and a single ray type (direct). Seen is a band covering the full sky, until zenith 100° (end of parameter space). Right: Similar as left, using the direct and the reflected ray type of the same antenna. The spread is significantly reduced in zenith and azimuth. Furthermore, the width of the band is decreased, due to an improved viewing angle resolution. Note the changing axis.

Next, in section 6.4.4, the impact of the more realistic *ARZ2020* model will be shown, using the *Alvarez2009* as well as the *ARZ*-templates as reconstruction module.

6.4.1 Impact of Combining Pulses

As described in section 6.1.3, the viewing angle of the signal arriving at an antenna can constrain the neutrino arrival direction to a band on the sky. To show this, a study is performed with a single neutrino ($\theta_\nu = 70$, $\phi_\nu = 20$, $E_\nu = 10^{19}$ eV) which is reconstructed 200 times with varying thermal noise. Figure 6.13 left shows the spread in reconstructed values for the neutrino direction using the triggered pulse in the phased array, including a single antenna. As can be seen, the neutrino arrival direction can be restricted to a band, ranging widely in zenith and azimuth since no polarization information is included. The width of the band is determined by the resolution of the viewing angle reconstruction.

Including a reflected pulse in the reconstruction for this event limits the neutrino arrival direction to a smaller range of allowed directions, due to different band that is described by the viewing angle corresponding to this ray type. Figure 6.13 right shows the distribution of reconstructed directions using the same phased array antenna inluding a direct and reflected ray in the reconstruction. Clearly seen is the limited range of possible zenith and azimuth directions, covering only roughly 6° in zenith. Furthermore, the band is more narrow than using the a single pulse, caused by a better resolution for the viewing angle.

Further constraining is expected by including more information in the reconstruction. Figure 6.14 visualizes the expected neutrino arrival direction range by looking at the overlap of several viewing angle cones of this same event. Note that this figure is purely geometry, and does not entail any simulations or reconstructions. Each band due to the viewing angle of each included pulse is indicated in yellow, and colours are getting darker when the bands are overlapping, resulting in purple where they all the bands cross. Figure 6.14 left includes the direct rays of the Vpols in the full station. Due to the vertically displaced antennas,

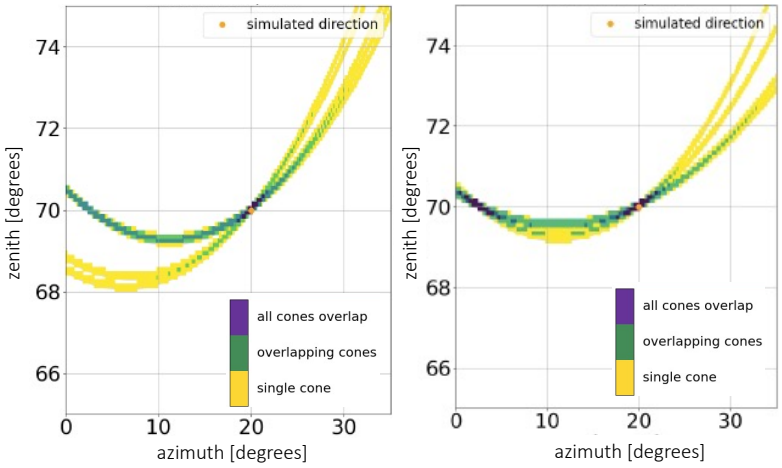

Figure 6.14: Geometry of the allowed region for the neutrino direction using a viewing angle uncertaingy of 0.5°. The same event of figure 6.13 is used, now for the direct and reflected ray of two Vpols (left) and for the direct ray of 5 Vpols (right). The regions due to the viewing angle are indicated in yellow, the overlap of these in green and the cross point of all in purple.

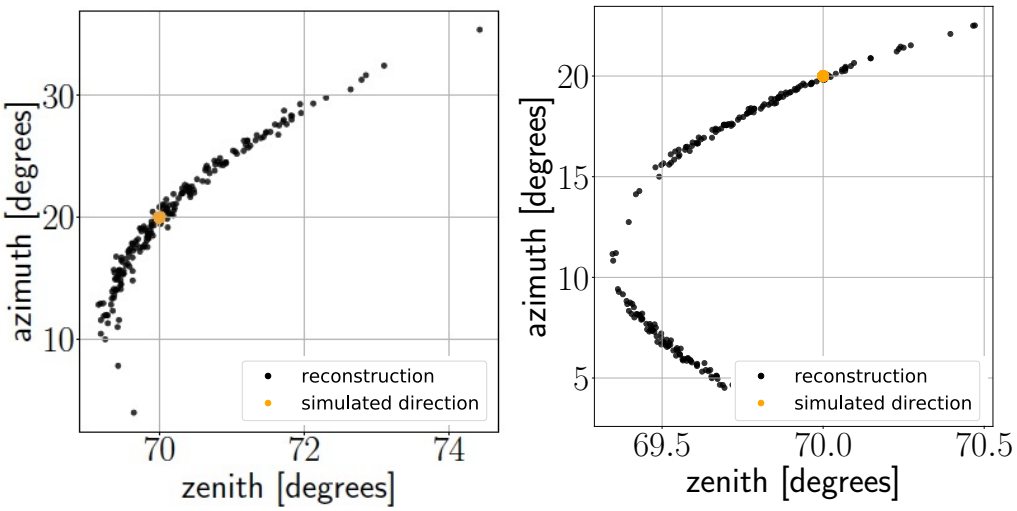

Figure 6.15: Spread of the neutrino direction reconstruction using the same event of figure 6.13. Left: The direct and reflected ray type of 2 Vpols are used (corresponding to figure 6.14 left). Right: The direct ray of 5 Vpols are used (corresponding to figure 6.14 right. Seen is in the right figure, is that the zenith direction can be determined within 1°. Note the changing axis.

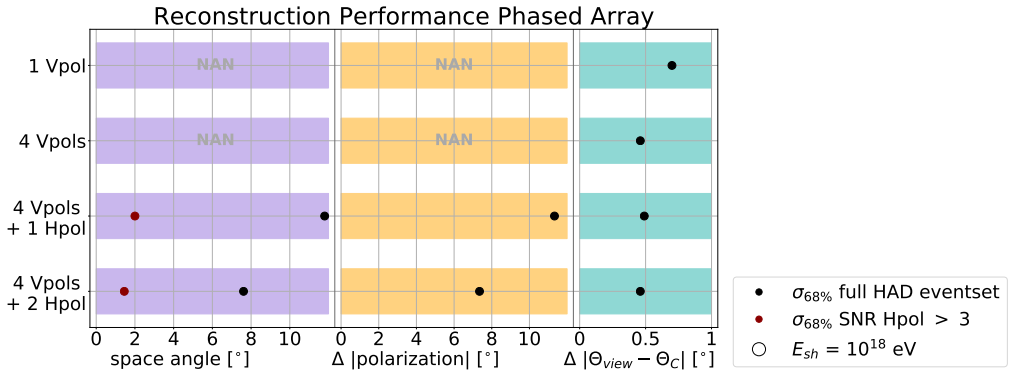

Figure 6.16: Resolution ($\sigma_{68\%}$) of the space angle (left column), polarization (middle column) and the viewing angle (right column) for using the phased array and its nearby Hpols. For the space angle, indicated in red are the events with a significant contribution in the Hpol (SNR > 3).

the change in viewing angle and signal direction results in two very discrete bands with an intersection point. Figure 6.14 right shows the overlap for two antennas with a direct and are reflected ray. Because four pulses are included, the viewing angle can be reconstructed more precise than for figure 6.13 right, and therefore the crossing of the bands result in two discrete areas, which correspond to opposite polarization angles.

Figure 6.15 left (right) shows the reconstruction using the same antennas as for figure 6.14 left (right). Although there are no Hpol included in the fit, the zenith angle for the neutrino direction can be determined within a degree for 6.14 right.

6.4.2 Phased Array Cluster

The Hpol antennas above the phased array could be used for the antenna unfolding (making use of equation 6.1) to reconstruct the polarization, since they are expected to detect the same electric field as the phased array due to their close-by position. Using the forward-folding technique has the advantage that slight changes in the electric field will be included and that, even for low SNR, adding more antennas will cause noise-reduction. The data set of 10^{18} eV neutrinos is used to study the resolution that can be obtained with the phased array and its nearby Hpols.

Results are shown in figure 6.16. Using all four Vpols of the phased array reduces the viewing angle resolution of $\sigma_{68\%} = 0.7^\circ$ for a single Vpol to $\sigma_{68\%} = 0.48^\circ$. The viewing angle can be very well reconstructed for events with an SNR in the phased array antennas of larger than 2.5. Adding the Hpols to the reconstruction will also give information on the polarization. The polarization can be reconstructed to $\sigma_{68\%} = 11^\circ$ for adding an Hpol, and reduces to $\sigma_{68\%} = 7^\circ$ for the two Hpols. Also shown in the figure is the space angle, which is the angle between the reconstructed and the true direction and which will be used as the measure of the angular resolution in this chapter. Using the full phased array and the two nearby Hpols, reduces the space angle for events with large Hpol contribution from $\sigma_{68\%}$=2° to $\sigma_{68\%}$=1.4°.

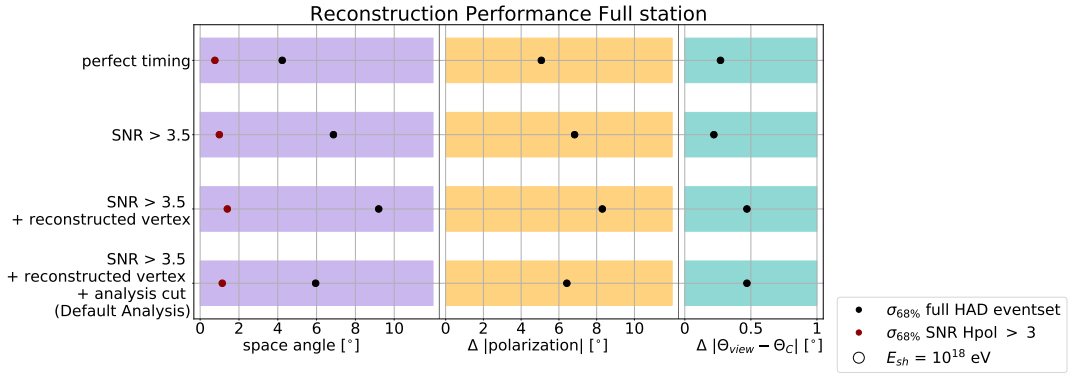

Figure 6.17: Resolution ($\sigma_{68\%}$) of the space angle (left column), polarization (middle column) and the viewing angle (right column) for the full RNO-G station. From top to down, the rows describe 1. performance assuming perfect timing (all pulses included and true vertex position), 2. performance assuming perfect timing, but excluding pulses outside the phased array cluster with SNR < 3.5, 3. similar as 2 but including reconstructed vertex and 4. the default analysis (including the phased array cluster and pulses in the rest of the station with SNR > 3.5, reconstructed vertex and analysis cuts as wil be described in section 7.1.2). For the space angle, indicated in red are the events with a significant contribution in the Hpol (SNR > 3).

6.4.3 Full Station

The polarization resolution is highly dependent on the type of event. When information is available in the Hpol (SNR > 3), the polarization can be obtained very precisely. When information in the Hpol is lacking, the specific signature of the event determines how much the polarization can be restricted, and therefore how well the direction of the neutrino can be determined. To study the potential of the angular resolution using all pulses arriving at the various antennas of an RNO-G station, the reconstruction is performed on the full station assuming perfect timing. This means, that all raytracing solutions are used in the fit, assuming that the pulse position can exactly be established, and assuming a perfect vertex position. Results are shown in figure 6.17 top row. Note that the viewing angle can be established within $\sigma_{68\%} = 0.27^\circ$, which is an improved compared to the usage of only the phased array as shown in section 6.4.2. The full event set reconstructs 68% of all events within 4° and to 0.74° for events with a large Hpol contribution.

Since the exact position of all the pulses cannot be established, pulses arriving with a very low amplitude cannot be included in the fit, as explained in section 6.3.3. Therefore, besides the phased array and the nearby Hpols, only pulses are included with an SNR > 3.5. The impact of reducing the information used in the reconstruction is shown in the second row of the same figure. Whereas events with large Hpol contribution reconstruct equally well, for the full event set the space angle increases to 6.5°.

The last two rows of the figure show the resolution of the space angle, polarization and viewing angle for including the reconstructed vertex as obtained with the method described in section 6.2.2. The bottom row also includes event quality cuts, as will be discussed in 7.1.2.

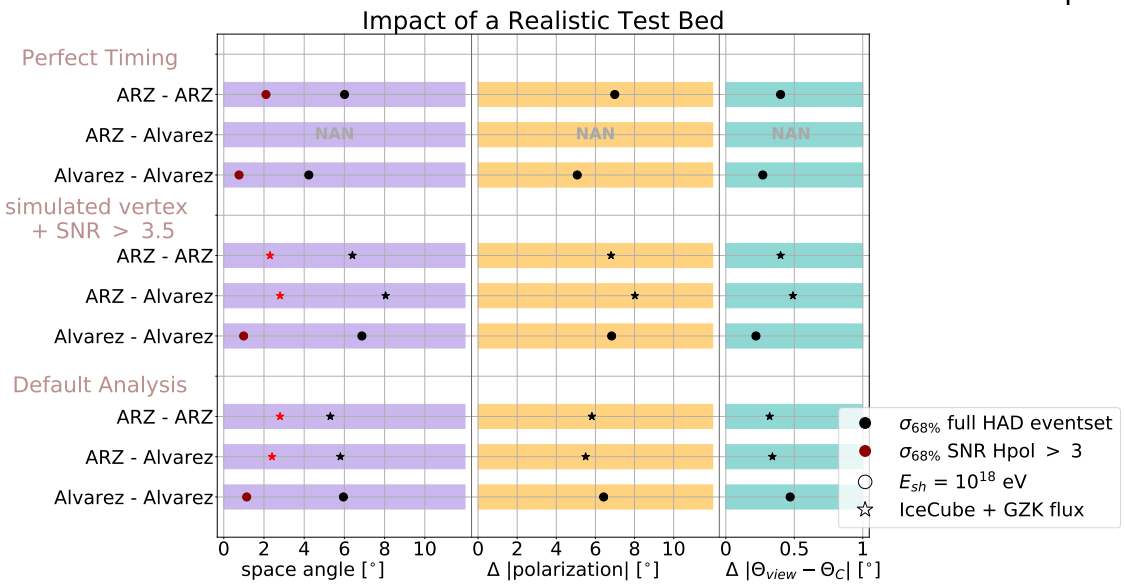

Figure 6.18: Resolution ($\sigma_{68\%}$) of the space angle (left column), polarization (middle column) and the viewing angle (right column) for the full RNO-G station. From top to down, the rows describe 1. performance assuming perfect timing (all pulses included and true vertex position), 2. performance assuming perfect timing, but excluding pulses outside the phased array cluster with SNR < 3.5, 3. the default analysis (including the phased array cluster and pulses in the rest of the station with SNR > 3.5, reconstructed vertex and analysis cuts as wil be described in section 7.1.2). For each category, the *Alvarez* as well as the *ARZ* simulation set is used, indicated as *Simulation Model - Reconstruction Model*. For the space angle, indicated in red are the events with a significant contribution in the Hpol (SNR > 3).

6.4.4 Impact of a Realistic Signal Model

The most realistic electric-field model available for in-ice Askaryan emission is the model from [144] and is available as the *ARZ2020* model in NuRadioMC as a shower library per energy. The shower library is described in 5.1.2, as well as the differences between this semi-analytic model and the *Alvarez2009* parametrization. There is no phase information included in the *Alvarez2009* model (as explained in section 5.1.2).

Describing with the *Alvarez2009* parametrization Results of the performance of the reconstruction with the *Alvarez2009* parametrization on a *ARZ2020* simulation set, which uses the flux models described in 7.1.1 are shown in figure 6.18. The middle row shows the the performance for the reconstruction set-up (excluding pulses with SNR < 3.5) making use of a perfect vertex position. This results in a resolution of the space angle of $\sigma_{68\%} = 5.7°$ for which the polarization is the main contributor. The default analysis (reconstructed vertex and analysis cuts, as will be explained in section 7.1.2) gives slightly better results. A viewing angle resolution of 0.43° can be obtained, which is improving for larger amplitude events, as shown in appendix B.

Describing with *ARZ*-templates To improve the signal model the *ARZ*-templates, as described in section 6.3.7, are used for the reconstruction. The viewing angle results in a similar resolution of 0.4° and is also SNR dependent. The polarization is similar described as with the *Alvarez2009* parametrization. Therefore, for the realistic data set, including full knowledge of the signal model, only slightly improves the results.

As already discussed in figure 6.11, there are small shower-to-shower fluctuations. Especially for viewing angles nearby the Cherenkov angle, the showers can vary significantly. For nearby vertices, the change in viewing angle within the phased array and the nearby Hpols can be $\approx 0.2^{\circ}$ for a meter spacing. The individual showers, due to the different shower profiles, behave sligtly different for different viewing angles and can for near Cherenkov angle events lead to a significant change in amplitude, leading to an offset in the polarization reconstruction. This effect is shown for an example shower library in appendix D. Therefore, the angular resolution is not converging for large SNR in the Hpol.
Also shown in figure 6.18 (top row) is the performance of the different signal models assuming perfect knowledge of the pulse positions and the vertex position, to show the maximum possible improvement on the neutrino direction with the available information. Note that the *ARZ - Alvarez* is left empty for this categorie. Because *Alvarez2009* has no phase information included, the timings of the waveforms do not correspond, leading to inreliable results assuming perfect timing for the reconstruction.

6.4.5 Energy Resolution

As a by-product of this fitting approach, the shower energy is reconstructed. For the *Alvarez2009* model and the true vertex position, the phased array can limit the energy resolution to $\sigma_{68\%} = 13\%$ for $\log 10(\frac{E_{\text{rec}}}{E_{\text{sim}}})$. The resolution improves to $\sigma_{68\%} = 0.06\%$ for including the full RNO-G station. The final obtained energy resolution for the *ARZ* simulations, including reconstructed vertex, is $\sigma_{68\%} = 14\%$. The data set will be described in 7.1.1 and 7.1.2 and is based on an assumed neutrino flux and includes an event selection based on analysis cuts. All the distributions providing the obtained energy resolutions are shown in in appendix E.

For shallow stations (ARIANNA) the energy resolution is studied to be less accurate for higher energies, due to a larger uncertainty in the vertex positions for higher energies, since higher energy events lead to further away vertices [139; 143]. This is not observed in this results quoted here, because the change in viewing angle for the direct and reflected ray decreases for larger vertices distances (higher energies), which makes it more likely to observe both raytpaths. For a shallow station, almost all events will have a direct and reflected ray, meaning that the only difference comes from the distance of the vertex.

6.4.6 Electromagnetic Showers

For electron neutrinos undergoing a charged current interaction a part of the energy is transferred into a electromagnetic shower. The waveform observed at the detector is the result of the interference of the electromagnetic and hadronic component of the shower. Due to stochastic nature of the shower development effected by the LPM elongation there is a lot of variability between showers, making the waveform hard to predict [91]. The electromagnetic showers are in more detailed discussed in section 3.4.2. While very little event-to-event fluctuations are observed for the lower energies around 10^{16} eV, they start to play an important role for the higher energies, resulting in complete random waveforms around 10^{19} eV.

The *Alvarez2009* model, which is used for most of the performance studies in this chapter, includes some statistical variations due to the LPM effect by elongating the pulse according

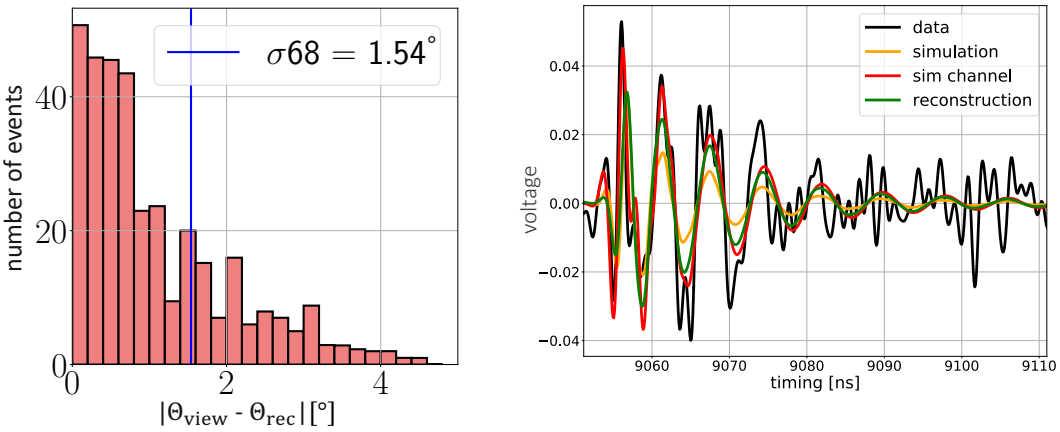

Figure 6.19: Left: Viewing angle resolution for the reconstruction of electromagnetic showers. Right: Example event for the reconstruction of electromagnetic showers. Seen is the large deviation in amplitude between the data (red) and the simulation (orange).

to a Gaussian distribution. However, these time-domain waveforms are not realistic and far off from the more accurate *ARZ2020* simulations. Since the waveforms are very fluctuating, the average shower profile, like done for hadronic showers, is not useful. Therefore, we describe the electromagnetic showers with a purely hadronic assumption. An example event is shown for 10^{18} eV neutrino, in figure 6.19, where is clearly shown that the simulated hadronic shower (orange) does not match the data (red). The electromagnetic showers result in a viewing angle resolution of $\sigma_{68\%} = 1.54°$, as shown in figure 6.19 left. The obtained polarization is $\sigma_{68\%} = 10°$.

Therefore, a better signal model is needed to reconstruct electromagnetic showers with this approach, or a seperate method needs to be developed. Recent studies for reconstruction with machine learning has shown to also work for electromagnetic showers [141].

6.5 Possible Improvements

This chapter described the first reconstruction method for the deep component of an in-ice radio detector, making use of the entire station. Naturally, as counts for all reconstruction methods at any stage, several improvements can be made in order to make the reconstruction more precise or computationally more favorable. This chapter indicates several suggestions for next iterations of the forward-folding approach.

The reconstruction outlined in this chapter, makes use of the vertex position to indicate where the pulses are located in the traces. While any pulse position for signals with SNR > 2.5 is easily found by correlating the data with a voltage template, it requires the understanding of a pulse being present or not. An uncomplicated pulse finder is used in this work by applying a threshold cut, as discussed in section 6.3.3. This can be improved by any other pulse finder, which for example uses the correlation with a neutrino template. Futhermore, if such a pulse finder is available pre-selecting all the pulses in the traces can lower the timing of the reconstruction significantly, since only the antennas would have to be included in the fitting procedure which detect signal. Especially for the vertex reconstruction this helps a lot, since it uses the timing delay between each antenna pair. Also, knowing the antennas

which see signal, and eliminating signal-less traces, reduces the impact of noise. Likewise, a small time-window around the identified pulse can be selected to reduced thermal noise impact.

Secondly, the reconstruction of the vertex position can be combined together with the reconstruction of the neutrino direction and energy, i.e. the timing and the waveforms can be combined in a single reconstruction. This way, the phase differences of the waveforms due to different viewing angles can be combined in the reconstruction of the vertex, and therefore a more accurate vertex reconstruction can be obtained. Consequently, allowing to include all antennas in the reconstruction without the pulse selection, and therefore also including pulses that overlap (section 6.3.6). This can also be done in an iterative manner. Viewing angle differences from a direct and a reflected ray can give a handle on the vertex position, which then results in a better estimate of the expected viewing angles at the antennas, etc. This requires the *ARZ*-templates as the model for the electric field, since the *Alvarez2009* does not include phase information.

Furthermore, there are several way to further reduce computing time of the reconstruction. The search area is geometrically limited, and starting values for the viewing angle and shower energy are obtained with a minimizer. But furthermore, the search area is completely scanned in zenith, azimuth and shower energy and is thus taking ≈ 10 minutes per event. MCMC chains can be helpful for including the vertex reconstruction, which adds three dimensions of the vertex position as parameters. Also, a nested minimizer can be used, to make sure that the local minima of the wrong side of the Cherenkov cone is discarded and that the full parameter space is scanned.

6.6 Effects of the Ice

To minimize systematic uncertainties and optimize the angular resolution, a good knowledge of the ice is required, as disucssed in section 3.6. Besides the ice characteristics like the density and the attenuation length, other effects are important for the radio neutrino detectors, i.e. horizontal propagation, reflective layers and birefringence. This section discusses these ice effects, as well as the influence on reconstructing the neutrino properties and the (potential) usage of RadioPropa for these ice studies.

6.6.1 Firn Model

The ice density data taken at Summit Station is suggested to be described by a double exponential function by [111]. Both this model, together with the Summit Station data and the single exponential model as implemented in NuRadioMC (`greenland_simple`) are given in figure 6.20. The double exponential function is referred to as the *firn model* (`greenland_firn`), as it uses a more steep exponential function to describe the upper part of the ice and is described by

$$\begin{aligned} n(z) &= 1.78 - 0.502 \cdot \exp(-z/30.8\,\mathrm{m}) && z \leq 14.9\,\mathrm{m} \\ n(z) &= 1.78 - 0.310 \cdot \exp(-(z - 14.9\,\mathrm{m})/40.9\,\mathrm{m}) && z \geq 14.9\,\mathrm{m} \end{aligned} \tag{6.13}$$

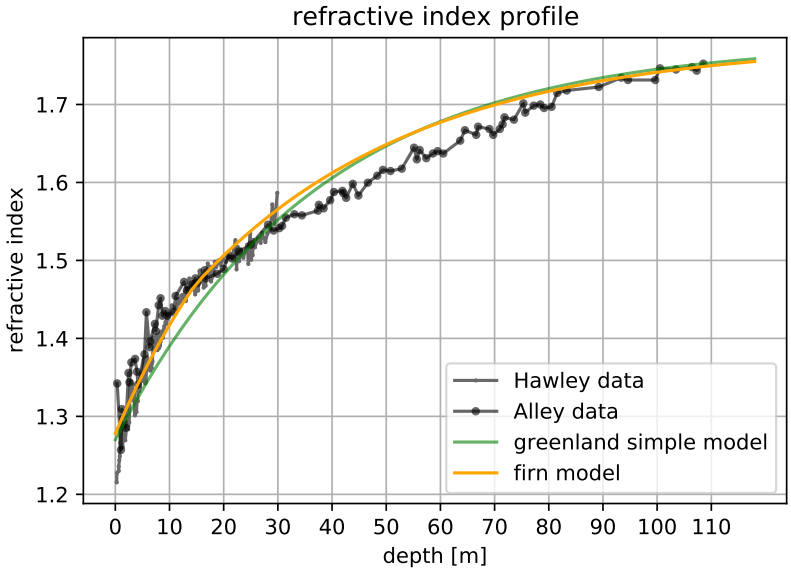

Figure 6.20: Refractive index models fitted to the density data of [111]. In green the `greenland_simple` model is indicated, using a single exponention. Orange shows the `greenland_firn` model, which uses a double exponential function.

The difference between the firn model and the `greenland_simple` model refractive index is maximum 2.1% at the critical depth of 14.9 meters, which is the connection point between the two different exponentials of the firn model. For the deep ice, below 350 m, the ice is the same with a refractive index of 1.78. For more shallow ice, the models start to differ with a maximum deviation point at 14.9 m. While the radio rays for the firn model propagate faster between 350 and 50 m depth, the signal travels faster for the `greenland_simple` model for the upper 50 m. Therefore, the time differences depend a lot on the specific path traveled through the ice and depends on the ray type and the antenna depth. The time-shifts between the two models were studied for antennas at 100 m, 50 m and 20 m deep, as presented in figure 5 of [133]. For the firn model, RadioPropa is used to perform the raytracing, and for the `greenland_simple` model the analytic raytracing, as discussed in section 5.1.3. Because for the direct rays the signal does not traverse the very shallow ice, the travel time for the firn model is expected to be lower, with an increasing effect for more deep antennas. For refracted ray types, the amount of time spend in the shallow and/or deep ice is less trivial and therefore, for more deep antennas, the spread is more broad.

The impact of these time-differences due to the firn model can be evaluated by performing the direction reconstruction outlined in this chapter with the firn model on a data set created with the `greenland_simple` model. Because of the changes in timing between pulses arriving at the antennas as well as the timing differences between various ray types, the signal direction is influenced by this. The angular resolution on the signal's zenith obtains a larger and asymmetric spread. As expected, especially the vertex reconstruction is influenced by the time-differences, as shown in appendix C. It results in a larger spread for the neutrino zenith ($\approx 1^\circ$) as well as azimuth direction and a bias in the zenith direction of 0.4°.

Besides the impact on the waveforms due to the different propagation times, a different ice model influences the so-called *shadow zone*, which is the near-surface volume in the ice from where no signals can be observed in the receiving antennas due to the raybending (as dis-

cussed in 3.6). The two-exponential firn model results in more raybending, and therefore in a larger shadow zone, which therefore reduces (although slightly) the effective volume of the detector. This is visualized in figure 4 of [133].

6.6.2 Horizontal Propagation

FDTD simulations (discussed in section 5.1.5) of radio signals propgating in the ice expect besides the classical raybending in the firn other modes that caus the signal to be able to originate from the shadow zone [111]. When the rays reach the ice-air boundary at an angle larger than the total internal reflection angle, a fraction of the signal will couple into a mode that is propagating along the surface. Furtermore, the signal can be received from the shadow zone because the signals propagate horizontally at an arbritrary depth. Due to annual snow deposits, the density gradient at a specific depth could contain perturbations, which may result in the coupling of a fraction of the signal to propagate horizontally for rays that are bended in the ice which become horizontally in the specific depth range of the perturbations. Small amplitude signals from the shadow zone at shallow depths have indeed been observed by the ARIANNA experiment [110]. To mimic the effect of horizontal propagation, a new module `HorizontalPerturbation` is implemented in RadioPropa. The implementation follows the suggestion by [111], in which it will propagate a fraction of horizontally reaching refracted rays in predefined depths in a horizontal layer instead of bending down again. The implementation contains 2.3% electric-field fraction and an attenuation length of half that of the bulk ice, as also suggested by [111]. Naturally, the occurence of horizontal propagation increases the effective volume of the detector.

6.6.3 Reflective Layers

Vertically arriving cosmic rays can result in air showers that are not fully developed yet while reaching the Earth's surface. Reaching the ice, these air showers will further develop and produce radio emission within the ice sheet and therefore they could trigger an RNO-G station [101]. If these signals are reflected on layers in the deep ice (*reflective layers*), these cosmic-ray events cannot be vetoed by their direction. Measurements have shown that these layers are indeed present [102]. These events might be vetoed due to horizontal propagation of the radio signal they emit, since they are coming from above and therefore always travel in the firn. As well for this horizontal propagation, as the effect of the reflective layers RadioPropa can be a useful tool to study this.

6.6.4 Birefringence

At the South Pole, the propagation of the radio signal is measured to be polarization dependend and therefore resulting in significant time delays for horizontally- and vertically polarized antennas which has been explained by *birefringence* models for near-horizontal propagation [145], for vertical propagation [146] and for the general case [147]. Ice is a biaxial media, meaning that the permittivity matrix contains three different refractive indices which directions are defined by the flow of the ice sheet. The strength of this effect depends on allignments of the ice crystals which are determined by the speed of the ice flow. At the Summit Camp site, however, the ice flow is slow (1.33 m per year, measured at a different site of the Greenland ice sheet [148]) and therefore a lack of strong horizontal preference

in the ice crystal fabric is expected, although currently specific birefringence measurements are lacking. The amplitude of the signal gets decomposed according to the preferred polarization directions due to the ice flow, and therefore a good understanding of the birefringent behavior of the specific ice sheet is required in order to obtain a good polarization estimate. Also, this decomposition will reduce the effective volume of the detector. Furthermore, due to the difference in arrival time for the various polarization components, a good modeling of the birefringence is required to obtain the exact pulse-timings for low signal events. However, if a good model is available, and if high signal amplitudes are observed in antennas detected different polarizations, time-delay between the arriving pulses can be used to probe the vertex distance.

Chapter 7

Angular Resolution for RNO-G

...minngaaneerpunga
— *Greenlandic for* I'm from...

Making use of the developed reconstruction method in chapter 6, the angular resolution for RNO-G can be obtained. This chapter discusses the expected RNO-G event distribution, analysis cuts (section 7.1) and the resulting angular resolution (section 7.2) and corresponding covered sky area (section 7.3). Next, a discussion is given on the implications of the angular resolution for neutrino source searches in section 7.4. Furthermore, section 7.5 gives an outlook on the improved resolution for showers that trigger more than a single RNO-G station, the so-called *coincidence events*. Finally, recommodations for in-ice radio neutrino detectors are given followin g the results of this chapter (section 7.6).

Φ_{astro}	γ_{astro}	m	α	$R_{\text{cut-off}}$	f_p at $E = 10^{19}$ eV
1.01	2.19	3.4	2.5	100 EeV	10%

Table 7.1: The parameters for the flux used to generate an event set for RNO-G, which contains an astrophysical neutrino flux as well as a cosmogenic neutrino flux. Here, Φ_{astro} is the astrophysical flux normalization, γ_{astro} the spectral index of the astrophysical flux as obtained by [149]. For the cosmogenic neutrino flux, a model from [150] is used, with source evolution parameter m, spectral index of the injection spectrum α, proton fraction f_p and cut-off rigidity $R_{\text{cut-off}}$.

7.1 Analysis Efficiency and Event Distribution

To study the angular resolution of RNO-G an astrophysical and cosmogenic neutrino flux model is assumed to generate an event set. This section discusses the flux model as well as the characteristics of the RNO-G event distribution. Furthermore, quality cuts as well as the neutrino zenith and the shower energy dependence of the event distribution are discussed.

7.1.1 Event Distribution

To study the angular resolution of RNO-G, a realistic event set is generated using an astrophysical and cosmogenic neutrino flux model based on [149] and [150]. The specifics of this neutrino flux model are given in table 7.1. The event set contains neutrino events with generated electric fields of the *ARZ2020* signal model (see section 5.1.2). For the trigger a 2-σ single Vpol trigger is used, as proxy for the phased array trigger. The resulting event distributions for hadronic showers are shown in figure 7.1. These distributions are weighted, as described in section 5.1.1. RNO-G is less sensitive for declined showers as can be seen in figure 7.1 top left. The favor for more inclined showers breaks down however for near horizontal directions, due to Earth absorption for high energies (E $> 10^{16.5}$ eV), and due to the lack of vertically polarizared electric field and the phased array trigger for the lower energies. Altogether, RNO-G is most sensitive for neutrinos arriving around 70°. Furthermore, RNO-G expects to see most events around $10^{17.5}$ eV (bottom left), due to the lower effective volumes for lower energies due to the smaller amplitude events, and the lower flux expectations at the higher energies. Also shown is the distribution of the signal-to-noise ratio (SNR) in the phased array Vpol and nearby Hpol (bottom right). While the SNR of the Vpol is not lower than 2, due to the threshold of the trigger, most events have an SNR of 2.5 (just above trigger threshold) with a long tail towards higher SNR values. For the Hpol, most events have an SNR lower than 2, and the fraction is strongly diminishing for larger signals. The figure shows in orange and pink event distributions after the analysis cut, which will be discussed in section 7.1.2.

The event distribution shown in figure 7.1 excludes charged current electron neutrino interactions and therefore only contains hadronic showers. This distribution is used for the analysis given in this chapter and all the results shown.

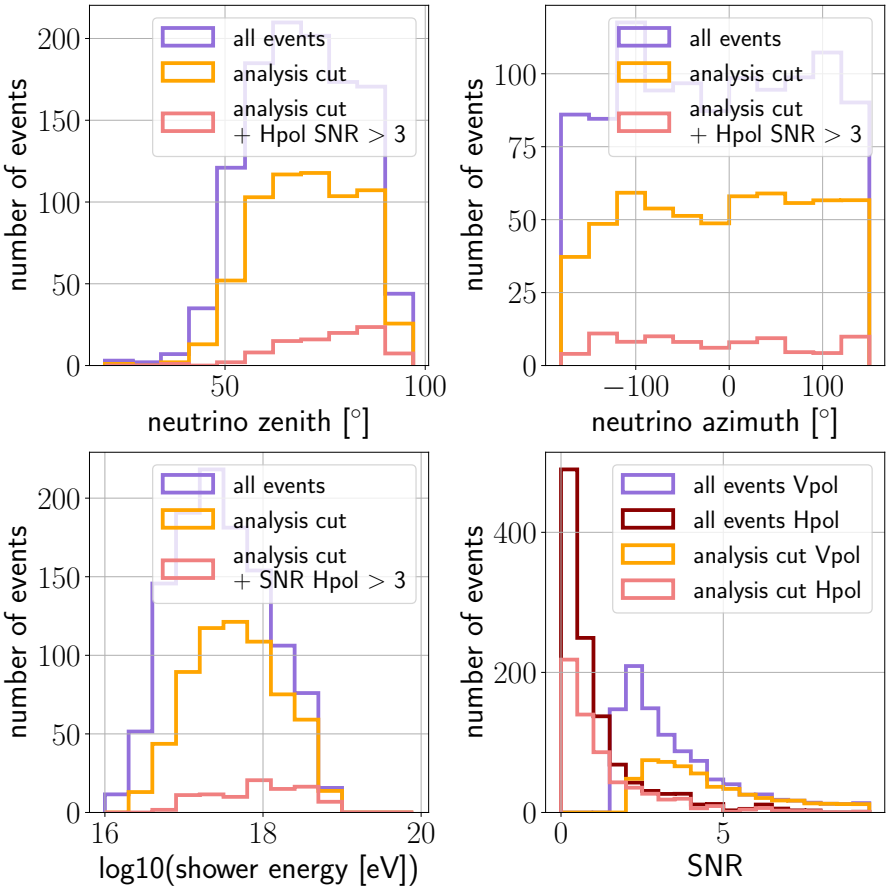

Figure 7.1: Hadronic event distribution for an RNO-G station assuming a flux containing the extension of the IceCube flux and a GZK model. Indicated in orange is the event distrubtion after the analysis cut.

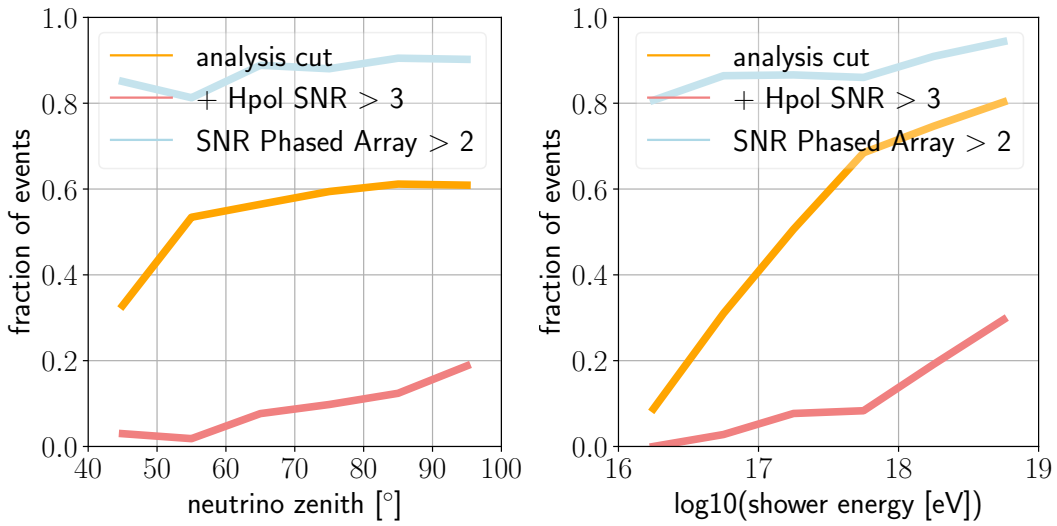

Figure 7.2: Zenith (left) and energy (right) dependent SNR distribution for an RNO-G station. The orange line indicates the analysis efficiency for RNO-G, i.e. a signal of SNR > 2 in the phased array, the helper strings and the antenna at -80 m. Furthermore, a better angular resolution can be obtained for the subset of events with a strong signal in the Hpol (SNR > 3), which is indicated by the pink line.

7.1.2 Analysis Cuts

As discussed in section 6.2, the analysis cut for the outlined reconstruction method is detectable signal in each of the helper strings and an other Vpol on the power string besides the phased array in order to require a good signal direction and vertex reconstruction. This section discusses the implications for RNO-G and shows the energy and zenith dependence of the event distribution that are part of the high quality event set that is reconstructable.

7.1.2.1 Neutrino Shower Energy Dependence

The shower energy dependent efficiency for an SNR cut of 2 is shown in figure 7.2 right, indicated with the orange line. In order to improve the reconstruction with a good polarization estimate, contribution in the Hpol is required (SNR > 3), as indicated by the pink line. For both cuts, a clear improvement for higher energy showers can be observed. As can be seen, most events are above trigger threshold for the full energy range, as indicated by the blue curve. High energy events result in very large amplitude signal for nearby vertices and can still be detected for very far away vertices. Nearby vertices result in a larger difference in viewing angle, which for near Cherenkov cone events lowers the amplitude significantly and will therefore result in low signals in the helper strings. Hence, the reduction in analysis efficiency for lower energies.

7.1.2.2 Neutrino Zenith Dependence

Furthermore, the analysis efficiency is dependent on the incoming zenith direction of the neutrino. Figure 7.2 left shows the efficiency of one Vpol with a signal of SNR > 2 besides the phased array and the helper strings, resulting in better efficiencies for more inclined showers.

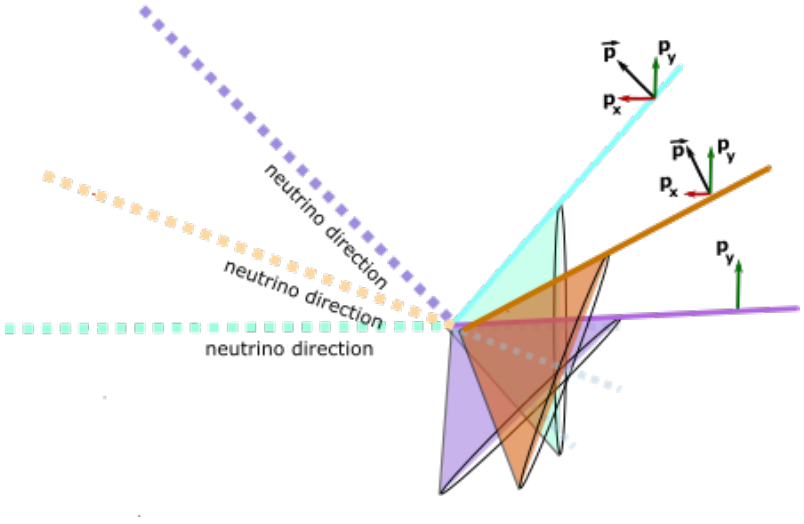

Figure 7.3: Schematic figure that shows the geometry of the shower for neutrinos arriving at different zenith directions. Indicated with the arrows are the horizontal and vertical polarization components.

The radio signature in the detector is determined by the part of the Cherenkov cone that is recorded by the detector, and hence determines if enough information is available to constrain the neutrino arrival direction. The part of the cone that is observed at the detector, highly depends on the interaction vertex of the neutrino and the incoming neutrino direction.

Figure 7.3 shows a schematic of the geometry of the interacting neutrino, the resulting Cherenkov cone and the signal propagating through the ice for three different inclinations of the neutrino direction. Due to the large Cherenkov angle, very vertical showers will not be observed by RNO-G, because the radio signal will propagate beneath the radio antennas and will not be observed. For less vertical showers (purple geometry), only the upper part of the cone will be detected, increasing the part of the cone that might be visible by an RNO-G station for less inclined showers (orange and green geometry). In other words, for more inclined showers, a larger variety of signal launch directions results in a detectable signal at the detector. This is visible in figure 7.4 left, which shows the launch direction of the radio signal with respect to the neutrino arrival zenith. The distribution of launch angles for more inclined showers shifts towards smaller launch angles and is broader than for more vertical showers. Furthermore, the small distribution of launch angles for very declined showers ($\approx$ 50°) results in roughly horizontal arriving signals, which often results in one helper string not seeing signal due to the refraction in the ice and therefore these events miss the analysis cut.

For inclined showers not only the top part of the cone might be visible, but a larger range of the upper part of the cone, resulting in a larger spread of the possible polarization angles observed at the detector. This is shown in figure 7.4 right and results in a zenith dependent point spread function. Figure 7.5 shows the reconstruction of the multiple neutrino events with the same direction (azimuth = 20° and zenith is 50° (left) and 70° (right)). The larger spread for 70° is due to the larger spread in possible polarization angles compared to 50°. The cross-like shape is because of the larger probability of an event seen at the side of Cherenkov cone than on top.

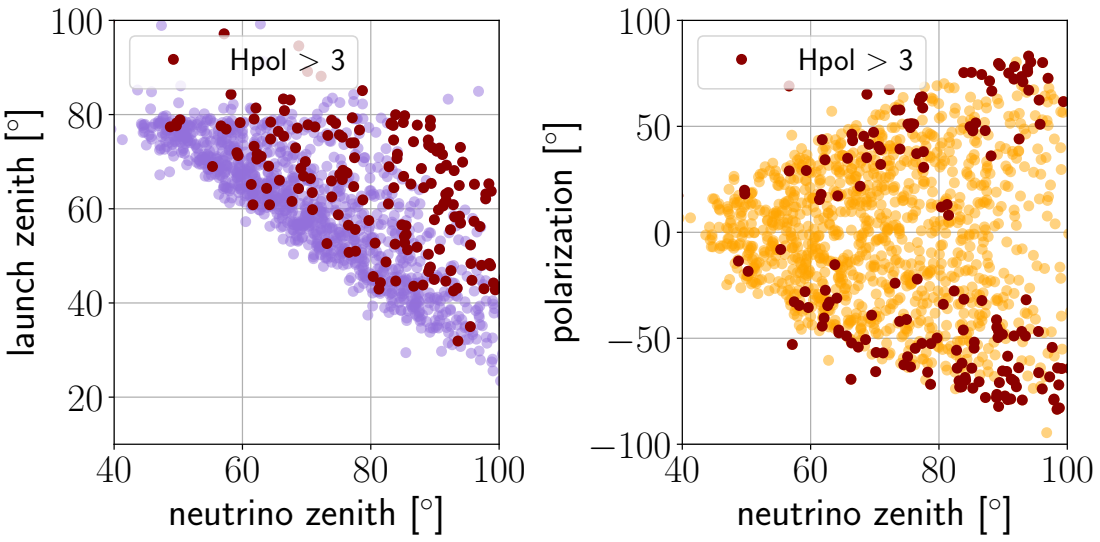

Figure 7.4: Left: Relation between the launch direction of the signal and the neutrino zenith direction. Right: Relation between the polarization angle and the neutrino zenith direction. Indicated in red are the events which have an Hpol contribution of SNR > 3.

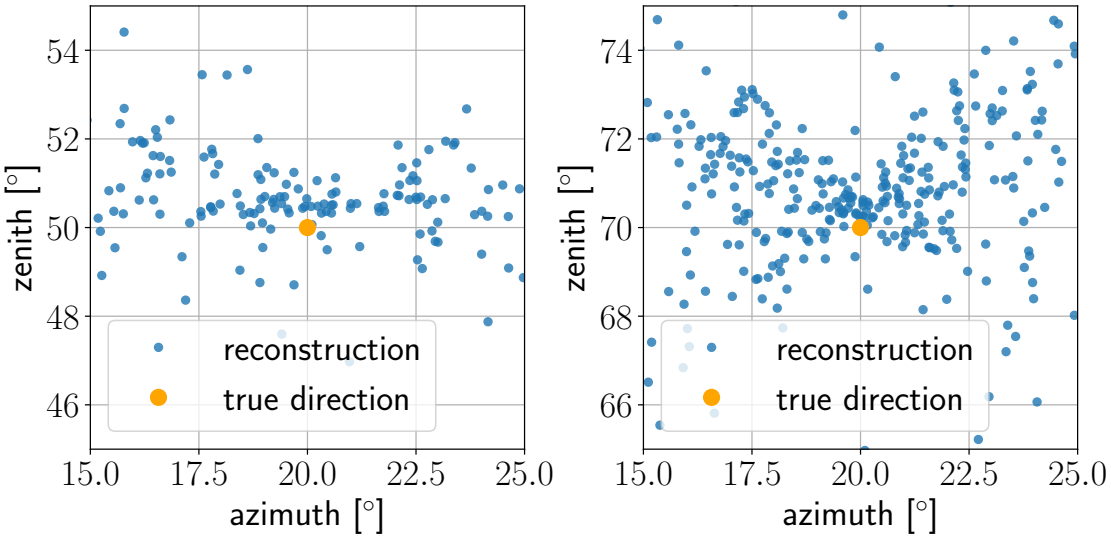

Figure 7.5: Spread in the reconstruction of the neutrino direction for neutrino events with zenith angle of 50° (left) and 70° (right).

Furthermore, as indicated in figure 7.3 with the arrows, the polarization pointing inwards to the shower axis results in polarization with a larger horizontal component for more inclined showers. The polarization is more horizontally polarized for very vertical showers, which due to the geometry miss a change to trigger the detector. For more inclined showers ($\approx$ 50°), the signal only contains vertically polarized electric field, and increasing in horizontal polarized electric field for even more steep showers.

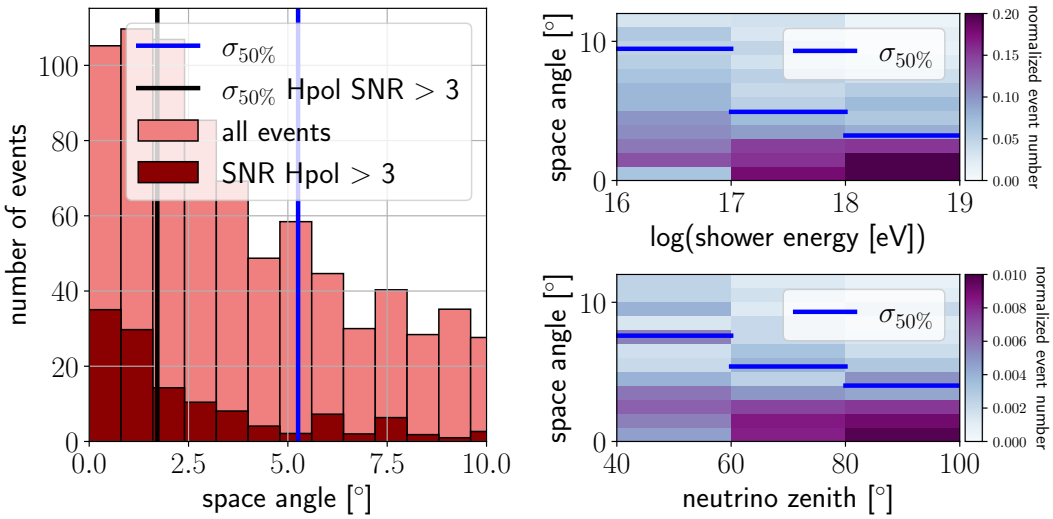

Figure 7.6: Angular resolution for the full hadronic event set. Left: Space angle. In red events that have an SNR in the Hpol > 3 are indicated. Right: Zenith (top) and shower energy (bottom) dependence of the angular resolution.

7.2 Angular Resolution

Making use of the analysis cuts of section 7.1.2, and using the reconstruction outlined in chapter 5, the angular resolution of RNO-G can be established. This section shows the results for the angular difference between the reconstructed and the true value (space angle) that can be obtained for RNO-G, as a measure for the angular resolution, as well as the zenith and energy dependence of the space angle. The reconstruction is perfomed using the *Alvarez2009* model (section 6.3.7) and uses the phased array, the near-by Hpols and all pulses in the antennas with SNR > 3.5.

7.2.1 Full Hadronic Event Set

The median space angle, as shown in figure 7.6 left, for the full event set is $\sigma_{50\%} = 5.4^\circ$, which can be interpeted such that 50% of the events can be reconstructed within 5.4°. Indicated in the same figure is the subset of events with a contribution of SNR > 3 in an Hpol, which show an increase in performance to $\sigma_{50\%} = 1.8^\circ$ and contains 5% of the events.

As shown in figure 7.6, the angular resolution shows a clear increase for more inclined showers (bottom right) and higher energy showers (upper right), which coincides with the zenith and energy dependent SNR distribution as shown in figure 7.2. Since higher energy showers correspond to higher SNR events, they naturally result in a better viewing angle resolution.

7.2.2 Quality Cuts

Applying the analysis cuts as given in figure 7.2 improves the quality of the event set and reduces the event set to 54.1%. The $\sigma_{50\%}$ of the space angle reduces to 2.4° and for events with an Hpol contribution of SNR > 3 to $\sigma_{50\%} = 1.3^\circ$, as shown in figure 7.7 right. The resolutions for the neutrino direction as shown in figure 7.7 are both symmetric for the zenith

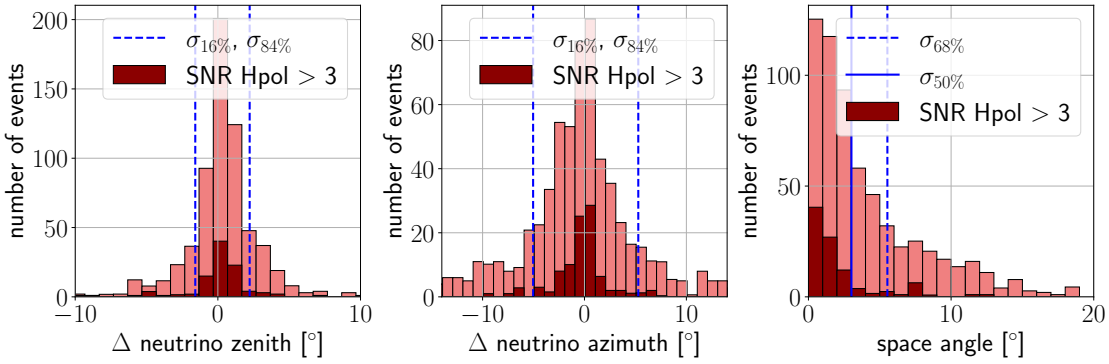

Figure 7.7: Resolutions for zenith (left), azimuth (middle) and space angle (right) for the applied qualitity cuts.

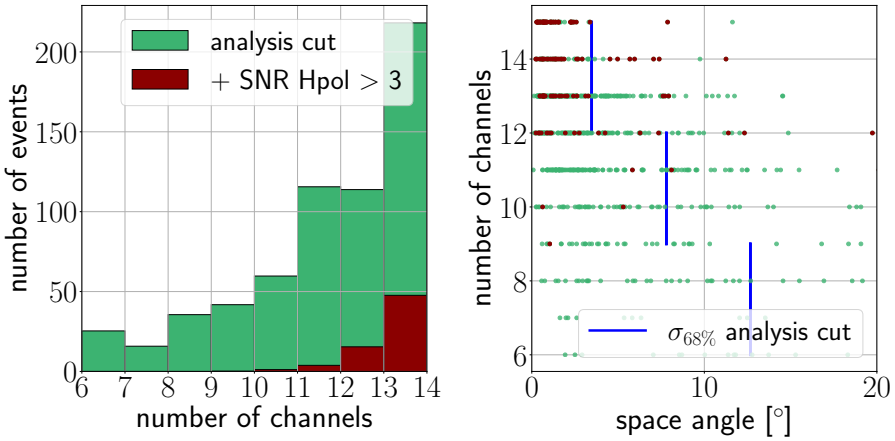

Figure 7.8: Left: Distribution of the number of antennas that is used in the reconstruction. Note that the minimum number is 6, which are the phased array antennas and the nearby Hpols. Right: Dependence of the space angle and the number of antennas used in the reconstruction. A clear improvement is seen for a larger number of antennas.

(left) and azimuth (middle) distribution. Because the polarization contributes most to the uncertainty, and because mostly the upper part of the cone is seen, the geometry results in a wider distribution for azimuth than for zenith.

Furthermore, the space angle clearly improves with the number of antennas that have a pulse (SNR $>$ 3.5) and therefore are included in the fit, as visualized in figure 7.8 right. Note that the lowest number of antennas is 6, since the phased array and the near-by Hpols are always part of the fitting procedure. Especially the vertical spacing of different antennas results in a large difference of viewing angle, which constrains the neutrino arrival direction significantly even without Hpol contribution. Therefore, the events that have signals also in the higher up antennas (-60, -40 m), which corresponds to a large number of antennas, have a better angular resolution. Shown in figure 7.8 left is that most events with a large Hpol contribution correspond to events where most antennas have a large signal.

For the hadronic events with analysis cut, a shower energy resolution of $\log(\frac{E_{\text{rec}}}{E_{\text{sim}}})$ = 14% is obtained. Results for the energy resolution are shown appendix E. Also, results for viewing angle, polarization and the signal arrival direction for the event set with analysis cuts are given in appendix E, as well as the results for the reconstruction with the *ARZ*-templates.

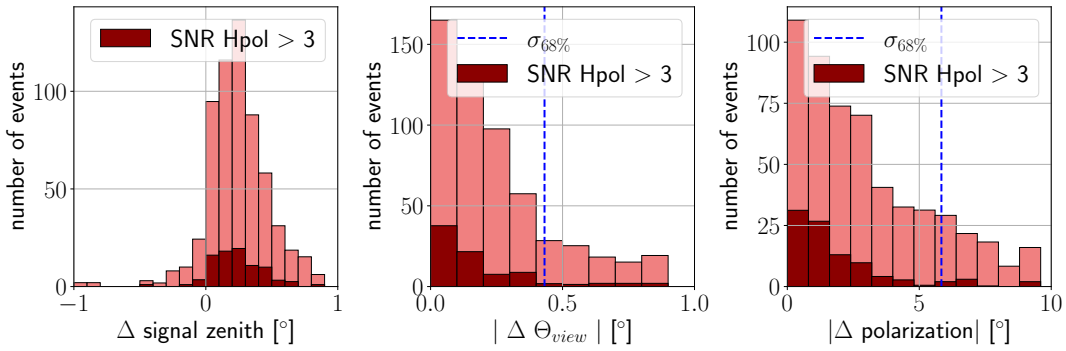

Figure 7.9: Resolutions for the signal zenith direction (left), the viewing angle (middle) and the polarization (right) for the applied quality cuts.

7.3 Sky Area Estimates

Besides the space angle, the sky area, which indicates the region to which the neutrino direction is reconstructed in square degrees, is an important measure for the angular resolution. Furthermore, indicating a sky area for a detected neutrino event, the size as well as shape, is important for follow-up programs. Figure 7.9 shows the resolutions for the signal arrival direction, viewing angle and polarization for the default analysis for which the space angle is shown in figure 7.7, i.e. quality cuts as described in 7.1.2 and an assumed flux as described in 7.1.1. As can be seen, the main uncertainty of the angular resolution comes from the polarization, and therefore the uncertainty areas are expected to be long narrow bands on the sky.

7.3.1 True Sky Area

The shape of the sky area is studied using the minimization landscape for individual events, i.e. the minimiziation value L for zenith and azimuth aroud the reconstructed value are determined for the energy that minimizes the test statistic. An example is given in figure 7.10 left, where the true value (orange dot) and the reconstructed value (light blue dot) are indicated. Seen in the figure is that the space angle is very small. The example event has a contribution in the Hpol of SNR > 3. The contour such that the minimization value is lower than the test statistic at the true value is given in orange, i.e. $L < L_{\text{sim}}$ such that it indicates the true sky area. For this event, this contour contains an area of 2.96 deg^2. Seen is that the contour results in a stretched ellipse-shaped area.

Figure 7.11 left shows the distribution of the true sky area for the default analysis. The sky area for 65% of the events can be reconstructed within 10 deg^2. For the subset of high quality events (SNR Hpol > 3) a clear improvement is seen, i.e. 60% of the events has a sky area below 2.5 deg^2.

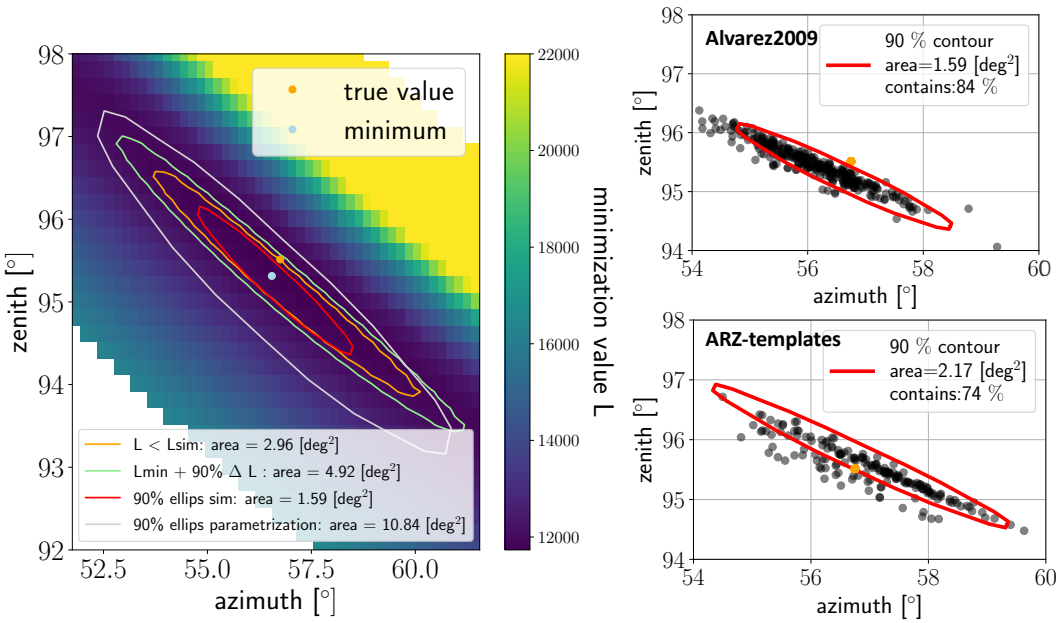

Figure 7.10: Left: Minimization landscape for an example neutrino event. The event has an Hpol contribution of SNR > 3. Indicated are the true direction (orange dot), and the direction corresponding to the minimum χ^2-value (blue dot). Furthermore, various uncertainty contours are given. The orange line indicates the area such that $L < L_{\text{sim}}$, i.e. the area that is more likely to be reconstructed as the direction than the true value. The red ellipse show the ellipse-shaped contour according the Gaussian assumption of the resolution of the viewing angle and polarization due to the true distribution of this event with varying noise. The white ellipse shows the same contour, but uses a parametrization for the resolutions due to an event classification. These ellipses give the estimated area such that 90% of the events are reconstructed within this contour. Right: Same example event (energy and direction) as the left plot, simulated multiple times and reconstucted with the *Alvarez2009* model (top) and the *ARZ*-templates (bottom). Indicated in red are the ellipses due to the true distribution of the polarization and viewing angle resolution.

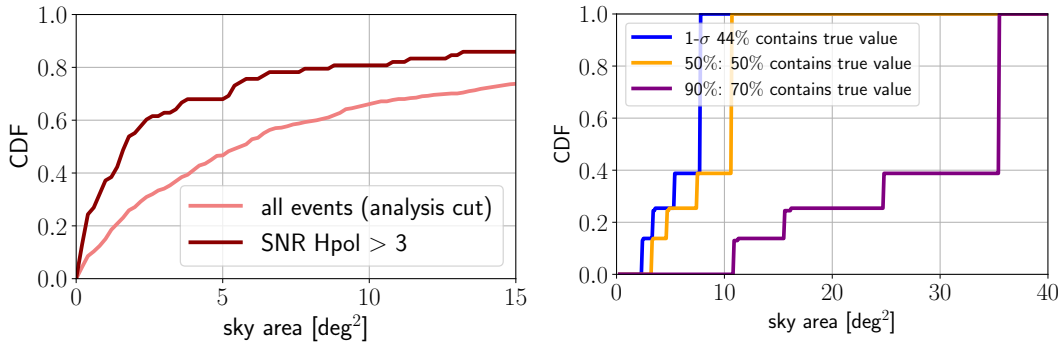

Figure 7.11: Cumulative distribution function for the sky area for the default analysis (7.2.2). Left: The true sky area, i.e. the area such that minimization value is lower than the simulated value. In dark red the subgroup of events are indicated with large contribution in the Hpol. Right: The sky area as obtained from parametrized distributions for the viewing angle and polarization resolution.

7.3.2 Sky Area Estimate for Containing the True Value

To estimate the sky area for a reconstructed neutrino event, the minimization landscape can be recalibrated by comparing the minization value of true values compared to the reconstructed values. This is done by estimating the area of the contour such that $L = L_{\text{rec}} + \Delta L$, with that ΔL the x%-containment of the $L_{\text{sim}} - L_{\text{rec}}$ distribution. This area is then defined such that x% of the contours contain the true value. Because of an imperfect noise model, and because of the correlated nature of the thermal noise, contours describing the statistical fluctuations cannot be determined using Wilk's theorem, i.e. $L_{\text{sim}} - L = 2.3$ for 1-σ contours [151]. A discussion is given in appendix G, as well as the verification of the method of recalibrating the landscape using the $L_{\text{sim}} - L$ distribution. This method allow for contours that are event specific, since they are determined by the shape of the minimization landscape of the event. Furthermore, it is computational expensive and relies on the reconstruction method to be unbiased. The $L_{\text{sim}} - L_{\text{rec}}$ distribution for the default analysis is shown in the appendix and shows no obvious dependencies on the event type.

Figure 7.10 left shows in light green the contour such that 90% of the contour contains the true value for the example event. The contour results in a sky area such that 4.92 deg^2.

7.3.3 Sky Area Estimate for Containing the Reconstructed Spread

For a less time-consuming method, and to also work when individual events show a small bias in the reconstruction, we parametrize the spread in the reconstructions due to statistical fluctuations. Following the results from the previous methods, we describe the sky area with an ellipse.

The area that is covered by these events for an example event is shown in figure 7.10 right, where the same event (with SNR Hpol > 3) with different noise realizations is reconstructed with *ARZ*-templates (bottom) and *Alvarez2009* (top). For the small polarization resolution of $\approx 5.7^\circ$ ($\sigma_{68\%}$ for the default analysis) the spread can be assumed to be not curved. To describe this region, an uncorrelated 2D Gaussian distribution is chosen, since most of the spread comes from the polarization and the viewing angle. This results in an ellipse-shape

Distribution	Parametrization		fraction
μ_{view}	0	all events (analysis cuts)	100 %
σ_{view}	0.43	all events (analysis cuts)	100 %
	0.3	SNR Vpol > 5	45 %
μ_{pol}	0	all events (analysis cuts)	100 %
σ_{pol}	5.7	all events (analysis cuts)	100 %
	5	n_{ch} = 12, 13 and SNR Hpol < 3	34 %
	2.3	SNR Hpol > 3	24 %

Table 7.2: Parametrizations for the uncertainty distributions for the viewing angle and the polarization for different event classes. The viewing angle resolution as well as the polarization resolution are parametrized using a Gaussian assumption with mean μ_{i} and standard deviation σ_{i}.

for the region of equal probability, where length and width are determined by the polarization and viewing angle respectively. These contours are given in figure 7.10 in red, which is a 2D Gaussian, based on describing the true distribution of the uncertainty of the polarization (σ_{pol} and μ_{pol}) and viewing angle (σ_{view} and μ_{view}) with an 1D Gaussian. Consequently, the contour is determined by an ellipse with radii $2.145 \cdot \sigma_{\text{view}}$ and $2.145 \cdot \sigma_{\text{pol}}$ such that 90% of the distribution is contained [152]. As shown in the figure, describing the spread of the reconstruction with a 2D Gaussian contains 84% for *Alvarez2009* reconstructions and 74% for *ARZ* reconstructions. This ellipse is also shown in red on the minimization landscape of a single event in 7.10 left, resulting in a covered area of 1.59 deg^2. The contour describes the estimated region such that 90% of the reconstructions lies within this contour, and does for this event not include the true value, as seen in the figure.

For the full event set, the distributions of figure 7.9 are used to determine the distribution of the resolution for the viewing angle and polarization, resulting in a Gaussian with $\sigma = 0.43^\circ$ and $\sigma = 5.7^\circ$ respectively, as indicated as the 68%-quantile in the figure. This results in a sky area of 35 deg^2 for the 90%-contour. Events with better sky area can be identified by selecting events that have a significant contribution in the Hpol (SNR > 3) since the polarization resolution can be described by a Gaussian with $\sigma = 2.5^\circ$. Furthermore, the viewing angle resolution improves with the signal amplitude in the Vpol (appendix B) and the polarization improves dependent on the number of antennas included in the fit (figure 7.8 right). The different event groups and the resulting parametrizations of the distributions are shown in table 7.2. The resulting area for the example event shown in figure 7.10 is indicated in the figure with the white contour and results in a larger estimate than the true distribution, in a sky area of 10.8 deg^2. Figure 7.12 illustrates the sky area that is obtained for different event groups, i.e. the full event set (blue) and two sub groups with the smallest resulting sky area. Both groups include a large signal amplitude in the Vpol, for which green includes a large Hpol contribution and red with a large number of antennas. Although the groups exclude each other, they have a very similar performance of 10.8 deg^2 and 11.2 deg^2 for the 90%-contour. The distribution for the full event set is shown in figure 7.11 right as a CDF.

The obtained sky area makes RNO-G suitable for follow-up programmes. For the high quality events optical and X-ray telescopes can search the region in the sky the neutrino is pointed to for radiation. Even for events with a larger sky area, optical telescopes like ZTF can be used for follow-ups due to their large FoV of 47 deg^2 [153].

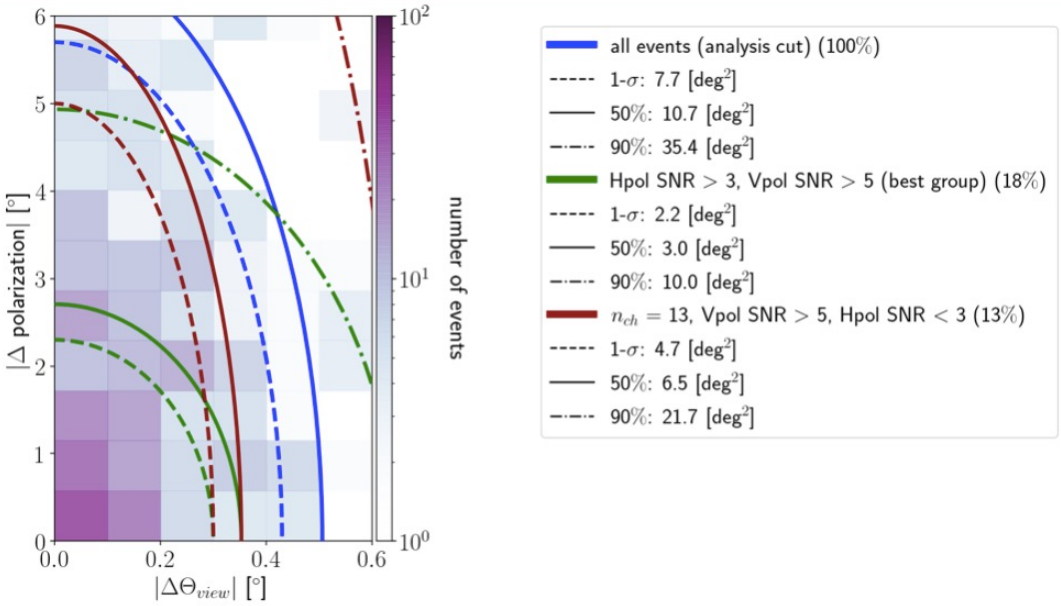

Figure 7.12: Distribution of the polarization and viewing angle resolution, i.e. 2D histogram of figure 7.9 middle and right. Note different scales of the x, y axes (10:1). The contours show parts of the ellipses as obtained by describing the resolution of the viewing angle and polarziation as uncorrelated Gaussian distributions. Blue indicates the contours for the full event set, i.e. the distributions shown in figure 7.9 middle and right. Green and red each show the two sub groups of events that result in the smallest sky area. The different linestyles indicate the 1-σ, 50% and 90%-contour.

7.4 Implication for Steady Point Sources

As a measure for the performance of RNO-G to identify individual sources as neutrino producers the *discovery potential* is studied. The discovery potential is the signal strength required such that a 5-σ discovery can be claimed in 50% of the experiments, i.e. it is a measure for identifying the obtained signal from the point source considering the background events. Results of this section were created with the software framework `toise` [154] and are obtained in cooperation with Steffen Hallmann. `toise` is a framework to quantify the science performance of neutrino detectors parametrizing the performance quantities of the detector, like the effective area, analysis efficiencies, angular resolution and energy resolution. The discovery potential is evaluated by placing a point source at a specific zenith bin, assuming a point spread function and isotropic background corresponding to the specific zenith bin and using a circular region around the pointsource to obtain the number of signal and background events. The angular distribution obtained as shown in figure 7.6 is used in `toise` to study the effect on the discovery potential for RNO-G.

A steady point source with an E^{-2} spectrum is studied as the model source. A good localization of the neutrino events results in a reduced number of background events for the source region. Therefore, an improved angular resolution improves the discovery potential. For the neutrino background, the diffuse astrophysical background and neutrinos created by the GZK-effect are considered. As currently the level of the diffuse UHE neutrino flux is unknown, the cosmogenic neutrino background from [150] is used and the extrapolation of the measured diffuse astrophysical neutrino flux from [149], similar as described in section 7.1.1.

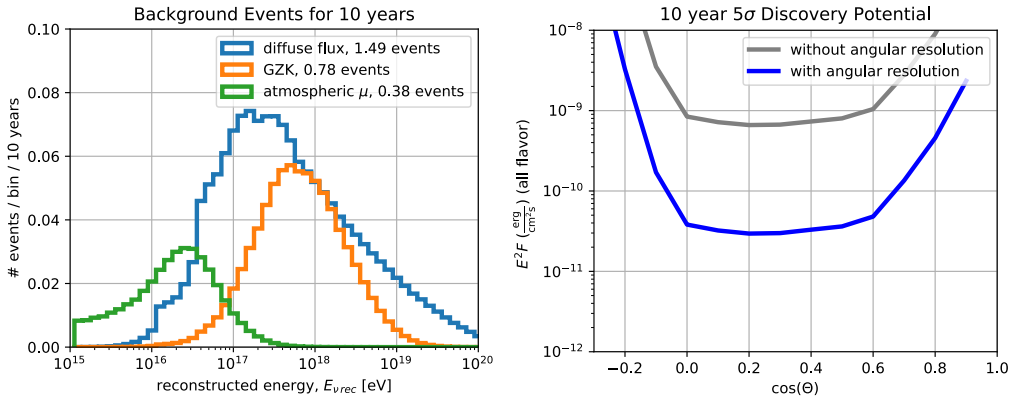

Figure 7.13: Left: Expected number of events for the complete RNO-G array (35 stations) for a 10 year livetime. Included are atmospheric muons (green), cosmogenic neutrinos (orange) and astrophysical neutrinos (blue). Right: All flavor discovery potential for a livetime of 10 years. The blue line shows the discovery potential including the obtained angular resolution.

Besides the neutrino background, muons created in cosmic-ray air showers that can interact in the ice are included. The muon background is studied in [89] to be approximately 0.3 events per year for a 100 station deep (100 meter) phased array trigger, and is shown to have large systematic uncertainties due to the variations in cosmic-ray mass composition and hadronic interaction models ($\approx$ factor 6) and to be highly dependent on the trigger ($\approx$ factor 10 larger for a single dipole trigger compared to a PA). As a proxy for the muon background, the zenith and energy dependent distribution for triggered events for IceCube-Gen2 Radio simulations for a deep phased array trigger (200 meter) are used. Assumed is that no distinction can be made between muons and neutrinos, i.e. the RNO-G surface stations are not used as a veto for muon events by detecting cosmic-ray air showers. By including the full muon background the obtained results are conservative.

The expected number of triggered events for RNO-G for a livetime of 10 years are shown in figure 7.13 left. The total expected number of events is 6.6, with the largest contribution coming from the diffuse astrophysical neutrino flux.

The event rates for the point source signal and the backgrounds as shown in figure 7.13 left, are used in an Asimov approach to obtain the discovery potential [155] . The discovery potential is $\approx 2 \cdot 10^{-10} \frac{\text{erg}}{\text{cm}^2\text{s}}$ for the angular resolution obtained in this work (blue line) and shows to be very flat in the regime where RNO-G is most sensitive. Without angular resolution the point source fluence required for a discovery increases by more than a factor 10 (grey line).

The differential point source discovery potential of RNO-G is given in figure 7.14, together with the total discovery potential for a zenith of 70°. The expected fluence for the long duration transient of 10 stacked 6 month lasting blazars, as taken from [86] and inferred from [159], is within the reach of the RNO-G discovery potential. Other sources shown in the plot are shorter time-scale transients, and therefore shown results are conservative.

The current implementation in the `toise` framework assumes a 1D distribution of the point spread function. For RNO-G, the point spread function shows to have a cross-shape due

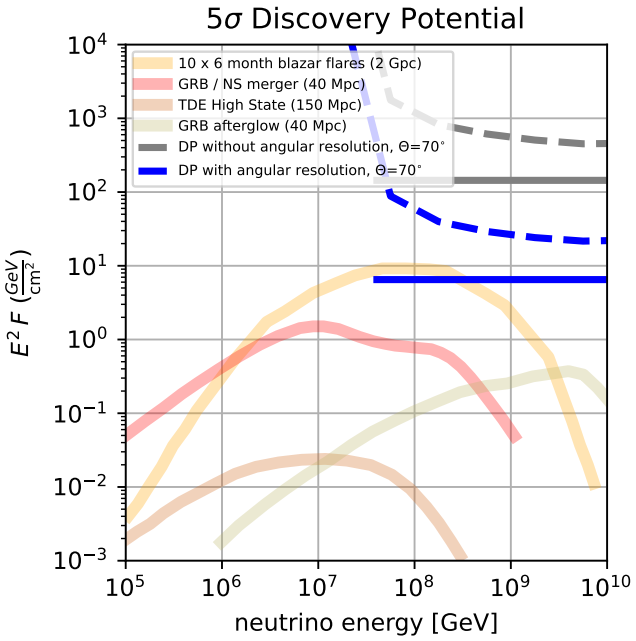

Figure 7.14: The RNO-G point source discovery potential and expected neutrino fluences for a variety of neutrino source candidates. The dashed lines show the discovery potential for full decade energy bins and the solid line the integrated discovery potential. The integrated discovery potential is shown in the energy range where 95% of the events are expected. The calculated fluences are obtained from [86] and are inferred from [156] for the TDE, [157] for the GRB afterglow, [158] for the neutron star merger and [159] for the blazars.

to the limited range of polarization angles allowed due to the geometry, like shown in figure 7.5. For further optimizations, the cross-shape can be included which will reduce the number of background events in the source region. Therefore, the results for the discovery potential as shown in this section are conservative.

7.5 Coincidence Events

Some neutrino events will be detected by multiple RNO-G stations, and due to the large spacing between the stations the angular resolution of these events can be further limited. While studying the full capacitcy of coincidence events of RNO-G is outside the scope of the work, in this section a proof-of-concept is given for the reconstruction for deep-deep coincindences and the consequences for deep-shallow coincidences are given.

7.5.1 Deep-Deep Coincidence

The RNO-G spacing of 1.25 km is such that most events will be seen by a single station, and therefore each station is equiped such that reconstruction of the neutrino event is possible. However, a fraction of the events will be seen by multiple stations due to the several sub-showers corresponding to a single neutrino. While tau neutrinos can result in a *double bang*, muons created due to the interaction of muon neutrinos can generate several showers due to stochastic energy losses. The individual reconstructions of the sub-showers can be combined in order to improve resolution of the direction, since the sub-showers have the

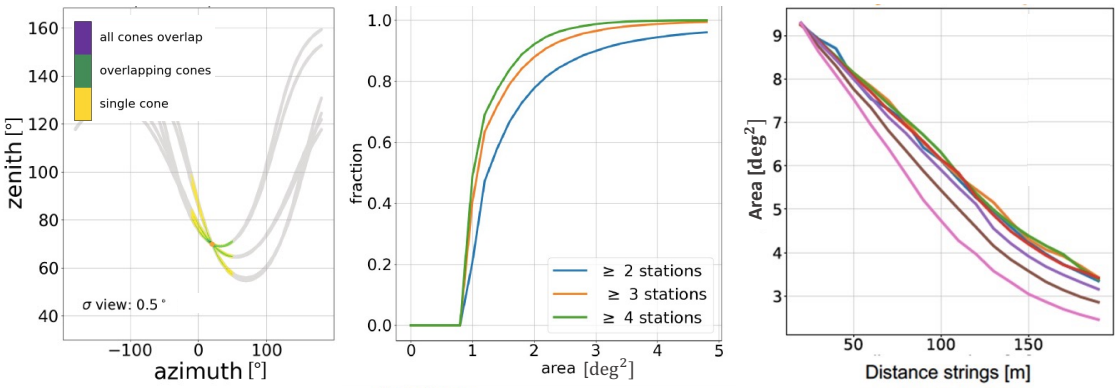

Figure 7.15: Left: Geometry plot for the overlap of the allowed regions for the neutrino directions due to the viewing angle for an event seen by three stations. The curves nicely intersect at a single point, i.e. the neutrino direction. Middle: The area for the allowed neutrino direction for events seen by multiple stations using a IceCube-Gen2 Radio simulation set. A single viewing angle resolution with a resolution of 0.5° per detected station. Right: Effect of the string spacing on the area that indicates the possible region for the neutrino direction. The various colors indicate different directions of the vertex position.

same direction.

Dependent on the geometry and characteristics of the event, even single showers can be detected by multiple surrounding stations. In these cases, the shower can be reconstructed combining all triggered stations, and therefore increasing the resolution of direction of the event. Due to the large spacing of the stations, both stations see a different part of the cone, and therefore the position on the Cherenkov cone can be identified even without the use of polarization. Figure 7.15 left shows the geometry of an event seen by three stations using a single antenna with a direct and a reflected pulse, assuming a viewing angle resolution of 0.5°, similar as in figure 6.14. Clearly seen is that, due to the different positions of the stations with respect to the vertex position, the overlap of the individual band on the sky due to individual viewing angles nicely indicates the direction of the neutrino. This method can be used to obtain the sky area to which the neutrino direction is restricted, due to the overlap of the cones. An IceCube-Gen2 Radio simulation set, using a similar flux model as described in 7.1.1, is used to give an indication of how well the neutrino direction can be restricted with the use of only the phased array (no polarization information). Figure 7.15 middle, shows that 80% of the single shower coincidence events can be reconstructed to a space angle of 2°.

The direction reconstruction method discussed in chapter 5 is adapted to reconstruct a shower that triggered two stations. While a full study of the reconstruction capability of coincidence events is not part of this work, an example event is used to show the proof-of-concept. An event is chosen with zenith 65.3° and azimuth 243.2°, shown in figure 7.16. This same event is reconstructed multiple times with different noise realizations to show the spread in reconstruction. For the reconstruction only the triggered pulse using the full phased array is included in the fit. Therefore, using a single station, no polarization information will be included. Figure 7.16 left, shows the spread of the neutrino arrival direction for the two stations individually. As can be seen, each station result in a ring of possible neutrino directions. For the station indicated in red, the side of the Cherenkov cone is not always good obtained, resulting in a double-band structure. While the neutrino direction can be obtained by overlaying the two independent stations, an improvement should be

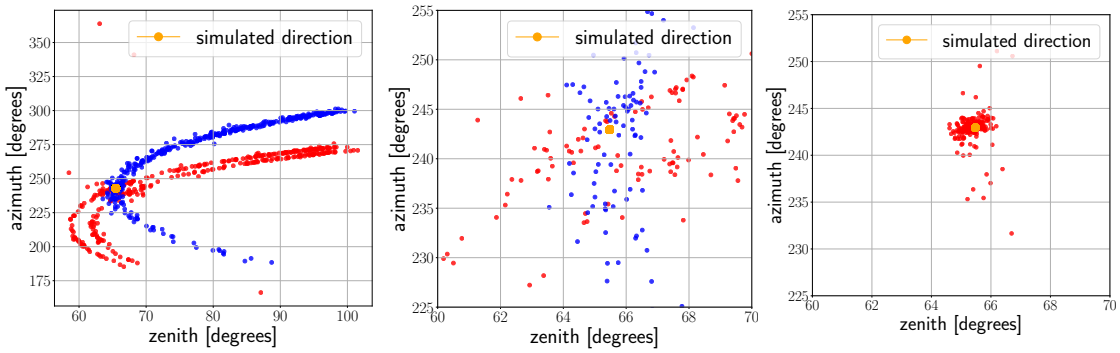

Figure 7.16: The neutrino direction reconstruction applied to an event that triggered two stations. Left: The reconstruction for the two stations seperately. Middle: Zoom-in of the left figure. Right: Combining the two stations in a single reconstruction.

obtained by fitting both stations simultaneously. The rings nicely overlap at the position of the true neutrino direction. Figures 7.16 right shows the spread in neutrino arrival direction when combining both stations simultanious in the fit, which reduces compared to the overlap of the two stations (Middle: zoom in of left plot), which reduces to $\sigma_{68\%} = 0.36^\circ$ for zenith and $\sigma_{68\%} = 0.66^\circ$ for azimuth.

For including both stations simultaneous in the fit, the timing resolution between stations does not need to be as good as for the timing of a single station. As long as the two triggered stations can be assigned to the same shower, both stations can be combined in the same fit.

7.5.2 Deep-Shallow Coincidence

For the surface station 15% of the events for $10^{17.5}$ eV neutrinos (largest sensitivy) will have a 2-σ pulse in one of the down pointing LPDAs of the surface component, as shown in figure 11 of [17]. While obtaining a pulse in one of the surface antennas often indicates that the Vpols at the power string (60 and 40 m) also see a pulse, which results already in a space angle of 4° (figure 7.8 right), the long baseline between the LPDAs and the phased array results in a large difference in viewing angle which reduces the space angle even more. [139] has shown that, using a similar reconstructed method as in this work, that 68% of all events triggered by the ARIANNA surface component can be reconstructed to a space angle within 3°.

7.6 Implication for In-Ice Radio Neutrino Detectors

The specifics of the performance of the reconstruction outlined in chapter 6 mainly depend on the quality and characteristics of the event set. The quality of the event set is predominatly determined by the detection volume (i.e. the specifics of the ice) and the trigger, and the specifics of the radio signatures depends on the station design. This means, that the performance of this reconstruction for other radio neutrino experiments depends on the ice sheet, moreover its attenuation length and the depth of the firn. As of now, no effort is been put in optimizing the reconstruction for different locations (i.e. South Pole) and station de-

signs (i.e. depth string and antenna spacing and depth).

First of all, the depth of the station is important, as it is optimal to have the reconstruction anntenas in the deep ice, below the firn. While the vertex reconstruction requires signal in an antenna vertically spaced from the phased array (the -80 m antenna in the RNO-G case), the vertically displaced antennas also result in pulses with large viewing angle differences which improves the angular resolution (as shown in figure **??** and is discussed in section 7.2.1. Therefore, not only the phased array is recommended to be below the firn, but also the reconstruction antennas on the power string, such that they won't be in the shadow zone. For RNO-G, the firn is 70 meters, and for South Pole (IceCube-Gen2 Radio) roughly 150 meters.

Secondly, the attenuation of the ice influences the amplitude of the signals once they reach the detector. The attenuation length at South Pole is larger than the ice-sheet of Summit. This results in larger amplitude events for the same distance. Since a larger attenuation length also increases the covered volume, the fraction of events above trigger threshold with respect to the total number of events will slightly be reduced. Therefore, the quality cuts used in this chapter will be more harsh for the South Pole ice. Also, a smaller attenuation length results in more close-by vertices, which gives a larger differences in viewing angle for vertically spaced antennas.

For the RNO-G design, a horizontal spacing of the strings is chosen such that they can be used for the reconstruction of the azimuthal direction of the signal. For larger horizontal spacings, the difference in detected viewing angle and, especially, different signal arrival directions, can give a better constrain on the angular resolution. For horizontal spacing, the change in viewing angle is smaller compared to the vertical spacing. Moreover, horizontally spacing is not impacted by the ray bending as holds for the vertical spacing. This way, horizontally spaced antennas can each detect a different part of the Cherenkov cone, and therefore no polarization is needed for the reconstruction, very similar to the coincidence events, described in section 7.5. While no full simulations were performed to study this effect, the impact of these string spacings is indicated by a geometry study. The on-sky area for the neutrino location was determined purely based on geometry using an neutrino event of 70° and 20° azimuth and an uncertainty of 0.5° in viewing angle. The area that constrains the neutrino direction due to a single Vpol at each string is calculated and shown in figure 7.15 right. A variety of vertex zeniths is chosen for a vertex distance of 2500 meters. Clearly shown is the improving angular resolution for increasing string distances.

Chapter 8
Conclusion and Outlook

Taku niaq tugut.
— *Greelandic for* See you soon

This thesis has outlined (chapter 5) the first methodology for direction reconstruction for deep in-ice radio neutrino detectors using the entire station, which is the main focus of this work. Presented is a forward folding technique in which an analytic description of the electric field is used, in order to combine all antennas in the station for reconstruction of the neutrino properties Θ, ϕ, E_{sh}. Therefore, this method can constrain the neutrino direction more than the intuitive approach of an individual measure of the viewing angle, polarization and the signal direction. Also, waveforms in multiple antennas are combined in the minimization approach, which exploits the effect of noise reduction.

The methodoloy is applied to an RNO-G deep station and the angular resolution for RNO-G is established (chapter 7). We showed that the angular resolution of a neutrino event highly depends on the signature of the radio emission in the station, i.e. the amplitude of the signal, the variety of ray types, and therefore, viewing angles that leave a noticable pulse in the station. Therefore, the impact of the neutrino zenith as well as the neutrino energy on the angular resolution are studied. An improved angular resolution for inclined showers as well as higher energies is obtained. The angular resolution for high quality events (50%) is studied to be $\sigma_{68\%} = 5.5^\circ$, i.e. 68% of the events (assuming an IceCube extension and GZK model) are expected to be reconstructed within 5.5°. Furthermore, the sub-categorie of events for which the electric field is significantly horizontally polarized such that signal is seen in the low sensitive Hpol antennas, has studied to have an angular resolution of $\sigma_{68\%} = 2.5^\circ$.

The neutrino direction reconstruction performance of an in-ice radio neutrino detector depends on the analysis cuts as well as the angular resolution. The framework of the presented methodology can easily be applied for different station designs and for other ice volumes, e.g. South Pole ice. Therefore, the angular resolution of other experiments can be obtained using the presented framework. Also station designs, i.e. string and antenna spacing, can be optimized as well as their optimum depth in the ice to minimize the angular resolution of the experiment. A large improvement for the angular resolution is given by signal in a large vertical range, which results in larger constrains on the polarization of the electric field, due to the difference in viewing angle of the signals arriving, and is hence an important factor for the angular resolution. Since difference in viewing angle can also results in a lower amplitude, and vertical spacing can re-

sult in raybending, the performance of the angular resolution is very much dependend on the antenna spacing, the depth of the station and the ice (density profile (raybending) as well as attenuation (event set, far away vertices)). This emphasizes the importance of a full Monte Carlo study for angular resolution performance and for station design optimization, for which the presented methodology can be used as a framework.

Furthermore, the effect is shown of using a realistic signal model (*ARZ2020*) for the electric fields of neutrino induced particle shower, and therefore the impact of small deviations in the shower profiles. No further optimizations were studied to improve the signal model, which is highly encouraged for future work. Also, for further analysis to study the angular resolution of in-ice radio detectors, the usage of the *ARZ2020* model is highly recommended.

Finally, the angular resolution for neutrino events for which the radio emission triggers multiple stations is expected to be improved significantly, such a good polarization reconstruction can be established without the usage of Hpol antennas. Promising first results with the outlined method are given in section 7.5. Further work will include studying the full capability of RNO-G coincidence events.

In the summer of 2022, 7 more stations will be deployed as part of the RNO-G array, and 35 stations will be reached in 2025. Furthermore, the radio detection technique will play a significant role in IceCube-Gen2 with the construction of 200 planned stations beginning in 2027. Hopefully, the optical extension will change the neutrino astronomy field to one in which 5-σ neutrino sources become routine. RNO-G and IceCube-Gen2 Radio, will lay the groundwork for detection, identification and pointing of neutrinos from either astrophysical or cosmogenic nature, thereby opening the field for higher energy neutrino astronomy. Hereby, only life will teach us if this thesis ends with an too optimistic note: Dear in-ice interacted neutrino detected with the radio technique, *Taku niaq tugut!*

Bibliography

[1] C. L. Cowan, F. Reines et al., *Detection of the Free Neutrino: a Confirmation*, *Science* **124** (1956) 103.

[2] E. Fermi, *Tentativo di una Teoria Dei Raggi* , *Il Nuovo Cimento (1924-1942)* .

[3] MicroBooNE collaboration, *First Measurement of Inclusive Muon Neutrino Charged Current Differential Cross Sections on Argon at $E_\nu \sim 0.8$ GeV with the MicroBooNE Detector*, *Phys. Rev. Lett.* **123** (2019) 131801.

[4] R. Davis, D. S. Harmer et al., *Search for Neutrinos from the Sun*, *Phys. Rev. Lett.* **20** (1968) 1205.

[5] SNO collaboration, *Measurement of the Rate of $\nu_e + d \rightarrow p + p + e^-$ Interactions Produced by ^8B Solar Neutrinos at the Sudbury Neutrino Observatory*, *Phys. Rev. Lett.* **87** (2001) 071301.

[6] J. Zhang, *JUNO Oscillation Physics*, *Journal of Physics: Conference Series* **2156** (2021) 012110.

[7] Super-Kamiokande collaboration, *Review of Atmospheric Neutrino Results from Super-Kamiokande*, *PoS* **ICHEP2020** (2021) 181 [2012.06864].

[8] M. Ageron, J. Aguilar et al., *ANTARES: The first undersea neutrino telescope*, *Nuclear Instruments and Methods in Physics Research Section A: Accelerators, Spectrometers, Detectors and Associated Equipment* **656** (2011) 11.

[9] IceCube collaboration, *Measurement of Atmospheric Neutrino Oscillations at 6–56 GeV with IceCube DeepCore*, *Phys. Rev. Lett.* **120** (2018) 071801.

[10] N. Agafonova, A. Alexandrov et al., *OPERA tau neutrino charged current interactions*, *Scientific Data* **8** (2021) 218.

[11] K. Hirata, T. Kajita et al., *Observation of a neutrino burst from the supernova SN1987A*, *Phys. Rev. Lett.* **58** (1987) 1490.

[12] IceCube Collaboration, *Evidence for High-Energy Extraterrestrial Neutrinos at the IceCube Detector*, *Science* **342** (2013) 1242856.

[13] M. G. Aartsen, M. Ackermann et al., *Observation of High-Energy Astrophysical Neutrinos in Three Years of IceCube Data*, *Physical Review Letters* **113** (2014) .

[14] M. Ackermann, M. Ajello et al., *The Spectrum of Isotropic Diffuse Gamma-Ray Emission between 100 MeV and 820 GeV*, *The Astrophysical Journal* **799** (2015) 86.

[15] M. Aartsen, M. Ackermann et al., *Differential limit on the extremely-high-energy cosmic neutrino flux in the presence of astrophysical background from nine years of IceCube data*, *Physical Review D* **98** (2018) .

[16] The Pierre Auger Collaboration, A. Aab et al., *The Pierre Auger Observatory: Contributions to the 34th International Cosmic Ray Conference (ICRC 2015)*, 1509.03732.

[17] J. Aguilar, P. Allison et al., *Design and sensitivity of the Radio Neutrino Observatory in Greenland (RNO-G)*, *Journal of Instrumentation* **16** (2021) P03025.

[18] V. F. Hess, *Über Beobachtungen der durchdringenden Strahlung bei sieben Freiballonfahrten*, *Z. Phys.* **13** (1912) 1084.

[19] M. Aartsen, M. Ackermann et al., *Neutrino emission from the direction of the blazar TXS 0506+056 prior to the IceCube-170922A alert*, *Science* **361** (2018) 147–151.

[20] G. F. Krymskii, *A regular mechanism for the acceleration of charged particles on the front of a shock wave*, *Akademiia Nauk SSSR Doklady* **234** (1977) 1306.

[21] A. Aab, P. Abreu et al., *Measurement of the cosmic-ray energy spectrum above 2.5×1018eV using the Pierre Auger Observatory*, *Physical Review D* **102** (2020) .

[22] K. Greisen, *End to the Cosmic-Ray Spectrum?*, *Phys. Rev. Lett.* **16** (1966) 748.

[23] G. T. Zatsepin and V. A. Kuzmin, *Upper limit of the spectrum of cosmic rays*, *JETP Lett.* **4** (1966) 78.

[24] T. Pierog, *Review of Model Predictions for Extensive Air Showers*, *JPS Conf. Proc.* **19** (2018) 011018.

[25] M. S. Muzio, G. R. Farrar et al., *Probing the environments surrounding ultrahigh energy cosmic ray accelerators and their implications for astrophysical neutrinos*, *Phys. Rev. D* **105** (2022) 023022 [2108.05512].

[26] K. Fang, K. Kotera et al., *Testing the newborn pulsar origin of ultrahigh energy cosmic rays with EeV neutrinos*, *Physical Review D* **90** (2013) .

[27] D. Boncioli, D. Biehl et al., *On the Common Origin of Cosmic Rays across the Ankle and Diffuse Neutrinos at the Highest Energies from Low-luminosity Gamma-Ray Bursts*, *The Astrophysical Journal* **872** (2019) 110.

[28] K. Murase, *High energy neutrino early afterglows from gamma-ray bursts revisited*, *Physical Review D* **76** (2007) .

[29] X. Rodrigues, J. Heinze et al., *Active Galactic Nuclei Jets as the Origin of Ultrahigh-Energy Cosmic Rays and Perspectives for the Detection of Astrophysical Source Neutrinos at EeV Energies*, *Physical Review Letters* **126** (2021) .

[30] J. Abraham, P. Abreu et al., *Correlation of the Highest-Energy Cosmic Rays with Nearby Extragalactic Objects*, *Science (New York, N.Y.)* **318** (2007) 938.

[31] M. Ackermann, M. Ajello et al., *Resolving the Extragalactic γ-Ray Background above 50 GeV with the Fermi Large Area Telescope*, *Phys. Rev. Lett.* **116** (2016) 151105.

[32] K. Murase, Y. Inoue et al., *Diffuse neutrino intensity from the inner jets of active galactic nuclei: Impacts of external photon fields and the blazar sequence*, *Physical Review D* **90** (2014) .

[33] M. Punch, C. W. Akerlof et al., *Detection of TeV photons from the active galaxy Markarian 421*, *Nature* **358** (1992) 477.

[34] J. Quinn, C. Akerlof et al., *Detection of Gamma Rays with E > 300 GeV from Markarian 501*, *The Astrophysical Journal Letters* **456** (2009) L83.

[35] PIERRE AUGER, TELESCOPE ARRAY collaboration, *The energy spectrum of ultra-high energy cosmic rays measured at the Pierre Auger Observatory and at the Telescope Array*, *PoS* **ICRC2019** (2020) 234 [2001.08811].

[36] PIERRE AUGER collaboration, *Measurement of the Depth of Maximum of Extensive Air Showers above* 10^{18} eV, *Phys. Rev. Lett.* **104** (2010) 091101.

[37] M. Spurio, *Probes of Multimessenger Astrophysics*. Springer, 2018.

[38] M. Ahlers and F. Halzen, *Minimal cosmogenic neutrinos*, *Physical Review D* **86** (2012) .

[39] A. van Vliet, J. R. Hörandel et al., *Cosmogenic gamma-rays and neutrinos constrain UHECR source models*, *PoS* **ICRC2017** (2018) 562 [1707.04511].

[40] J. Heinze, A. Fedynitch et al., *A New View on Auger Data and Cosmogenic Neutrinos in Light of Different Nuclear Disintegration and Air-shower Models*, *The Astrophysical Journal* **873** (2019) 88.

[41] R. A. Batista, M.-S. Shin et al., *Implications of strong intergalactic magnetic fields for ultrahigh-energy cosmic-ray astronomy*, *Physical Review D* **96** (2017) .

[42] P. F. Michelson, W. B. Atwood et al., *Fermi Gamma-ray Space Telescope: high-energy results from the first year*, *Reports on Progress in Physics* **73** (2010) 074901.

[43] R. A. Ong, *Highlights from VERITAS on VHE gamma-ray sources in our Galaxy*, *Advances in Space Research* **53** (2014) 1483–1491.

[44] F. Aharonian, A. G. Akhperjanian et al., *H.E.S.S. observations of PKS 2155-304*, *Astronomy and Astrophysics* **430** (2005) 865.

[45] MAGIC collaboration, *Status and First Results of the MAGIC Telescope*, *Astrophys. Space Sci.* **297** (2005) 245 [astro-ph/0407475].

[46] CTA OBSERVATORY, CTA CONSORTIUM, LST collaboration, *CTA – the World's largest ground-based gamma-ray observatory*, *PoS* **ICRC2021** (2022) 005.

[47] HAWC collaboration, *Highlights from the HAWC Observatory*, *Nucl. Part. Phys. Proc.* **306-308** (2019) 12.

[48] LHAASO collaboration, *Highlights of LHAASO science results*, *PoS* **ICRC2021** (2022) 011.

[49] J. N. Abdurashitov, T. J. Bowles et al., *Measurement of the Solar Neutrino Capture Rate by SAGE and Implications for Neutrino Oscillations in Vacuum*, *Physical Review Letters* **83** (1999) 4686–4689.

[50] R. Coniglione, *The KM3NeT neutrino telescope*, *Journal of Physics: Conference Series* **632** (2015) 012002.

[51] M. G. Aartsen, R. Abbasi et al., *IceCube-Gen2: the window to the extreme Universe*, *Journal of Physics G: Nuclear and Particle Physics* **48** (2021) 060501.

[52] F. G. Schröder, *Status of the radio technique for cosmic-ray induced air showers*, *Nuclear and Particle Physics Proceedings* **279-281** (2016) 190.

[53] G. A. Askar'yan, *Excess negative charge of an electron-photon shower and its coherent radio emission*, *Zh. Eksp. Teor. Fiz.* **41** (1961) 616.

[54] L. Pyras, C.Welling et al., *Radio Detection of EeV Neutrinos in Dielectric Media using the Askaryan Effect*, 2022. 10.3204/PUBDB-2021-03021.

[55] P. W. Gorham, S. W. Barwick et al., *Observations of the Askaryan Effect in Ice*, *Physical Review Letters* **99** (2007) .

[56] D. Saltzberg, P. Gorham et al., *Observation of the Askaryan Effect: Coherent Microwave Cherenkov Emission from Charge Asymmetry in High-Energy Particle Cascades*, *Physical Review Letters* **86** (2001) 2802–2805.

[57] P. Schellart, S. Buitink et al., *Polarized radio emission from extensive air showers measured with LOFAR*, *Journal of Cosmology and Astroparticle Physics* **2014** (2014) 014–014.

[58] J. Jelley, W. Charman et al., *Radio pulses from extensive air showers*, *Il Nuovo Cimento A* **46** (1966) 649.

[59] H. Falcke and P. Gorham, *Detecting radio emission from cosmic ray air showers and neutrinos with a digital radio telescope*, *Astroparticle Physics* **19** (2003) 477.

[60] H. Falcke, W. Apel et al., *Detection and imaging of atmospheric radio flashes from cosmic ray air showers*, *Nature* **435** (2005) 313.

[61] D. Ardouin, A. Bellétoile et al., *Radio-detection signature of high-energy cosmic rays by the CODALEMA experiment*, *Nuclear Instruments and Methods in Physics Research Section A: Accelerators, Spectrometers, Detectors and Associated Equipment* **555** (2005) 148–163.

[62] M. P. van Haarlem, M. W. Wise et al., *LOFAR: The LOw-Frequency ARray*, *Astronomy &amp Astrophysics* **556** (2013) A2 [1305.3550].

[63] PIERRE AUGER collaboration, *The Pierre Auger Cosmic Ray Observatory*, *Nucl. Instrum. Meth. A* **798** (2015) 172 [1502.01323].

[64] R. Hiller, N. Budnev et al., *Status and First Results of Tunka-rex, an Experiment for the Radio Detection of Air Showers*, *Physics Procedia* **61** (2015) 708.

[65] A. Aab, P. Abreu et al., *Measurement of the Radiation Energy in the Radio Signal of Extensive Air Showers as a Universal Estimator of Cosmic-Ray Energy*, *Physical Review Letters* **116** (2016) .

[66] P. Schellart, S. Buitink et al., *Polarized radio emission from extensive air showers measured with LOFAR*, *Journal of Cosmology and Astroparticle Physics* **2014** (2014) 014–014.

[67] T. Huege, M. Ludwig et al., *Simulating radio emission from air showers with CoREAS*, in *AIP Conference Proceedings*, AIP, 2013, DOI.

[68] J. Alvarez-Muñiz, W. R. Carvalho et al., *Monte Carlo simulations of radio pulses in atmospheric showers using ZHAireS*, *Astroparticle Physics* **35** (2012) 325–341.

[69] K. Bechtol, K. Belov et al., *SLAC T-510 experiment for radio emission from particle showers: Detailed simulation study and interpretation*, *Physical Review D* **105** (2022) .

[70] A. Connolly, *Status of SalSA*, 1010.4347.

[71] J. Alvarez-Muñiz, E. Marqués et al., *Coherent radio pulses from showers in different media: A unified parametrization*, *Physical Review D* **74** (2006) .

[72] S. Buitink, A. Corstanje et al., *Searching for neutrino radio flashes from the Moon with LOFAR*, in *AIP Conference Proceedings*, AIP, 2013,

[73] P. W. Gorham, C. L. Hebert et al., *Experimental Limit on the Cosmic Diffuse Ultrahigh Energy Neutrino Flux*, *Physical Review Letters* **93** (2004) .

[74] N. G. Lehtinen, P. W. Gorham et al., *FORTE satellite constraints on ultrahigh energy cosmic particle fluxes*, *Physical Review D* **69** (2004) .

[75] P. Gorham, P. Allison et al., *Constraints on the ultrahigh-energy cosmic neutrino flux from the fourth flight of ANITA*, *Physical Review D* **99** (2019) .

[76] I. Kravchenko, G. Frichter et al., *Performance and simulation of the RICE detector*, *Astroparticle Physics* **19** (2003) 15–36.

[77] H. Landsman, L. Ruckman et al., *AURA—A radio frequency extension to IceCube*, *Nuclear Instruments and Methods in Physics Research Section A: Accelerators, Spectrometers, Detectors and Associated Equipment* **604** (2009) S70–S75.

[78] P. Allison, S. Archambault et al., *Design and performance of an interferometric trigger array for radio detection of high-energy neutrinos*, *Nuclear Instruments and Methods in Physics Research Section A: Accelerators, Spectrometers, Detectors and Associated Equipment* **930** (2019) 112–125.

[79] A. Anker, S. Barwick et al., *A search for cosmogenic neutrinos with the ARIANNA test bed using 4.5 years of data*, *Journal of Cosmology and Astroparticle Physics* **2020** (2020) 053.

[80] A. Vieregg, K. Bechtol et al., *A technique for detection of PeV neutrinos using a phased radio array*, *Journal of Cosmology and Astroparticle Physics* **2016** (2016) 005–005.

[81] P. Allison, S. Archambault et al., *Low-threshold ultrahigh-energy neutrino search with the askaryan radio array*, *Physical Review D* **105** (2022) .

[82] S. Barwick, D. Besson et al., *Radio detection of air showers with the ARIANNA experiment on the Ross Ice Shelf*, *Astroparticle Physics* **90** (2017) 50–68.

[83] T. A. collaboration, A. Anker et al., *Measuring the polarization reconstruction resolution of the arianna neutrino detector with cosmic rays*, *Journal of Cosmology and Astroparticle Physics* **2022** (2022) 022.

[84] A. Nelles, *A wind-turbine for autonomous stations for radio detection of neutrinos*, in *Proceedings of 36th International Cosmic Ray Conference — PoS(ICRC2019)*, vol. 358, p. 968, 2019, DOI.

[85] Q. Abarr, P. Allison et al., *The Payload for Ultrahigh Energy Observations (PUEO): A White Paper*, 2010.02892.

[86] J. Álvarez Muñiz, R. Alves Batista et al., *The Giant Radio Array for Neutrino Detection (GRAND): Science and design*, *Science China Physics, Mechanics Astronomy* **63** (2019) .

[87] S. Prohira, K. D. de Vries et al., *Observation of Radar Echoes from High-Energy Particle Cascades*, *Phys. Rev. Lett.* **124** (2020) 091101.

[88] R. Gandhi, C. Quigg et al., *Neutrino interactions at ultrahigh energies*, *Physical Review D* **58** (1998) .

[89] D. García-Fernández, A. Nelles et al., *Signatures of secondary leptons in radio-neutrino detectors in ice*, *Physical Review D* **102** (2020) .

[90] Y. S. Jeong, M. V. Luu et al., *Tau energy loss and ultrahigh energy skimming tau neutrinos*, *Physical Review D* **96** (2017) .

[91] L. D. Landau and I. I. Pomeranchuk, *The limits of applicability of the theory of Bremsstrahlung by electrons and of the creation of pairs at large energies*, *Dokl. Akad. Nauk SSSR* **92** (1953) 535.

[92] J. B. Johnson, *Thermal Agitation of Electricity in Conductors*, *Phys. Rev.* **32** (1928) 97.

[93] R. S. Roger, C. H. Costain et al., *The radio emission from the Galaxy at 22 MHz*, *Astronomy and Astrophysics Supplement Series* **137** (1999) 7–19.

[94] L. Pyras, *Optimizing the triggering strategy for the detection of cosmic rays with the Radio Neutrino Observatory Greenland (RNO-G)*, Ph.D. thesis, Humboldt University. 10.3204/PUBDB-2021-01462.

[95] ARIANNA collaboration, *Livetime and sensitivity of the ARIANNA Hexagonal Radio Array*, in *34th International Cosmic Ray Conference*, 8, 2015, 1509.00115.

[96] "International Spaceflight, Satellite Radio Frequencies." https://www.zarya.info/Frequencies/Frequencies136.php.

[97] P. Allison, R. Bard et al., *Performance of two Askaryan Radio Array stations and first results in the search for ultrahigh energy neutrinos*, *Physical Review D* **93** (2016) .

[98] P. Allison, J. Auffenberg et al., *First constraints on the ultra-high energy neutrino flux from a prototype station of the Askaryan Radio Array*, *Astroparticle Physics* **70** (2015) 62–80.

[99] J. A. Aguilar, A. Anker et al., *Triboelectric backgrounds to radio-based uhe neutrino exeperiments*, *Astroparticle Physics (accepted)* (2021) [2103.06079].

[100] A. Fedynitch, H. Dembinski et al., *A state-of-the-art calculation of atmospheric lepton fluxes*, *PoS* **ICRC2017** (2017) 1019.

[101] S. D. Kockere, K. de Vries et al., *Simulation of the propagation of CR air shower cores in ice*, in *Proceedings of 37th International Cosmic Ray Conference — PoS(ICRC2021)*, Sissa Medialab, jul, 2021, DOI.

[102] Welling, Christoph, *Ice Layers at Summit*, *presentation at RNO-G collaboration call* .

[103] A. Kovacs, A. J. Gow et al., *The in-situ dielectric constant of polar firn revisited*, *Cold Regions Science and Technology* **23** (1995) 245.

[104] R. L. Hawley, E. M. Morris et al., *Rapid techniques for determining annual accumulation applied at Summit, Greenland*, *Journal of Glaciology* **54** (2008) 839–845.

[105] R. Alley and B. Koci, *Ice-Core Analysis at Site A, Greenland: Preliminary Results*, *Annals of Glaciology* **10** (1988) 1–4.

[106] J. Avva, J. M. Kovac et al., *An in situ measurement of the radio-frequency attenuation in ice at Summit Station, Greenland*, *Journal of Glaciology* **61** (2015) 1005–1011.

[107] J. A. Aguilar, P. Allison et al., *In situ, broadband measurement of the radio frequency attenuation length at Summit Station, Greenland*, 2201.07846.

[108] S. Barwick, D. Besson et al., *South Polar in situ radio-frequency ice attenuation*, *Journal of Glaciology* **51** (2005) 231–238.

[109] "Near Surface Ice Temperatures." https://user-web.icecube.wisc.edu/~araproject/radio/#surfacetemps.

[110] S. Barwick, E. Berg et al., *Observation of classically 'forbidden' electromagnetic wave propagation and implications for neutrino detection.*, *Journal of Cosmology and Astroparticle Physics* **2018** (2018) 055–055.

[111] C. Deaconu, A. G. Vieregg et al., *Measurements and modeling of near-surface radio propagation in glacial ice and implications for neutrino experiments*, *Phys. Rev. D* **98** (2018) 043010.

[112] A. Anker, S. Barwick et al., *Probing the angular and polarization reconstruction of the ARIANNA detector at the South Pole*, *Journal of Instrumentation* **15** (2020) P09039–P09039.

[113] T. M. Jordan, D. M. Schroeder et al., *A Polarimetric Coherence Method to Determine Ice Crystal Orientation Fabric From Radar Sounding: Application to the NEEM Ice Core Region*, *IEEE Transactions on Geoscience and Remote Sensing* **57** (2019) 8641.

[114] "Create Design Corp." `http://www.cd-corp.com/english/`.

[115] I. Kravchenko, S. Hussain et al., *Updated results from the RICE experiment and future prospects for ultra-high energy neutrino detection at the south pole*, *Phys. Rev. D* **85** (2012) 062004.

[116] J. A. Aguilar Sánchez, P. Allison et al., *Hardware Development for the Radio Neutrino Observatory in Greenland (RNO-G)*, p. 1058, 07, 2021, DOI.

[117] "Summit Station." `https://geo-summit.org`.

[118] A. Shturmakov and P. Sendelbach, *A new 122 mm electromechanical drill for deep ice-sheet coring (DISC): 4. Drill cable*, *Annals of Glaciology* **47** (2007) 51.

[119] C. Glaser, D. García-Fernández et al., *NuRadioMC: simulating the radio emission of neutrinos from interaction to detector*, *The European Physical Journal C* **80** (2020) .

[120] C. Glaser, A. Nelles et al., *NuRadioReco: a reconstruction framework for radio neutrino detectors*, *The European Physical Journal C* **79** (2019) .

[121] J.-H. Koehne, K. Frantzen et al., *PROPOSAL: A tool for propagation of charged leptons*, *Computer Physics Communications* **184** (2013) 2070.

[122] A. M. Dziewonski and D. L. Anderson, *Preliminary reference Earth model*, *Physics of the Earth and Planetary Interiors* **25** (1981) 297.

[123] J. Alvarez-Muñiz, R. A. Vázquez et al., *Calculation methods for radio pulses from high energy showers*, *Physical Review D* **62** (2000) .

[124] J. Alvarez-Muñiz, C. James et al., *Thinned simulations of extremely energetic showers in dense media for radio applications*, *Astroparticle Physics* **32** (2009) 100.

[125] J. Bellm et al., *Herwig 7.1 Release Note*, `1705.06919`.

[126] J. Alvarez-Muñiz, C. James et al., *Thinned simulations of extremely energetic showers in dense media for radio applications*, *Astroparticle Physics* **32** (2009) 100.

[127] T. Winchen, *RadioPropa — A Modular Raytracer for In-Matter Radio Propagation*, *EPJ Web of Conferences* **216** (2019) 03002.

[128] J. Avva, J. M. Kovac et al., *An in situ measurement of the radio-frequency attenuation in ice at Summit Station, Greenland*, *Journal of Glaciology* **61** (2015) 1005–1011.

[129] S. Buitink, *Using FDTD simulations to study radio propagation effects*, in *Proceedings of the ARENA 2018*, 2018, http://dx.doi.org/10.22323/1.395.1027.

[130] S. Prohira, C. Sbrocco et al., *Modeling in-ice radio propagation with parabolic equation methods*, *Physical Review D* **103** (2021) .

[131] R. A. Batista, A. Dundovic et al., *CRPropa 3—a public astrophysical simulation framework for propagating extraterrestrial ultra-high energy particles*, *Journal of Cosmology and Astroparticle Physics* **2016** (2016) 038–038.

[132] J. R. Cash and A. H. Karp, *A variable order runge-kutta method for initial value problems with rapidly varying right-hand sides*, *ACM Trans. Math. Softw.* **16** (1990) 201–222.

[133] B. Oeyen, I. Plaisier et al., *Effects of firn ice models on radio neutrino simulations using a RadioPropa ray tracer*, in *Proceedings of 37th International Cosmic Ray Conference (ICRC2021)*, vol. 395, 2021, http://dx.doi.org/10.22323/1.395.1027.

[134] J. Souney, J. M., M. Aydin et al., *The South Pole ice core (SPICEcore) project*, in *AGU Fall Meeting Abstracts*, vol. 2018, pp. C41C–1771, Dec., 2018, https://ui.adsabs.harvard.edu/abs/2018AGUFM.C41C1771S.

[135] P. Allison, J. Auffenberg et al., *First constraints on the ultra-high energy neutrino flux from a prototype station of the Askaryan Radio Array*, *Astroparticle Physics* **70** (2015) 62.

[136] ARA collaboration, *Arrival direction reconstruction of ultra-high-energy neutrinos with ARA*, *PoS* **ICRC2019** (2020) 933.

[137] J. A. Torres Espinosa, *Neutrino Astrophysics With The Askaryan Radio Array*, Ph.D. thesis, The Ohio State University, 2021.

[138] C. Welling, C. Glaser et al., *Reconstructing the cosmic-ray energy from the radio signal measured in one single station*, *Journal of Cosmology and Astroparticle Physics* **2019** (2019) 075–075.

[139] G. G. Gaswint, *Quantifying the Neutrino Energy and Pointing Resolution of the ARIANNA Detector*, Ph.D. thesis, UC, Irvine, 2021.

[140] C. Welling, P. Frank et al., *Reconstructing non-repeating radio pulses with Information Field Theory*, *Journal of Cosmology and Astroparticle Physics* **2021** (2021) 071.

[141] C. Glaser, S. McAleer et al., *Deep-learning-based reconstruction of the neutrino direction and energy for in-ice radio detectors*, *Astroparticle Physics* **145** (2023) 102781.

[142] ARA collaboration, *A neural network based UHE neutrino reconstruction method for the Askaryan Radio Array (ARA)*, *PoS* **ICRC2021** (2021) 1157.

[143] A. Anker, S. Barwick et al., *Neutrino vertex reconstruction with in-ice radio detectors using surface reflections and implications for the neutrino energy resolution*, *Journal of Cosmology and Astroparticle Physics* **2019** (2019) 030–030.

[144] J. Alvarez-Muñiz, A. Romero-Wolf et al., *Čerenkov radio pulses from electromagnetic showers in the time domain*, *Phys. Rev. D* **81** (2010) 123009.

[145] T. M. Jordan, D. Z. Besson et al., *Modeling ice birefringence and oblique radio wave propagation for neutrino detection at the South Pole*, *Annals of Glaciology* **61** (2020) 84–91.

[146] D. Z. Besson, I. Kravchenko et al., *Polarization angle dependence of vertically propagating radio-frequency signals in South Polar ice*, *Astropart. Phys.* **144** (2021) 102766 [2110.13353].

[147] A. Connolly, *Impact of biaxial birefringence in polar ice at radio frequencies on signal polarizations in ultrahigh energy neutrino detection*, *Physical Review D* **105** (2022) .

[148] D. Dahl-Jensen, N. Gundestrup et al., *Basal melt at NorthGRIP modeled from borehole, ice-core and radio-echo sounder observations*, *Annals of Glaciology* **37** (2003) 207–212.

[149] IceCube collaboration, *A measurement of the diffuse astrophysical muon neutrino flux using eight years of IceCube data.*, *PoS* **ICRC2017** (2018) 1005.

[150] A. van Vliet, R. A. Batista et al., *Determining the fraction of cosmic-ray protons at ultrahigh energies with cosmogenic neutrinos*, *Physical Review D* **100** (2019) .

[151] S. S. Wilks, *The Large-Sample Distribution of the Likelihood Ratio for Testing Composite Hypotheses*, *Annals Math. Statist.* **9** (1938) 60.

[152] B. Wang, W. Shi et al., *Confidence Analysis of Standard Deviational Ellipse and Its Extension into Higher Dimensional Euclidean Space*, *PloS one* **10** (2015) e0118537.

[153] R. Dekany et al., *The Zwicky Transient Facility: Observing System*, *Publ. Astron. Soc. Pac.* **132** (2020) 038001 [2008.04923].

[154] J. van Santen, B. Clark et al., *toise: a framework to describe the performance of high-energy neutrino detectors*, *Journal of Instrumentation* **17** (2022) T08009.

[155] G. Cowan, K. Cranmer et al., *Asymptotic formulae for likelihood-based tests of new physics*, *The European Physical Journal C* **71** (2011) .

[156] C. G. pin, K. Kotera et al., *Ultra-high-energy cosmic rays and neutrinos from tidal disruptions by massive black holes*, *Astronomy and Astrophysics* **616** (2018) A179.

[157] K. Murase, *High energy neutrino early afterglows from gamma-ray bursts revisited*, *Physical Review D* **76** (2007) .

[158] B.-B. Zhang, B. Zhang et al., *A peculiar low-luminosity short gamma-ray burst from a double neutron star merger progenitor*, *Nature Communications* **9** (2018) .

[159] K. Murase, Y. Inoue et al., *Diffuse neutrino intensity from the inner jets of active galactic nuclei: Impacts of external photon fields and the blazar sequence*, *Physical Review D* **90** (2014) .

Appendix

A RFI events

Figure 8.1 and 8.2 show spectrograms for RNO-G RFI events for the first data taking season. The events are identified to stem from the hardware of an RNO-G station, as explained in section 3.5. As can be seen from the figures, the RFI pulses caused by the LoRaWAN (figure 8.1) are more narrow band and for lower frequencies than the backgrounds caused by the charging of the batteries (figure 8.2).

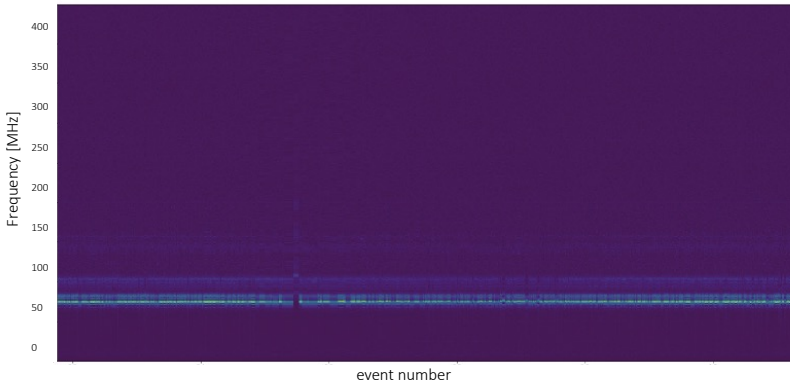

Figure 8.1: Spectrogram for RFI events observed in RNO-G data caused by the LoRaWAN communication antenna.

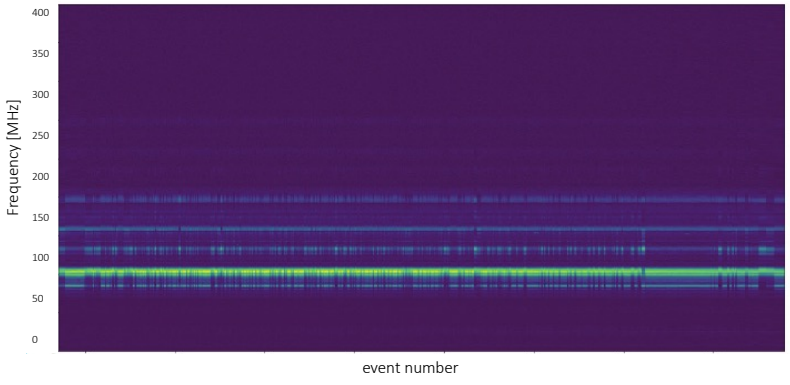

Figure 8.2: Spectrogram for RFI events observed in RNO-G data caused by the batteries.

B Viewing Angle Resolutions

The resolution of the viewing angle improves for event with a large SNR for reconstruction as shown in figure 8.3.

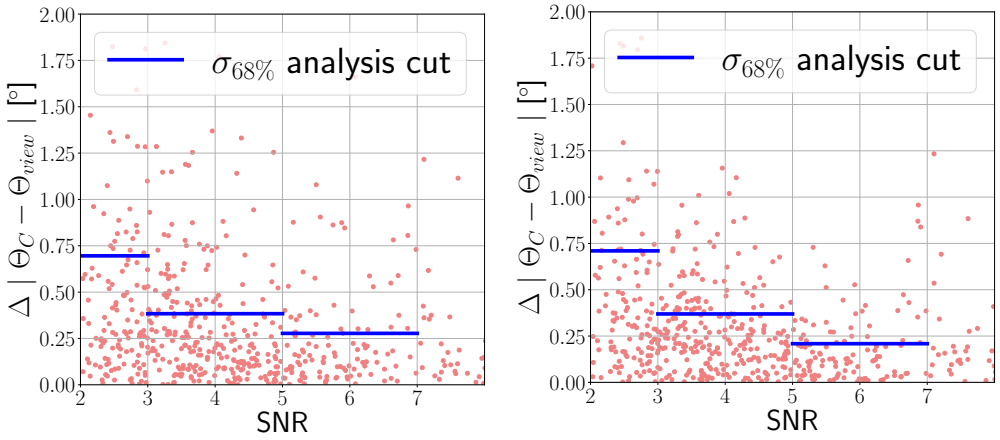

Figure 8.3: Viewing angle resolutions for reconstructing with the *Alvarez2009* parametrization (left) and with the *ARZ*-templates for the full hadronic eventset described in section 7.1.1 for the default analysis.

C Firn Model

As discussed in section 6.6, the impact of the ice model is important for the reconstructions, since it influences the expected time differences of the waveforms. Simulating the ice with a single exponential function and reconstructing with a double exponential function, as suggested by [111], results in an offset for the neutrino arrival direction as shown in figure 8.4.

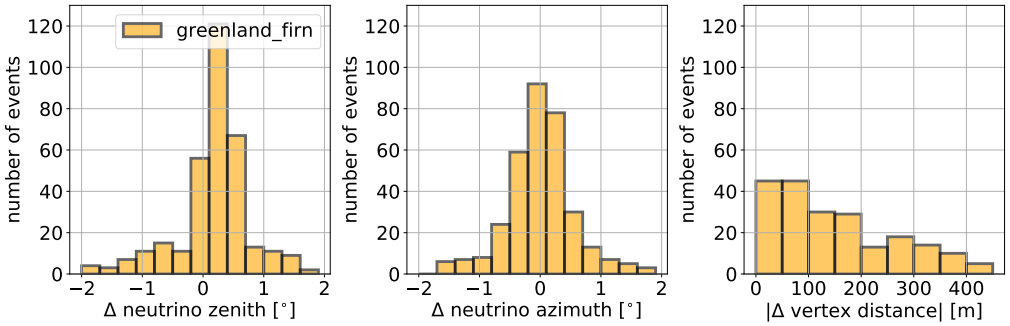

Figure 8.4: Impact of the firn model on the direction reconstruction. For this comparison noiseless simulations are used and for the forward-folding approach a single Vpol-Hpol pair is used in the reconstruction.

D *ARZ* Shower Profiles

As discussed in section 6.3.7, templates for the *ARZ2020* model are created and used as an electric-field model for the reconstructions. Figure 8.5 left shows an example shower library including all shower profiles for this shower energy available in NuRadioMC, together with the average shower profile indicated in orange which is used for the templates. Resulting waveforms are shown right. Figure 8.6 shows for an example library three shower profiles relative to the *ARZ*-templates. The deviations observed lead to an inperfect reconstruction which mainly influence the resolution of the polarization, as discussed in section 6.4.4.

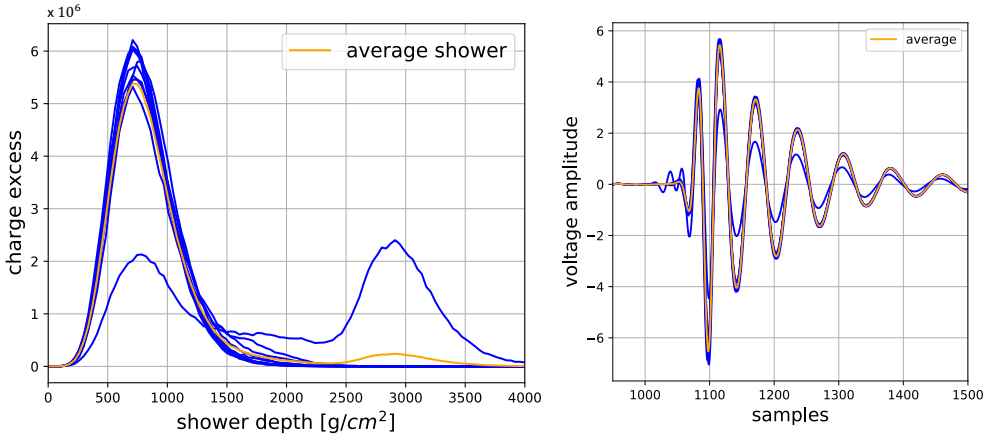

Figure 8.5: Left: Shower profiles for the full *ARZ2020* shower library available in NuRadioMC for an example energy. In orange, the average profile is shown. This profile is used for the *ARZ*-templates. Right: Example waveforms corresponding to the shower profiles and the left. In orange the waveform from the *ARZ*-templates is shown.

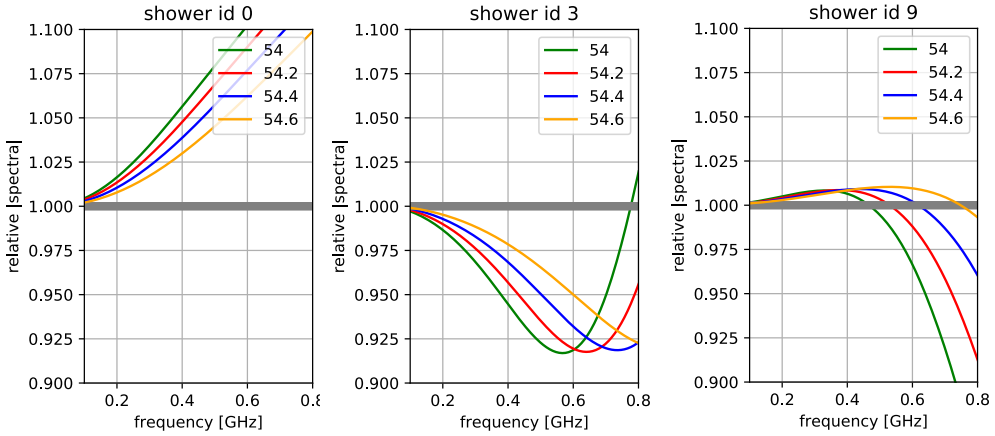

Figure 8.6: Example electric-field spectra (R = 2 km, E_{sh} = 10^{18} eV) that shows the deviations between individual shower profiles, as part of the *ARZ* shower library in the radio neutrino software NuRadioMC [119]. For three shower profiles (out of the 10 available per shower energy), the spectra relative to the sectra due to the average shower profile (grey) is shown. This average shower profile is used for the reconstructions with the *ARZ*-template. Spectra for four viewing angles are given (colored lines). Per shower profile, variations till 10% are observed compared to the average spectrum. Further more, variations till 3% for the same shower profile is observed for varying viewing angles.

E Energy Resolutions

Section 7.2.2 discusses the energy resolution for RNO-G. Figure 8.7 and 8.8 show the corresponding distributions.

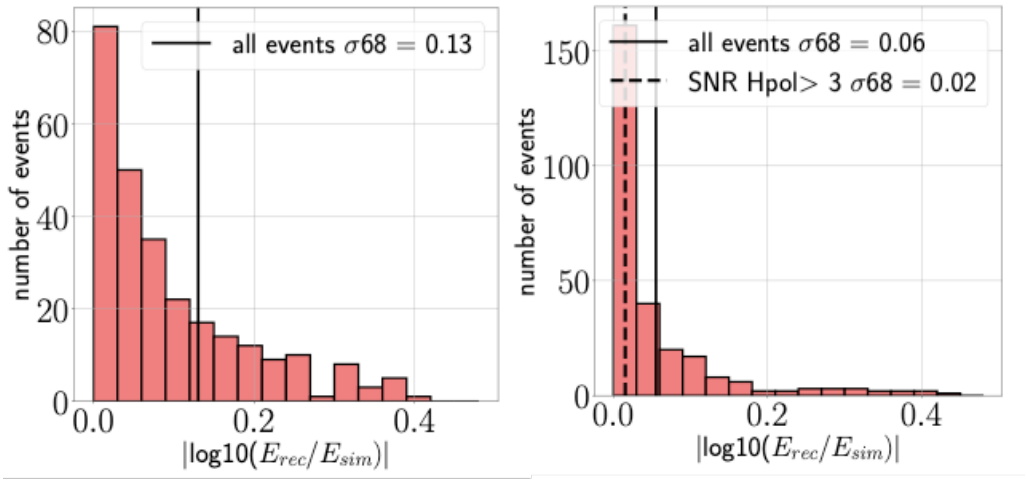

Figure 8.7: Shower energy resolution using the phased array (left) and the full station (right) making use of the true vertex position.

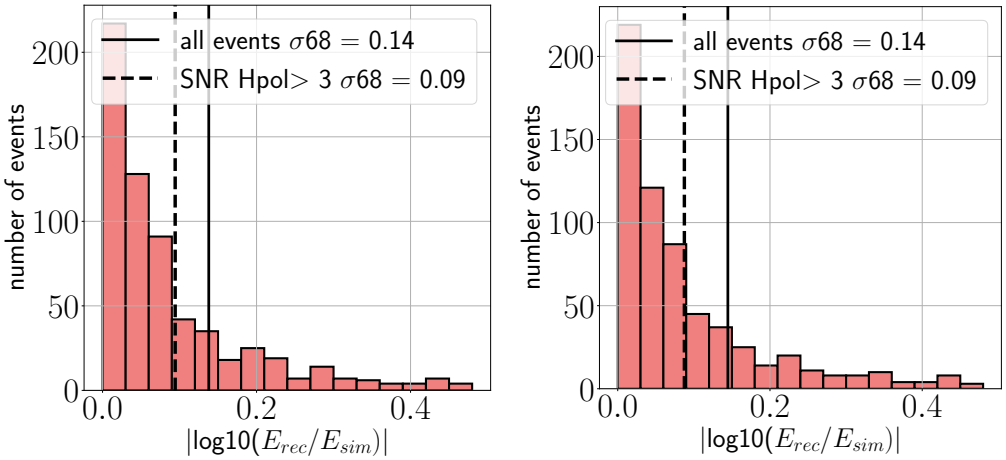

Figure 8.8: Shower energy resoltuion for reconstructing with *ARZ*-templates (left) and *Alvarez2009* (right) for the default analysis, i.e. the hadronic contribution of the flux discussed in 7.1.1 with an applied event selection discussed in 7.1.2.

F Results for Reconstructing with *ARZ*-templates

Section 7.2 shows the results for the angular resolution for RNO-G using the *Alvarez2009*-model. Results for the reconstruction obtained with the *ARZ*-templates are shown in 8.9, 8.10 and 8.11.

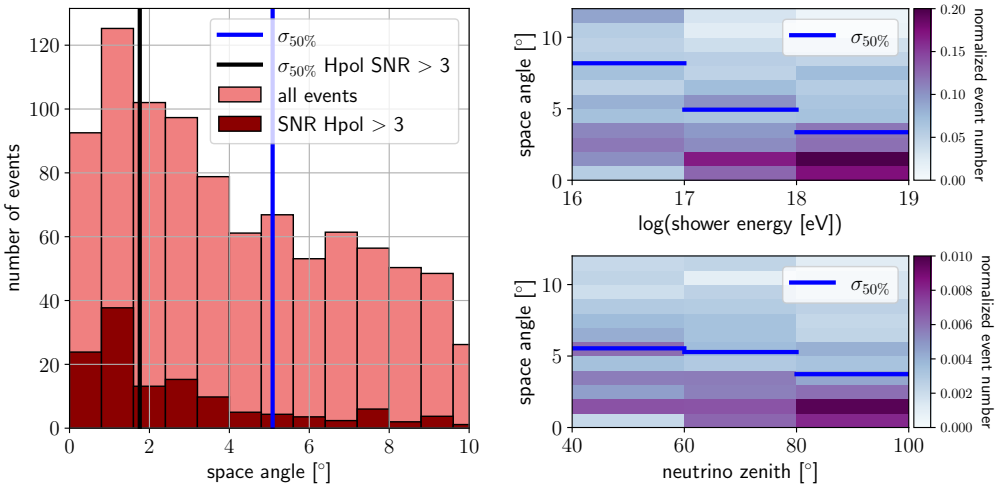

Figure 8.9: Space angle results for the full hadronic event set for an IceCube and GZK flux model described in 7.1.1 for reconstructing with *ARZ*-templates.

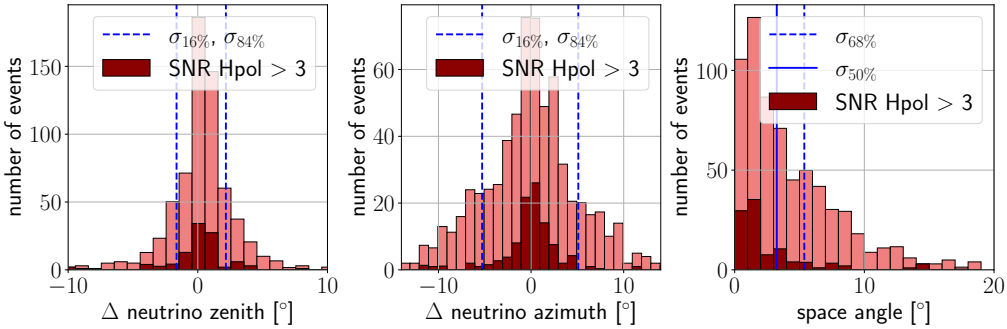

Figure 8.10: Space angle results and resolutions for neutrino zenith and azimuth for reconstructing with *ARZ*-templates for the default analysis, i.e. the hadronic contribution of the flux discussed in 7.1.1 with an applied event selection discussed in 7.1.2.

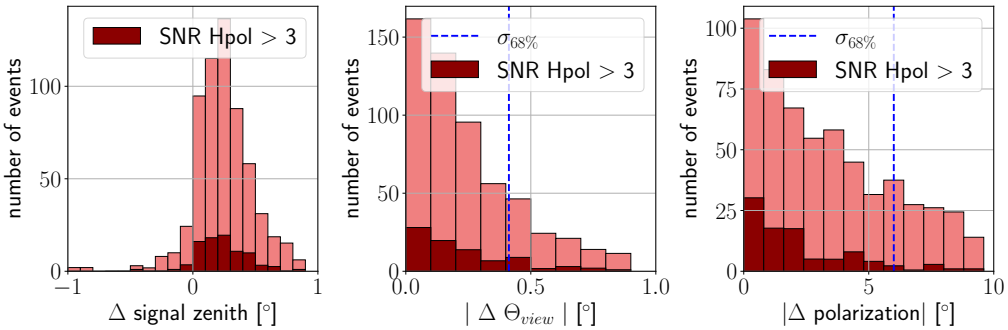

Figure 8.11: Resolutions for the signal arrival direction (left), the viewing angle (middle) and the polarization (right) for the default analysis, i.e. the hadronic contribution of the flux discussed in 7.1.1 with an applied event selection discussed in 7.1.2.

G Uncertainty Estimation

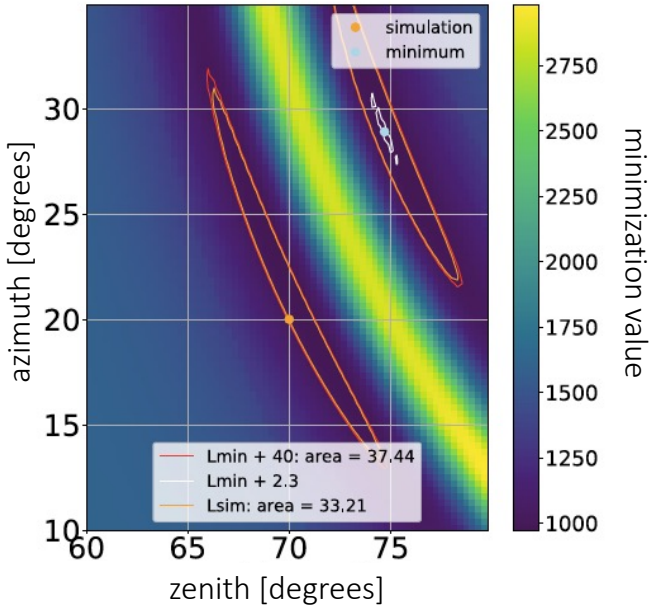

Figure 8.12: Minimization landscape for an example event. Seen are the minimum regions on each side of the Cherenkov angle with similar | Δ Θ_{view} - Θ_C |. Uncertainty contours are given for different error estimations. Note that the orange contour is given by $L = L_{\text{sim}}$ and therefore the simulated value (orange dot) is on the edge of this contour.

Section 7.3 describes the methods used to obtain uncertainty estimates for single even reconstructions. This appendix outlines in more detail the method of *recalibrating the minimization landscape* using an example event simulated and reconstructed with the *Alvarez2009* model.

The minimization landscape for an example event is shown in figure 8.12. For each direction the probability of the event coming from that direction is determined by finding the energy which minimizes the test statistic. The landscape shows a clear double banana-shape structure which corresponds to the two sides of the Cherenkov angle. As can be seen in the figure, the reconstructed value (blue) is reconstructed on the other side of the Cherenkov cone. The contour in orange indicates the area where the direction of the neutrino is more likely than the simulated value, i.e. $L = L_{\text{sim}}$.

When the minimization landscape is purely determined by statistical fluctuations, the contours can be determined by using Wilk's theorem [151]. Since the global best fitted value has 3 degrees of freedom and every other point on the grid has only 1, the subtraction of $\chi^2(3)_{\text{min}}$ -

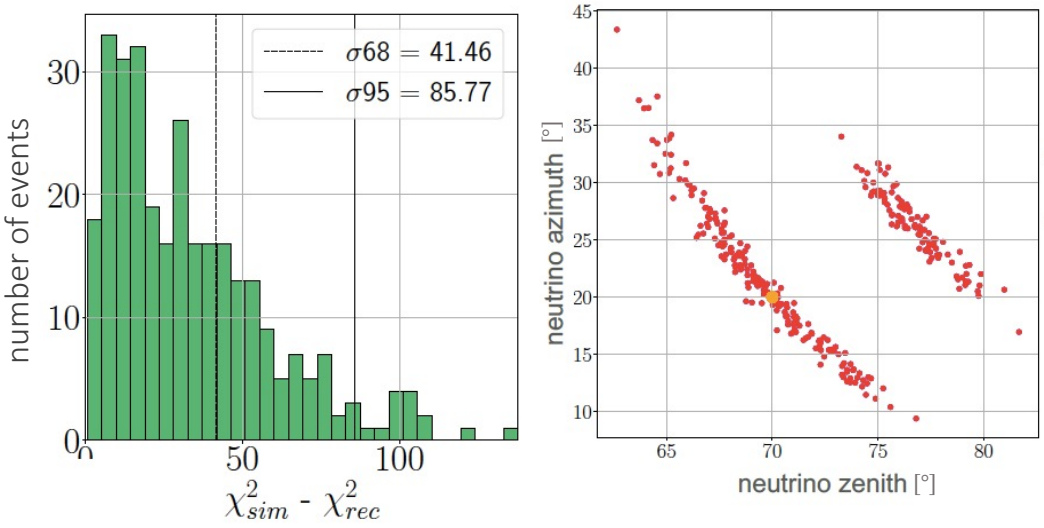

Figure 8.13: Left: Distribution of the difference between the minimization value of the simulation and the reconstruction. Right: Spread in the reconstruction of the neutrino direction corresponding to the distribution shown in the left, as well as the minimization landscape of figure 8.12.

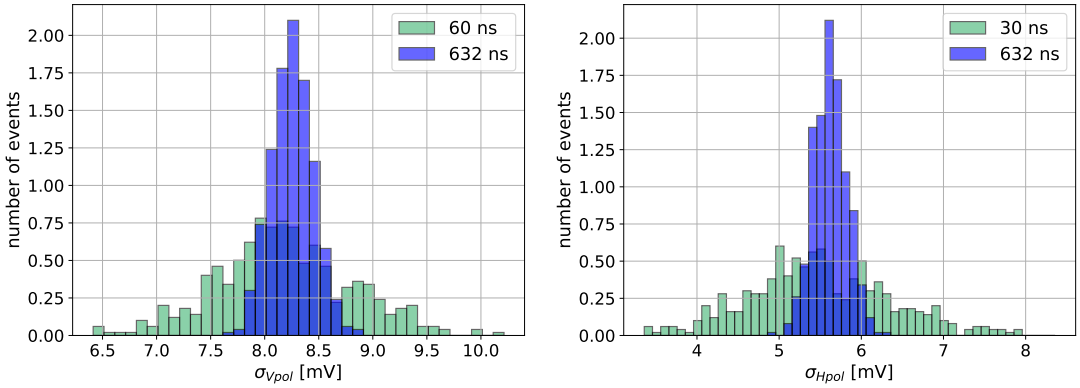

Figure 8.14: Distribution of root-mean-squared σ of the noise for the time windows and filters of the Vpol (left) and Hpol (right). For the Vpol, a σ_{Vpol} of 8.2 mV is used, and for σ_{Hpol} a value of 5.6 mV for the standard deviation in the test statistic as described in section 6.3.1

$\chi^2(1)$ will be $\chi^2(2)$ distributed. Therefore, the 1-σ contour can be determined by:

$$L_{\text{min}} - L = 2.3 \tag{8.1}$$

The χ^2-landscape and the corresponding 1-σ contour is shown in figure 8.12 in white. Wilk's theorem results in a small 1-σ contour which does not include the true direction.

The test statistic used, asummes a Gaussian distribution of the noise. However, this is not necessary valid in the small time-windows used for the reconstruction. Due to the incomplete noise-model and the large number of samples, ΔL takes values way larger than expected for purely statistical fluctuations. The variation in σ_{i} for the time-windows used is shown in figure 8.14 . Furthermore, the noise in the time-domain is autocorrelated, and in the χ^2 minimization is the dependence of neighbouring samples not taken into account. Therefore, Wilk's theorem cannot be used to extract event dependent uncertainties.

To understand the impact of the noise on the reconstruction the event from 8.12 with the same (x, y, z, θ, ϕ and E) is simulated. Each event with its own set of Rayleigh disributed random thermal noise. The spread in the reconstructed azimuth and zenith are shown in figure 8.13 right. As can be noticed by comparing this figure to 8.12, is that the spread due to the noise is way larger than purely statistical. Also, the reconstructions result in two neutrino direction clusters.

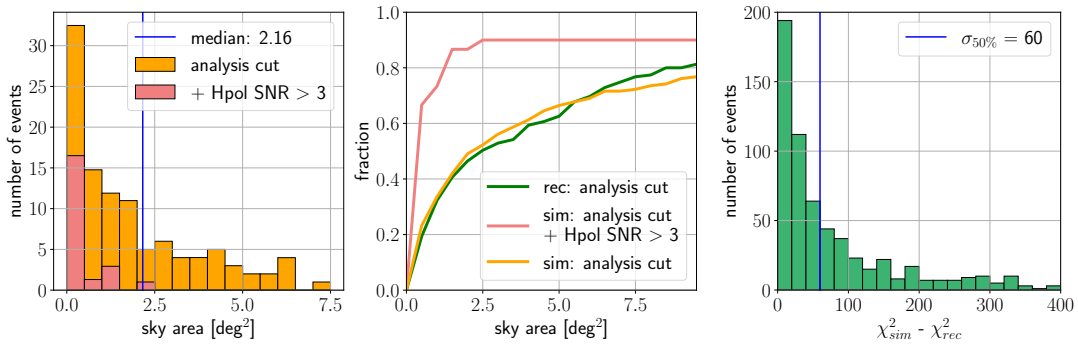

Figure 8.15: Left: Distribution of the region with a smaller calculated χ^2 than the true direction, i.e. the area that is more likely to be reconstructed than the true value (sky area). A clear improvement for event with a large Hpol contribution is observed. Middle: CDF of the sky area. In green the sky area is determined with $L < \Delta L$ with ΔL the 68% values from the L_{sim} -L_{min} distribution, such that the covered area corresponds to the region such that for 68% of the events the true value lies within this region. Right: Distribution for L_{sim} - L_{rec} for the default analysis.

This corresponds to the same $|\Theta_C - \Theta_{\text{view}}|$, but at the different sides of the Cherenkov angle. Figure 8.13 left shows the distribution of

$$\Delta L = L_{\text{sim}} - L_{\text{rec}} \tag{8.2}$$

values for each of these simulated events. The angular uncertainty due to the noise is estimated by mapping the $\Delta\chi^2$ distribution to p-value. The confidence region is determined by calculating the lower quantile from the distribution. The 68% coverage is determined and the contours are shown in figure 8.12. The contour can be interpreted as 68% time of a similar event reaching the detector, the true direction would be within the given contour. Furthermore, as can be seen in the same figure, is that the method includes the two minima corresponding to the two sides of the Cherenkov cone.

The distribution for the true sky area for the *Alvarez2009* event set is shown in figure 8.15 left. Especially for events with Hpol contribution the sky area results in a very good resolution. The cumulative distribution on the right also indicates the results obtained with above outlined method, using a containment of 68%.

For the estimation of the sky area (discussed in 7.3), the above described method can be used. A contour using the approach is given in figure 7.10. The distribution to obtain the contours for the default analysis is shown in figure 8.15 right.

Acknowledgements

Dankjewel.
— *Dutch for* Thank you

During the scope of this thesis, RNO-G developed from an un-funded project to its first data taking year. All big things start small, and it has been fascinating to experience the first years of this very ambitious project, and learn from the experience and expertise from all the contributing people involved.
First of all, *dankjewel* Anna. For this great oppurtinity, for being one of the motivators of this project, and also for showing your vision of "*Chose what is important for you, and just go for it*".
Dankjewel RNO-G collaboration. For the pleasant cooperation. Due to the pandemic I unfortunately never had the pleasure to meet most of you in person, but it still feels like we're all part of the same team. I'm very greatfull for the opportunity to deploy the first RNO-G stations in Greenland, which was an unforgettable experience, and had an amazing time with some of you here.
Then, the DESY and FAU radio neutrino group, *dankjewel* for endless hours of discussing, coding, questioning, complaining and drinking. This was great fun. You all made my PhD experience more than amazing.
A big *dankjewel* to a large fraction of the DESY PhD students. For becoming great friends and keep reminding me that science (as well as life) is more than radio neutrino detection. Especially to Lilly, Zack, Steffen, Jakob, Christoph, Marc, Leander and Richard for reading parts of the thesis for feedback.
My parents and siblings, *dankjewel* for all those hours spend in the car and train, moving me around Berlin, and for the plenty of visits. You made me feel like I was not so far away after all.
Lastly, Marc, *dankjewel* for showing me how easy and fun life can be.

'We hebben nog zo ver te gaan,' zuchtte de jongen
'Ja. Maar kijk eens hoe ver we zijn gekomen,' zei het paard.
- Charlie Mackesy